Modeling and control of NPC based converter interface for hybrid storage system dedicated to microgrid purposes

Quentin Tabart

Communauté
UNIVERSITÉ Grenoble Alpes

THÈSE

Pour obtenir le grade de

DOCTEUR DE LA COMMUNAUTE UNIVERSITE GRENOBLE ALPES

Spécialité : **Génie électrique**

Arrêté ministériel : 25 mai 2016

Présentée par

Quentin TABART

Thèse dirigée par **Ionel Vechiu, Professeur, ESTIA Recherche**, et codirigée par **Seddik BACHA, Professeur, Université Grenoble Alpes**

préparée au sein du **Laboratoire ESTIA Recherche / G2ELAB** dans **l'École Doctorale EEATS**

Modélisation et commande d'une interface à base d'un convertisseur NPC pour système de stockage hybride dédié micro-réseau

Thèse soutenue publiquement le **« 10/12/2019 »**, devant le jury composé de :

M, Abdelkrim BENCHAIB
Dr. HDR, R&D Manager Supergrid Institue, Rapporteur
M, Jean Paul GAUBERT
Professeur, Université de Poitiers, Rapporteur
Mme, Xuefang LIN-SHI
Professeur, INSA Lyon, Examinatrice, Présidente du jury

I'd put my money on the sun and solar energy.
What a source of power. I hope we don't have to
wait until oil and coal run out before we tackle that.

Thomas Edison

Acknowledgements

First of all I would like to show my deep gratitude to the director and co-director of my thesis, Ionel Vechiu and Seddik Bacha for their guidance, patience and perseverance.

I show my gratitude to Xuefang Lin-Shi, professor at *INSA Lyon*, for presiding the jury and Jean Paul Gaubert, professor at *Université de Poitié*, and Abdelkrim Benchaib, *R&D manager at Supergrid Institute*, for having reviewed this dissertation.

I gratefully acknowledge the director of ESTIA Jean-Roch Guiresse and his successor Patxi Elissalde for giving me the opportunity to be part of ESTIA's adventures, as well as Nadine Couture for her emotional support and for being a breath of fresh air.

Je voudrais aussi remercier chaleureusement le bureau des doctorants et en particulier Aitor, Sylvain, Ruben, Ahmed, Barbie, Samuel, Audrey, Max, Dim et tous les autres, mais aussi tous mes stagiaires et les étudiants, doctorants ainsi que le personnel de l'ESTIA pour leur amour fougueux du Pays Basque.

Finalement, last but not least, un grand merci à Sarah pour son amour à toute épreuve et à Léa pour sa coquinerie, et aussi à mes parents et ma sœur pour leur soutiens tout au long de cette thèse. Merci du fond du cœur.

Abstract

The increasing rise of distributed generation integration in the energy mix is a challenging issue. Indeed distributed generation based on renewable energy sources like solar and wind creates fluctuation of the grid's parameter and can lead to minor issues like harmonics, over or under voltages, flicker and so on, or to major failure like blackouts. The concept of microgrid associated with energy storage systems is seen as a potential solution to increase renewable energy integration to the grid, while increasing efficiency and reliability at the same time.

A review of energy Storage technologies is carried out and it results that currently none of these technologies can offer energy and power capabilities while fast response and efficiency at the same time. The use of Hybrid Energy Storage System allows to reach such performance. For this thesis, a Li-Ion and a Vanadium Redox Flow Battery have been selected for their good power and energy abilities respectively, and their high round trip efficiency.

The main contribution of this work lies in the structural limits analysis of the topology and the control algorithm for the four leg three level NPC used as a multipurpose interface between a Renewable Energy Source, a Hybrid Energy Storage System and a Microgrid. The effectiveness of the proposed algorithms and limits model are tested both in simulation and experiments. Ancillary services like frequency and voltage support are then developed and tested in simulation under various conditions.

Table of Contents

List of Figures

List of Tables

Chapter 1

Introduction

Contents

1.1 Distributed Generation

1.1.1 Introduction

The 20th century saw the emergence of electrical energy as the main vector of development. Power systems were designed in a centralized fashion, with large production plants (coal, gas, nuclear, dams) supplying consumers and industries through transmission and distribution networks. This model has proven its high availability and reliability in a dense power system thanks to redundancy, but shown high losses and expansion costs, especially for rural areas [1].

Entering the 21st century, the breakthrough of renewable based production technologies in solar, wind, hydro and biomass, along with energy market liberalization and financial incentive, allowed medium to small producers to connect to the low voltage distribution network to diversify the energy mix. The centralized scheme which has been used to design the national scale power systems has quickly been pressured by these distributed energy producers, causing issues to the grid but also pushing forward new concepts to make large integration of renewable energy possible.

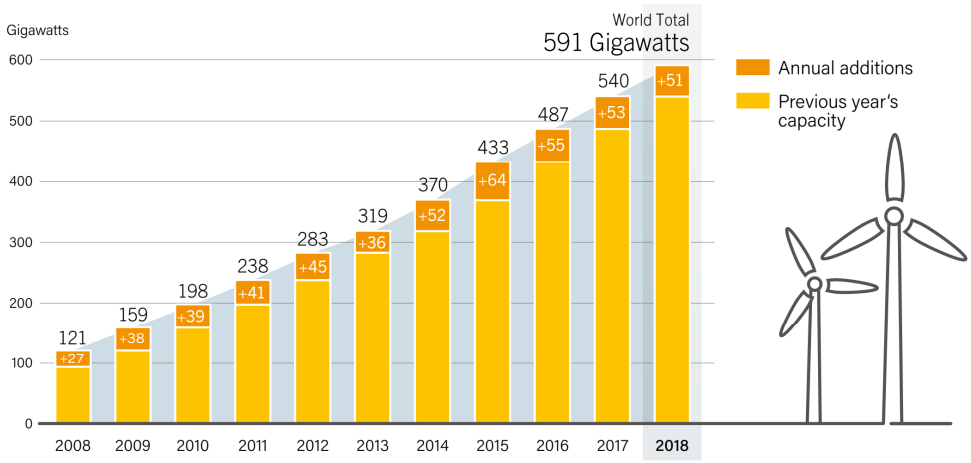

Figure 1.1 Wind power global capacity [2]

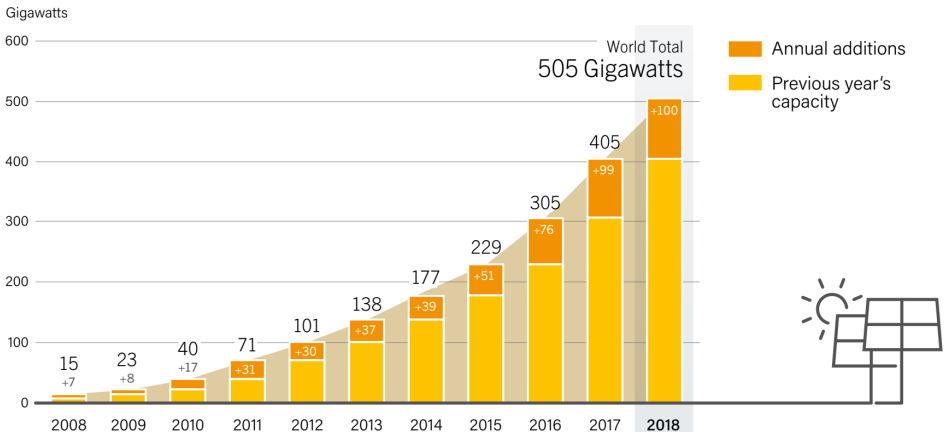

Figure 1.2 Solar PV power global capacity [2]

1.1.2 Definition of DG

Distributed generation research emerged from the need to address issues caused by the fast growth of RES based small power plants' integration to distribution networks. DG mainly stands in opposition to centralized generation with large power plants. But there is not yet consensus on a precise definition of DG as it encompasses several concepts or practices named as on-site generation, dispersed generation, embedded generation, decentralized generation, decentralized energy, situ generation or distributed energy.

Still, the main characteristics behind the DG concept are the geographical closeness of the source to the consumers as well as the dispersion and limited power of the generators [3]. As a consequence, many grid codes would state that such sources should be connected to the distribution network, which can be considered as the main definition of DG in an interconnected power system. The case of islanded grids such as island grids can be considered as an implementation of DG concept because of the closeness of the production to the consumption area despite the particularities involved by such weak power systems.

DG technologies typically use renewable energy sources like solar, wind, small hydro and biomass. It includes also small combustion engine generators and Distributed Energy Storage Systems (DESS). The drawbacks associated with the

variable nature of some RES based DG like solar and wind focuses most of the research in this field as large DG integration to the grid can cause major issues.

1.1.3 Issues caused by DGs

The old unidirectional distribution system became quickly pressured by the massive growth of DG systems, particularly by some RES based like wind and solar due to their stochastic nature causing near unpredictable production variations. Distribution System Operators (DSO) had to take into account the DG factor in the planning of distribution network expansion to counterbalance the increased number of failure and incidents observed in the field [4]–[7].

Issues observed at the different levels of the distribution network are mostly passive components lifetime reduction (transformers, feeders, protections) and distribution network increased losses. The main causes of these drawbacks are related to the following power quality issues and are actively studied in the literature:

- Voltage rise in the DG's neighborhood and feeder overvoltage [8]
- Voltage/current unbalances due to monophasic DGs/loads [8], [9]
- Frequency oscillation [10]–[12]
- Zero sequence current [8]
- Harmonic amplification [13]

These issues are exacerbated by the penetration of variable RES based DG because of the lack of control of such generators and could cause major drawbacks in the case of a large DG integration in the current distribution networks. Although, it has also been shown that using DG has the ability to improve power quality in rural areas using adapted control methods.

1.1.4 Evolution of grid codes and standards

The aforementioned issues are addressed in a different way in the literature. Standardization process, as well as grid codes, have implemented some of the proposed solutions. In recent years, committees such as IEEE Standard Association (SA) or the European Renewable Energy Council (EREC) have

released new standards or guides to overcome lacks of previous releases. Noticeable improvements to facilitate DG unit penetration to distribution networks can be found in the EREC G83 (2016) Distributed Generation Connection Guide, the IEEE 1547.6-2011 Recommended Practice for Interconnecting Distributed Resources with Electric Power Systems Distribution Secondary Networks. These standards are widely used and discussed within the scientific community [9], [14]–[29].

From technical point of view, one of the most important standards adopted and implemented in most grid codes in recent years is the voltage regulation through reactive power for DGs such as wind farms and solar plants [9]. This standard is widely accepted but still, its systematic implementation is subject to impact studies, mainly because of the wide range of techniques and devices used for such functionality and its dependence on voltage conditions. The lack of harmonization of grid codes makes it even harder to generalize these standards, even though European countries put effort in that way [17].

Particular effort has been put into Island grids standardization tanks to the competitiveness of RES compared to conventional generation as the latter often depends on costly importation of fuel or gas, and does not benefit of economies of scale [5], [30]–[33]. But variable RES are considered fatal to a weak network due to stability issues, and for example, solar plant and wind farms are subject to a 30% penetration limit in French islands [5], [33]–[35]. Even though important improvements have been implemented in forecasting tools, there is a consensus on RES based DG unit installation in island grids for the addition of Energy Storage System (ESS) to smooth the power variation and enable ancillary services which are necessary for weak grid context [31]. The main requirement evolution for RES power plant operators in the weak grid is not only to smooth the power profile using an ESS but to provide the network operator with a day ahead production plan and thus be considered as a near conventional generator [36].

Additionally, an advanced information transmission system is necessary to enable large scale DG penetration. This need is addressed in the "*IEEE 2030-2011 Guide for Smart Grid Interoperability of Energy Technology and Information Technology Operation with the Electric Power System, and End-Use Applications and Loads*".

The large deployment of “smart meters” has become an opportunity to collect data for both operators to optimize energy dispatch, and users to reduce their consumption. The French national scale energy meters replacement by the Linky smart meter go in that way.

The IEEE 1547.4-2011 guide is the first (to the knowledge of the author) mainstream standard committee to take into account intentional and planned islands of a part of an electrical power system, often referring to MicroGrid (MG) concept.

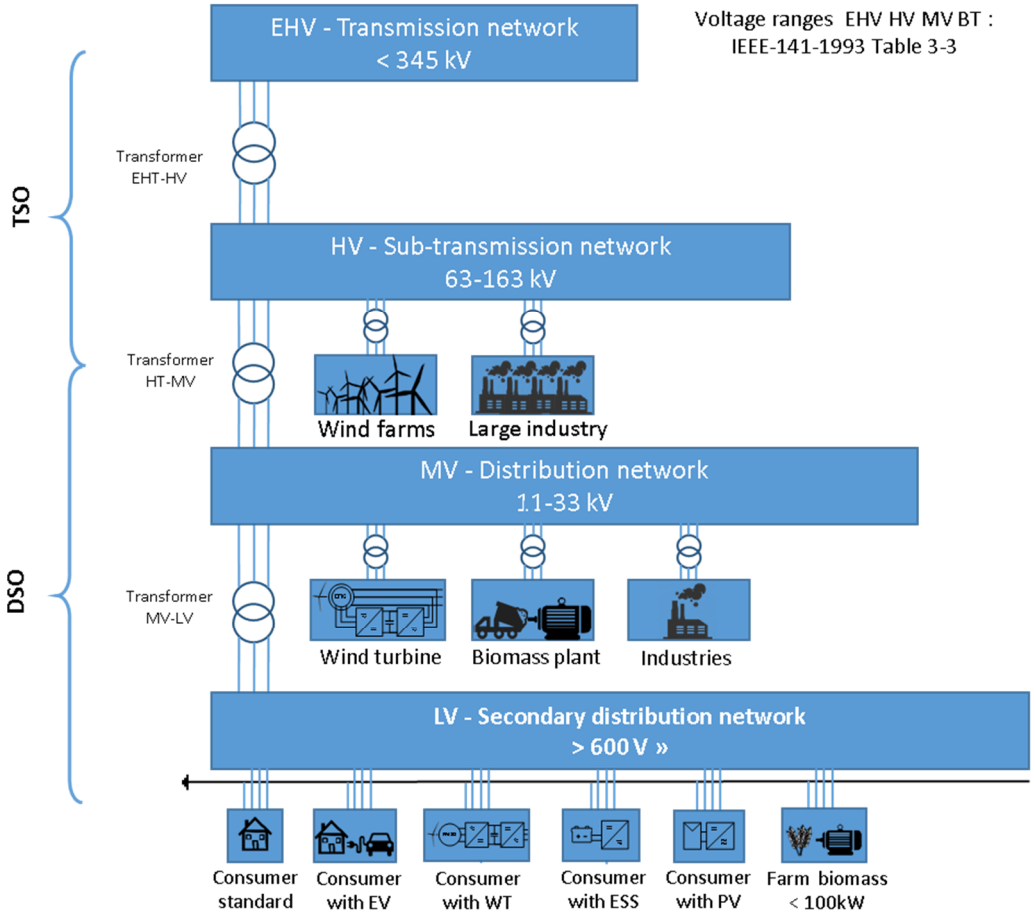

Figure 1.3: Standard current power system structure with DG

1.2 Microgrid and Virtual Power Plants

1.2.1 MG concept

1.2.1.1 Definition

The MG concept has emerged while a large number of DG have been implemented in distribution networks, causing the problems described in Section 1.1.3 [37]–[40]. It is defined by a group of sources, loads, storages and passive network components which are part of a power distribution system in a limited area, downstream from the distribution substation. The particularity of MG is that it can operate connected as well as disconnected from the main grid or other MGs [37], [38], [41].

MG concept has proven its ability to increase the Renewable Energy Source (RES) integration to the grid [39], [42]–[44]. The main drawback is the low short-circuit power of the MG while islanded mode which makes it weak, and thus very sensitive to active and reactive power variation [45]–[48]. Such issues can be drastically improved using ESS to support the MG operations and ensure its stability while improving power delivery quality [49]–[51].

Despite these drawbacks, MG is seen as a good candidate for large RES integration and even a 100% renewable energy mix. The recent development of this concept proposes a framework for practical implementation based on small to medium distribution networks using distributed agents for production scheduling and distributed ancillary services participation, like voltage and frequency regulation [52]. Although, the need for a dense measurement network and an advanced communication system is mandatory for this framework to come in practical use as detailed in section 1.1.4.

Finally, the analogy between an island grid and a MG is relevant as far as the RES integration is concerned, and we can even state that both are interleaved. Indeed, MG research contributes to island grid improvement by defining a framework for DG management in weak grid context, and inversely islands (connected or not to the mainland or another island) provide case studies and a possible industrial

deployment starting point thanks to the competitiveness of RES compared with conventional generation means [30], [35], [53], [54].

1.2.2 Virtual Power Plants

From the point of view of the DSO, a large penetration of DG cause planning issues leading to aforementioned power quality issues as well as increase both energy and economic losses, especially with large penetration of variable RES. The Virtual Power Plant (VPP) concept consists in aggregating various small size generating and storage units to form a "single virtual generating unit" that can behave as a conventional one [55], [56]. This concept emerged from the need to address economic and technical issues in distribution network planning while large DG penetration [56], [57]. Although it encompasses economic and technical tools for distribution planning, VPP is also a suitable framework to raise ancillary service from both generation side (primary/secondary frequency/voltage reserve) and demand side with Demand Response (DR) services that make aggregated loads controllable [11], [55], [57]–[61].

This concept can be scaled to suit different level needs. A hybrid power plant with several production means and storage capabilities can be considered as the lowest size VPP studied in the literature, often referring to Technical VPP (TVPP). It enables the coordination of the DG along with ESSs to provide production planning and scheduling, frequency and voltage regulation on a technical point of view and on a limited area and can be supervised by the DSO. On the other hand, the Commercial VPP (CVPP) is an economic framework suited to large networks and provides techniques for both economical dispatch optimization and distribution network losses reduction. It provides, as well, several recommendations for energy market structuration and management [62], especially for large storage capabilities offered by Electric Vehicle (EV) [63] and the flexibility offered by aggregated load control capabilities [64].

1.2.3 Current MG and VPP projects

Many research and industrial projects on MG and VPP concepts are currently put into practice on various scales. As mentioned previously, the MG concept is particularly suited to be implemented first in remote islands thanks to the competitiveness of RES compared with conventional gas/oil generation plants. Therefore numerous projects have been carried out in islands grids to implement a large proportion of RES. The following projects aim to increase the RES penetration using the MG research to support the industrial deployments.

- 60 European islands of the Pact of Island project (EU) [30], [53], [54], [65]
- Guadeloupe and Reunion islands (France) [66]
- Canary islands smart MicroGrid project (Spain) [30]
- Pantelleria island in the Mediterranean Sea (Italy) [54]
- Dongfushan island (China) [67]

Many other MG worldwide research projects and industrial demonstrators can be found in the literature:

- British Columbia Institute of Technology microgrid testbed [68]
- Microgrid testbed of Queensland University of Technology Australia [68]
- I-SARE project (Spain) [69]

The VVP concept is also put into practice on various scales in the following current or significant projects:

- FENIX project (EU) [57], [70]–[73]
- Bornholm island EDISON project (Danish) [11]
- Xiaozhongdian project (China) [74]

1.3 Energy Storage Systems in MG & VPP

Historically, pumped hydro has been implemented in centralized power systems thanks to the large capabilities and the fast response time of this type of ESS. It has enabled to store the energy of large power plants with slow response time and expensive starting costs like nuclear plants during low demand periods (typically during the night), and inject it during high demand periods.

Recent advances in electrochemical, electromechanical and electrostatic ESS technologies have drastically increased the efficiency, the lifetime, as well as specific power and energy, while both capital and operation expenditure decreased thanks to process improvements and large worldwide demand. The huge distributed power and energy that could be available with the massive deployment of EV and home ESSs, along with a market of ancillary services as theorized in the VPP framework, could consecrate the era of ESS as the keystone of future power systems [11].

In a MG with high penetration of RES, the weak nature of the power system can be mitigated by several means, like dispatch optimization and large active and reactive power primary reserve [42], [43], [60]. Although these solutions may tackle the weakness issues and improve MG stability, the use of small scale ESS instead can be competitive and improve the MG's efficiency, as well as the power quality [75]–[78]. Literature review shows that the latter solution is highly praised, despite technical challenges that still need to be addressed in terms of rare natural resources and recycling issues involved.

ESS is broadly seen as a mandatory technology to ensure the operation of a power system, especially with large RES penetration, and even more for a MG [79]–[81]. But the latter needs for both power and energy in order to ensure proper operation in both connected and especially in islanded mode is huge [82]. Thus, the literature shows that in a MG context an ESS should have high efficiency and power/energy capacity while showing fast response time and a good lifetime. Unfortunately, none of the currents ESS technologies offer such tradeoff. Thus the use of several ESSs technologies to realize a Hybrid Energy Storage System (HESS) is necessary to mitigate the drawback and enhance the advantage of each ESS technologies [83], [84].

The power electronic structures to integrate a ESS with an RES or to realize a HESS is the next challenge to address, as it will depend on a tradeoff between efficiency (how many power converters are used), flexibility (how deeply the ESSs can be used) and power quality (which topologies/techniques to use for low output harmonic, voltage unbalances cancellation, immunity to disturbances). The literature shows, for example, that ESSs can be integrated directly within the DG device/plant on the DC bus of a PV inverter or the back to back power converter

of wind turbines. In this configuration, the use of one or several DC/DC power converter can be necessary to control the power flow of the ESS(s), thus impacting the overall conversion chain.

1.4 Problem Statement

MG is a decentralized concept seen as a solution for high RES based DG integration into the grid. To ensure its stability and high power quality, the use of ESSs is mandatory, but none of the currently available technologies can offer the required specifications. Thus the use of HESS allows an increased specific energy/power and lifetime, as well as low response time which is an important requirement for MG with high shares of variable RES based DG.

The interface's structure between several ESSs, a RES and the grid is also a key point as it will impact the efficiency of the overall conversion chain, the power quality as well as flexibility and the lifetime of the HESS.

Moreover, ancillary services are required to ensure the proper operation of the MG, such as voltage and frequency regulation capabilities. The MG concept will also rely on the ability of the DG along with the HESS to take care of the unbalanced and critical load issues.

1.5 Objectives of the thesis

The objective of the thesis is to interface a RES along with a HESS to the grid with a unique power converter device while maintaining high power quality and enable ancillary services such as voltage and frequency regulation, as well as power filter capabilities. Using a single power converter allows decreasing losses compared with other classic solutions using several DC/DC and DC/AC power converters. The Three Level Neutral Point Clamped (3LNPC) multilevel topology is chosen to realize this interface for its increased power capabilities and reduced current output harmonic content and switching losses compared with a classic two-level inverter. Although using only one power converter benefits from the above-mentioned advantages, several issues have to be addressed to ensure proper

operation of this unique power electronic interface. In this thesis, a new model of the 3LNPC limits is proposed to assess the ability of the power converter to operate as an efficient and effective HESS and RES interface. A new nonlinear control strategy is designed and compared with classic control for HESS power flow control. Finally, a 4^{th} leg is added to the 3LNPC topology along with an AC side controller that operates both in connected and islanded mode for voltage and frequency regulation, voltage unbalances and harmonic cancelation.

The control strategies developed are tested by simulation means on Matlab/Simulink and using components available in the SimPowerSystem library. An experimental test bench composed of emulated DGs and ESSs is also used to reproduce a microgrid case study and asses the ability of the proposed control strategies to both feed and support the grid.

1.6 Thesis layout

- Chapter 2 : Energy Storage Hybridization
- Chapter 3 : HESS and RES interfacing
- Chapter 4 : Control of a 3L-NPC based HESS and RES multipurpose interface
- Chapter 5 : Experimental validation
- Chapter 6 : Conclusion

1.7 Chapter References

[1] R. Viral and D. K. Khatod, "Optimal planning of distributed generation systems in distribution system: A review," *Renew. Sustain. Energy Rev.*, vol. 16, no. 7, pp. 5146–5165, 2012.

[2] REN21, "Renewables 2019 global status report," 2019.

[3] T. Ackermann, G. Andersson, and L. Söder, "Distributed generation: a definition," *Electr. power Syst. Res.*, vol. 57, no. 3, pp. 195–204, Apr. 2001.

[4] R. Bayindir, M. A. Zamani, and J. Balcells, "Investigations Into the Control and Protection of an Existing Distribution Network to Operate as a Microgrid: A Case Study," *IEEE Trans. Ind. Electron.*, vol. 61, no. 4, pp. 1904–1915, Apr. 2014.

[5] G. Notton, *Problematic Integration of Fatal Renewable Energy Systems in Island Grids*. Springer International Publishing, 2016.

[6] F. H. Math H. Bollen, "Integration of Distributed Generation in the Power System," in *Integration of Distributed Generation in the Power System*, John Wiley & Sons, 2011, p. 524.

[7] A. Rouhani, S. H. Hosseini, and M. Raoofat, "Composite generation and transmission expansion planning considering distributed generation," *Int. J. Electr. Power Energy Syst.*, vol. 62, pp. 792–805, Nov. 2014.

[8] S. Islam, Y. K. Wu, and J. H. Lin, "Standards and Guidelines for Grid-connected Photovoltaic Generation Systems: a Review and Comparison," *IEEE Trans. Ind. Appl.*, vol. PP, no. 99, pp. 1–1, 2017.

[9] Y. Yang, P. Enjeti, F. Blaabjerg, and H. Wang, "Suggested grid code modifications to ensure wide-scale adoption of photovoltaic energy in distributed power generation systems," in *Conference Record - IAS Annual Meeting (IEEE Industry Applications Society)*, 2013, pp. 1–8.

[10] R. K. Sahu, S. Panda, and G. T. Chandra Sekhar, "A novel hybrid PSO-PS optimized fuzzy PI controller for AGC in multi area interconnected power systems," *Int. J. Electr. Power Energy Syst.*, vol. 64, pp. 880–893, Jan. 2015.

[11] H. Zhao, Q. Wu, S. Hu, H. Xu, and C. N. Rasmussen, "Review of energy storage system for wind power integration support," *Appl. Energy*, vol. 137,

pp. 545–553, Jan. 2015.

[12] F. Blaabjerg and K. Ma, "Future on Power Electronics for Wind Turbine Systems," *IEEE J. Emerg. Sel. Top. Power Electron.*, vol. 1, no. 3, pp. 139–152, Sep. 2013.

[13] C. N. Rasmussen and H. Fujita, "Voltage-Regulation Performance of a Shunt Active Filter Intended for Installation on a Power Distribution System," *IEEE Trans. Power Electron.*, vol. 22, no. 3, pp. 1046–1053, May 2007.

[14] D. Heredero-Peris, M. Pages-Gimenez, and D. Montesinos-Miracle, "Inverter design for four-wire microgrids," in *2015 17th European Conference on Power Electronics and Applications, EPE-ECCE Europe 2015*, 2015, pp. 1–10.

[15] J. M. Guerrero, J. C. Vasquez, J. Matas, L. G. de Vicuña, and M. Castilla, "Hierarchical Control of Droop-Controlled AC and DC Microgrids #x2014;A General Approach Toward Standardization," *IEEE Trans. Ind. Electron.*, vol. 58, no. 1, pp. 158–172, Jan. 2011.

[16] B. Ghullam Mustafa, B.-J. Birgitte, M. Pukar, and C. Carlo, "Mitigation of Unbalanced Voltage Sags and Voltage Unbalance in CIGRE Low Voltage Distribution Network," *Energy Power Eng.*, vol. 2013, Nov. 2013.

[17] F. Hassan *et al.*, "Review of existing reactive power requirements for variable generation," 2012, pp. 1–7.

[18] A. Susperregui, L. Xu, M. I. Martinez, and G. Tapia, "Sliding-mode control of a wind turbine-driven double-fed induction generator under non-ideal grid voltages," *IET Renew. Power Gener.*, vol. 7, no. 4, pp. 370–379, 2013.

[19] M. C. Kisacikoglu, B. Ozpineci, and L. M. Tolbert, "Effects of V2G reactive power compensation on the component selection in an EV or PHEV bidirectional charger," 2010, pp. 870–876.

[20] M. C. Kisacikoglu, B. Ozpineci, and L. M. Tolbert, "Examination of a PHEV bidirectional charger system for V2G reactive power compensation," in *Applied Power Electronics Conference and Exposition (APEC), 2010 Twenty-Fifth Annual IEEE*, 2010, pp. 458–465.

[21] R. H. Lasseter, "Smart distribution: Coupled microgrids," in *Proceedings of the IEEE*, 2011, vol. 99, no. 6, pp. 1074–1082.

[22] M. H. Namin and V. G. Agelidis, "Voltage sensitivity study of LV/MV networks under high penetration of photovoltaic generation considering residential and industrial load profiles," in *Photovoltaic Specialists Conference (PVSC), 2013 IEEE 39th*, 2013, pp. 2309–2314.

[23] C. M. Colson and M. H. Nehrir, "A review of challenges to real-time power management of microgrids," in *IEEE Power and Energy Society General Meeting*, 2009, pp. 1–8.

[24] H. Wang, P. Wang, and T. N. Preda, "An overview of the present grid codes for integration of distributed generation," 2012, pp. 1–4.

[25] B. Ghullam Mustafa, *Control and Protection in Low Voltage Grid with large scale renewable electricity generation*. 2014.

[26] M. Liserre, T. Sauter, and J. Y. Hung, "Future Energy Systems: Integrating Renewable Energy Sources into the Smart Power Grid Through Industrial Electronics," *IEEE Ind. Electron. Mag.*, vol. 4, no. 1, pp. 18–37, Mar. 2010.

[27] P. Jahangiri, "Voltage and reactive power regulation by photovoltaics in distribution systems," 2014.

[28] R. Shah, N. Mithulananthan, R. C. Bansal, and V. K. Ramachandaramurthy, "A review of key power system stability challenges for large-scale PV integration," *Renew. Sustain. Energy Rev.*, vol. 41, pp. 1423–1436, Jan. 2015.

[29] M. Barghi Latran and A. Teke, "Investigation of multilevel multifunctional grid connected inverter topologies and control strategies used in photovoltaic systems," *Renewable and Sustainable Energy Reviews*, vol. 42. pp. 361–376, Feb-2015.

[30] A. Colmenar-Santos, O. Monzón-Alejandro, D. Borge-Diez, and M. Castro-Gil, "The impact of different grid regulatory scenarios on the development of renewable energy on islands: A comparative study and improvement proposals," *Renew. Energy*, vol. 60, pp. 302–312, Dec. 2013.

[31] G. Xydis, "Comparison study between a Renewable Energy Supply System and a supergrid for achieving 100% from renewable energy sources in Islands," *Int. J. Electr. Power Energy Syst.*, vol. 46, pp. 198–210, Mar. 2013.

[32] D. Marín, "Intégration des éoliennes dans les réseaux électriques insulaires," *Thesis*, 2009.

[33] G. Notton, "Importance of islands in renewable energy production and storage: The situation of the French islands," *Renew. Sustain. Energy Rev.*, vol. 47, pp. 260–269, Jul. 2015.

[34] République Française, "Arrêté du 23 avril 2008 relatif aux prescriptions techniques de conception et de fonctionnement pour le raccordement à un réseau public de distribution d'électricité en basse tension ou en moyenne tension d'une installation de production d'énergie électri," *J. Off. la République Française*, vol. 98, 2011.

[35] G. Notton, L. Stoyanov, M. Ezzat, V. Lararov, S. Diaf, and C. Cristofari, "Integration Limit of Renewable Energy Systems in Small Electrical Grid," *Energy Procedia*, vol. 6, pp. 651–665, 2011.

[36] IEC, "Grid integration of large-capacity Renewable Energy sources and use of large-capacity Electrical Energy Storage," 2008.

[37] F. Katiraei, R. Iravani, N. Hatziargyriou, and A. Dimeas, "Microgrids management," *IEEE Power Energy Mag.*, vol. 6, no. 3, pp. 54–65, May 2008.

[38] R. H. Lasseter and P. Paigi, "Microgrid: A conceptual solution," in *PESC Record - IEEE Annual Power Electronics Specialists Conference*, 2004, vol. 6, pp. 4285–4290.

[39] Xuan Liu and Bin Su, "Microgrids - an integration of renewable energy technologies," in *2008 China International Conference on Electricity Distribution*, 2008, pp. 1–7.

[40] R. H. Lasseter, "MicroGrids," in *2002 IEEE Power Engineering Society Winter Meeting. Conference Proceedings (Cat. No.02CH37309)*, 2002, vol. 1, pp. 305–308.

[41] Y. Guan, P. Paigi, and M. R. Iravani, "Micro-grid autonomous operation during and subsequent to islanding process," *IEEE Trans. Power Deliv.*, vol. 20, no. 1, pp. 248–257, Jan. 2005.

[42] F. F. Yanine and E. E. Sauma, "Review of grid-tie micro-generation systems without energy storage: Towards a new approach to sustainable hybrid energy systems linked to energy efficiency," *Renew. Sustain. Energy Rev.*, vol. 26, pp. 60–95, Oct. 2013.

[43] A. Rezvani, M. Gandomkar, M. Izadbakhsh, and A. Ahmadi,

"Environmental/economic scheduling of a micro-grid with renewable energy resources," *J. Clean. Prod.*, vol. 87, pp. 216–226, 2015.

[44] R. Hemmati and H. Saboori, "Emergence of hybrid energy storage systems in renewable energy and transport applications – A review," *Renew. Sustain. Energy Rev.*, vol. 65, pp. 11–23, Nov. 2016.

[45] S. Baudoin, I. Vechiu, and H. Camblong, "A review of voltage and frequency control strategies for islanded microgrid," in *System Theory, Control and Computing (ICSTCC), 2012 16th International Conference on*, 2012, pp. 1–5.

[46] F. Katiraei and M. R. Iravani, "Power Management Strategies for a Microgrid With Multiple Distributed Generation Units," *IEEE Trans. Power Syst.*, vol. 21, no. 4, pp. 1821–1831, Nov. 2006.

[47] J. M. Guerrero, M. Chandorkar, T. Lee, and P. C. Loh, "Advanced Control Architectures for Intelligent Microgrids - Part I: Decentralized and Hierarchical Control," *IEEE Trans. Ind. Electron.*, vol. 60, no. 4, pp. 1254–1262, Apr. 2013.

[48] H. Bevrani, B. François, and T. Ise, *Microgrid Dynamics and Control*. John Wiley & Sons, 2017.

[49] L. Barote, C. Marinescu, and M. Georgescu, "VRB modeling for storage in stand-alone wind energy systems," in *PowerTech, 2009 IEEE Bucharest*, 2009, pp. 1–6.

[50] S. Faias, P. Santos, J. Sousa, and R. Castro, "An overview on short and long-term response energy storage devices for power systems applications," *System*, vol. 5, p. 6, 2008.

[51] W. Wang, B. Ge, D. Bi, M. Qin, and W. Liu, "Energy storage based LVRT and stabilizing power control for direct-drive wind power system," in *2010 International Conference on Power System Technology: Technological Innovations Making Power Grid Smarter, POWERCON2010*, 2010, pp. 1–6.

[52] E. Amicarelli, T. Q. Tran, and B. Seddik, "Flexibility service market for active congestion management of distribution networks using flexible energy resources of microgrids," in *2017 IEEE PES Innovative Smart Grid Technologies Conference Europe (ISGT-Europe)*, 2017, pp. 1–6.

[53] E. Riva Sanseverino, R. Riva Sanseverino, S. Favuzza, and V. Vaccaro, "Near zero energy islands in the Mediterranean: Supporting policies and local obstacles," *Energy Policy*, vol. 66, pp. 592–602, Jun. 2014.

[54] V. Franzitta, D. Curto, D. Rao, and D. Milone, "Near zero energy island with sea wave energy: The case study of Pantelleria in Mediterranean Sea," in *OCEANS 2016 - Shanghai*, 2016, pp. 1–5.

[55] H. Saboori, M. Mohammadi, and R. Taghe, "Virtual power plant (VPP), definition, concept, components and types," in *Asia-Pacific Power and Energy Engineering Conference, APPEEC*, 2011, pp. 1–4.

[56] C. Kieny, B. Berseneff, N. Hadjsaid, Y. Besanger, and J. Maire, "On the concept and the interest of virtual power plant: Some results from the European project Fenix," *IEEE Power Energy Soc. Gen. Meet.*, pp. 1–6, Jul. 2009.

[57] D. Pudjianto, C. Ramsay, and G. Strbac, "Virtual power plant and system integration of distributed energy resources," *IET Renew. Power Gener.*, vol. 1, no. 1, pp. 10–16, Mar. 2007.

[58] V. Fernão Pires, E. Romero-Cadaval, D. Vinnikov, I. Roasto, and J. F. Martins, "Power converter interfaces for electrochemical energy storage systems - A review," *Energy Convers. Manag.*, vol. 86, pp. 453–475, Oct. 2014.

[59] P. Faria and M. Raoofat, "Remuneration structure definition for distributed generation units and demand response participants aggregation," 2014, pp. 1–5.

[60] S. M. Nosratabadi, R. A. Hooshmand, and E. Gholipour, "A comprehensive review on microgrid and virtual power plant concepts employed for distributed energy resources scheduling in power systems," *Renewable and Sustainable Energy Reviews*, vol. 67. pp. 341–363, Jan-2017.

[61] G. Papadakis, N. Ruiz, and I. Cobelo, "A Direct Load Control Model for Virtual Power Plant Management," *IEEE Trans. Power Syst.*, vol. 24, no. 2, pp. 959–966, May 2009.

[62] E. Kruger, E. Amicarelli, and Q. T. Tran, "Impact of European market frameworks on integration of photovoltaics in virtual power plants," in *EEEIC 2016 - International Conference on Environment and Electrical Engineering*, 2016, pp. 1–6.

[63] C. Quinn, D. Zimmerle, and T. H. Bradley, "The effect of communication architecture on the availability, reliability, and economics of plug-in hybrid electric vehicle-to-grid ancillary services," *J. Power Sources*, vol. 195, no. 5, pp. 1500–1509, Mar. 2010.

[64] H. Yujun, "Contribution au réglage de la tension sur un réseau HTA avec producteurs. Apport de la flexibilité de la demande," pp. 1–125, 2015.

[65] Y. Kuang *et al.*, "A review of renewable energy utilization in islands," *Renew. Sustain. Energy Rev.*, vol. 59, pp. 504–513, Jun. 2016.

[66] A. A. Renjit, F. Guo, and R. Sharma, "An analytical framework to design a Dynamic Frequency Control scheme for microgrids using energy storage," in *2016 IEEE Applied Power Electronics Conference and Exposition (APEC)*, 2016, pp. 1682–1689.

[67] B. Zhao, X. Zhang, P. Li, K. Wang, M. Xue, and C. Wang, "Optimal sizing, operating strategy and operational experience of a stand-alone microgrid on Dongfushan Island," *Applied Energy*, vol. 113. pp. 1656–1666, Jan-2014.

[68] E. Hossain, E. Kabalci, R. Bayindir, and R. Perez, "Microgrid testbeds around the world: State of art," *Energy Convers. Manag.*, vol. 86, pp. 132–153, Oct. 2014.

[69] "I-SARE." [Online]. Available: http://www.i-sare.net/. [Accessed: 03-Jul-2017].

[70] E. Mashhour and S. M. Moghaddas-Tafreshi, "Bidding strategy of virtual power plant for participating in energy and spinning reserve markets-Part I: Problem formulation," *IEEE Trans. Power Syst.*, vol. 26, no. 2, pp. 949–956, May 2011.

[71] B. Berseneff and B. B. R, "Réglage de la tension dans les réseaux de distribution du futur," 2011.

[72] E. Mashhour and S. M. Moghaddas-Tafreshi, "Bidding Strategy of Virtual Power Plant for Participating in Energy and Spinning Reserve Markets #x2014;Part I: Problem Formulation," *IEEE Trans. Power Syst.*, vol. 26, no. 2, pp. 949–956, May 2011.

[73] "FENIX PROJECT." [Online]. Available: http://www.fenix-project.org/. [Accessed: 09-May-2016].

[74] L. Ju, Z. Tan, J. Yuan, Q. Tan, H. Li, and F. Dong, "A bi-level stochastic scheduling optimization model for a virtual power plant connected to a wind-photovoltaic-energy storage system considering the uncertainty and demand response," *Appl. Energy*, vol. 171, pp. 184–199, Jun. 2016.

[75] N. Hajilu, G. B. Gharehpetian, S. H. Hosseinian, M. R. Poursistani, and M. Kohansal, "Power control strategy in islanded microgrids based on VF and PQ theory using droop control of inverters," 2015, pp. 37–42.

[76] M. A. Bin Roslan, S. R. S, and A. Prasad, "Control and operation of microgrid connected Hybrid Energy Storage System," 2016, pp. 356–360.

[77] I. Vechiu, A. Etxeberria, H. Camblong, and Q. Tabart, "Control of a microgrid-connected hybrid energy storage system," in *Renewable Energy Research and Application (ICRERA), 2014 International Conference on*, 2014, pp. 412–417.

[78] X. Luo, J. Wang, M. Dooner, and J. Clarke, "Overview of current development in electrical energy storage technologies and the application potential in power system operation," *Appl. Energy*, vol. 137, pp. 511–536, Jan. 2015.

[79] M. Yekini Suberu, M. Wazir Mustafa, and N. Bashir, "Energy storage systems for renewable energy power sector integration and mitigation of intermittency," *Renew. Sustain. Energy Rev.*, vol. 35, pp. 499–514, Jul. 2014.

[80] S. Vazquez, S. M. Lukic, E. Galvan, L. G. Franquelo, and J. M. Carrasco, "Energy Storage Systems for Transport and Grid Applications," *IEEE Trans. Ind. Electron.*, vol. 57, no. 12, pp. 3881–3895, Dec. 2010.

[81] M. G. Molina and P. E. Mercado, "Power Flow Stabilization and Control of Microgrid with Wind Generation by Superconducting Magnetic Energy Storage," *IEEE Trans. Power Electron.*, vol. 26, no. 3, pp. 910–922, Mar. 2011.

[82] S. X. Chen, H. B. Gooi, and M. Q. Wang, "Sizing of energy storage for microgrids," *IEEE Trans. Smart Grid*, vol. 3, no. 1, pp. 142–151, Mar. 2012.

[83] X. Tan, Q. Li, and H. Wang, "Advances and trends of energy storage technology in Microgrid," *Int. J. Electr. Power Energy Syst.*, vol. 44, no. 1, pp. 179–191, Jan. 2013.

[84] N. R. Tummuru, M. K. Mishra, and S. Srinivas, "Dynamic Energy Management of Renewable Grid Integrated Hybrid Energy Storage System," *IEEE Trans. Ind. Electron.*, vol. 62, no. 12, pp. 7728–7737, Dec. 2015.

Chapter 2

Energy Storage Hybridization

Contents

2.1 Trend on ESS technologies

In the past decade, the demand for ESS technologies has increased drastically. The need for reliable, efficient, large and cost-effective ESS solutions has received close attention from both the industrial and the academic community as can be seen in Figure 2.1. New technologies combined with significant improvement in material science have led to the emergence of a dynamic global ESS market. ESS technologies show drastic differences in term of characteristics, performances, and costs. Depending on the application purpose, ESS technology selection may take into account different technical and economical parameters. The economic and environmental issues being very high, bad design or the use in wrong operating conditions may significantly reduce both ESS performance and economical profitability. Thus, in this chapter, different ESSs technologies are characterized and a comparison of technologies, performances, and economics is carried out. This study shows that a single ESS technology can rarely meet all requirements itself, especially in a versatile application. Different services using ESS for grid applications are also detailed, along with suitable ESS technologies. Finally, couples of ESSs to realize high efficiency and performance Hybrid Energy Storage Systems (HESS) is proposed.

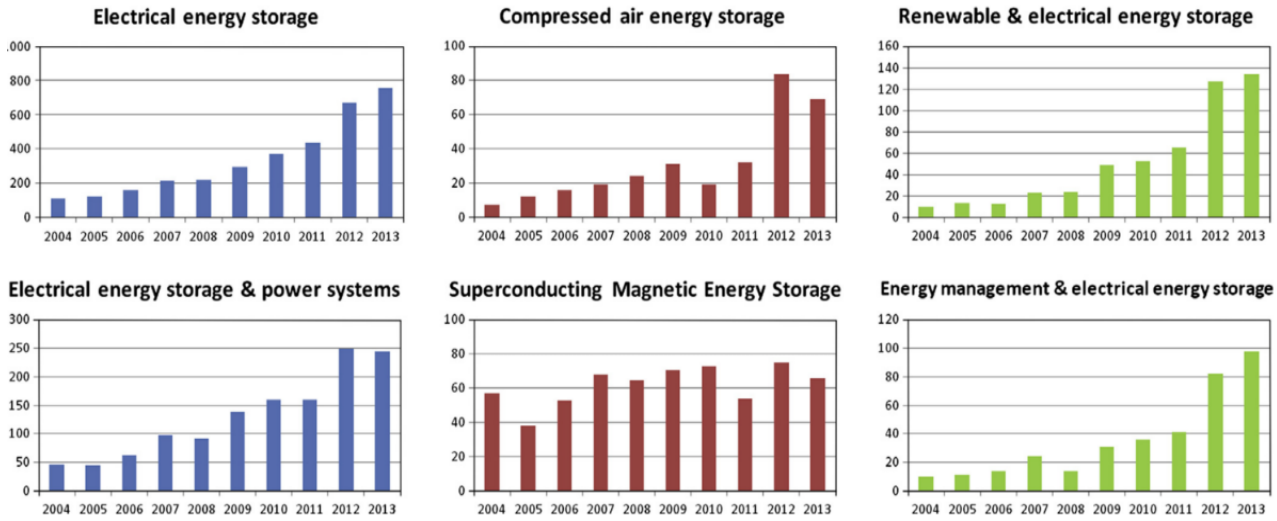

Figure 2.1 ESS technologies academic publication trends [1]

2.1.1 Electrochemical

Electrochemical energy storage converts the chemical energy contained in its active materials into electric energy by an electrochemical oxidation-reduction reverse reaction. This type of ESS constitute a large group of technologies thanks to the multiple possible technological implementations for these oxidation-reduction reactions to occur. Each of these presents different characteristics, advantages, and drawbacks, and can be classified as in the following sections.

2.1.1.1 Static electrolyte ESS

Static ESS technologies are composed of a solid electrode and/or liquid electrolyte, often packaged in batteries of cells in series to obtain a standard DC voltage. There are many of oxidation-reduction couples available in the literature, but the following are mainstream technologies used in the industry and are a significant example of how the technology employed affects the characteristics of the battery.

- Lead-Acid (LA)
- Nickel-Cadmium (Ni-Cd)
- Sodium-Sulfur (Na-S)
- Lithium-Ion (Li-Ion)

Figure 2.2 presents the architecture of a Lead Acid (LA) battery, which is very similar to other common architecture of a static electrolyte ESS with liquid electrolytes. LA batteries when compared to another electrochemical sources has many advantages. Its low price and the lead availability, a good reliability, a high cell voltage (2 V), a good electrochemical efficiency, and a lifetime from several hundreds to thousands of cycles [1], [2]. Thanks to these characteristics it is now the most widely used electrochemical source of electric energy and represents about 60% of installed power from all types of batteries. Its main drawback is the weight of lead and consequently, lower specific energy in the range 30-50 Wh/kg.

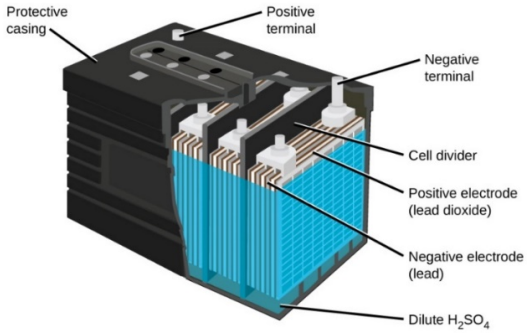

Figure 2.2 Architecture of a Lead Acid battery pack

Ni-Cd batteries on the other hand suffer from a low cell voltage (1.2V), a quite high self-discharge rate and the memory effect compared with LA batteries. Thus this oxidation-reduction couple is employed in a specific application where robustness, deep discharge rates, and good efficiency is needed. Although the higher specific energy and energy density compared with LA makes this ESS technology suitable for both stationary and embedded applications, the high price and the recycling issues involved by the nickel and cadmium electrodes do not allow economy of scale for large stationary applications [1], [3].

On the contrary, Na-S batteries benefit from easy economy of scale thanks to the abundance of the raw materials. The very high efficiency and long cycle life make it a very good ESS technology for large standalone applications, especially for grid support. But the high operating temperature and the corrosiveness of the sodium makes this technology hazardous. Still, this ESS technology is nowadays industrially mature and cheap enough to be deployed in large scale applications [1]–[3].

Finally, the Li-Ion has received a lot of attention this last decade for grid application thanks to its remarkable characteristics, particularly its very high specific power and energy as well as its superior power and energy density compared with all aforementioned ESS technologies. Therefore, the interest in an embedded application such as electric vehicles has boosted the interest of industrials and therefore reached competitive prices thanks to economy of scale. Worldwide projects are already using this technology for grid purpose, and recent manufacturer announcement may increase even further the Li-Ion ESS market capacity [1]–[3].

Project Name, location	Technology	Rated Power [MW]	Rated Energy [MWh]	Application
BEWAG, Berlin [1]	LA	8.5	8.5	Frequency Control
Chino, California	LA	10	40	Load Leveling
PREPA, Puerto Rico	LA	20	14	Frequency Control
Metlakatla, Alaska	LA	1	1.4	Frequency Control
Graciosa Island, Germany	Na-S	3	18	Wind & PV Peak shaving
Rokkasho Wind Farm, Japan	Na-S	34	244.8	Wind Leveling
PEGASE, Reunion	Na-S	1	7.2	PV Peak shaving
ILIS, Tudela	Li-Ion	1.1	0.56	PV Leveling
STORE, Canaria's Island	Li-Ion	1	3	Wind & PV Leveling
MILLENER, Corsica, Guadeloupe, Reunion Islands	Li-Ion	29	29	PV Plant Leveling

Table 2.1: Example of Electrolytic ESS facilities for grid application

A characteristic shared by all aforementioned ESSs technologies is that to reach high voltages several element have to be put in series. With time, the SOC of each individual cell will differ because of small differences in the chemistry and it is necessary to use a Battery Management System (BMS) that will, among other things, balance each cell of the branch to insure a proper operation of the battery pack. Most BMS technologies balance the voltage of each cell in order to have a homogenous charge/discharge cycles [4].

2.1.1.2 Fuel Cells

A fuel cell is an electrochemical cell that converts the chemical energy from a fuel into electricity through an electrochemical reaction of hydrogen-containing fuel with oxygen, or another oxidizing agent. Fuel cells require a continuous flow of fuel and oxygen (usually from air) to sustain the chemical reaction, thus producing electricity continuously for as long as fuel and oxygen are supplied.

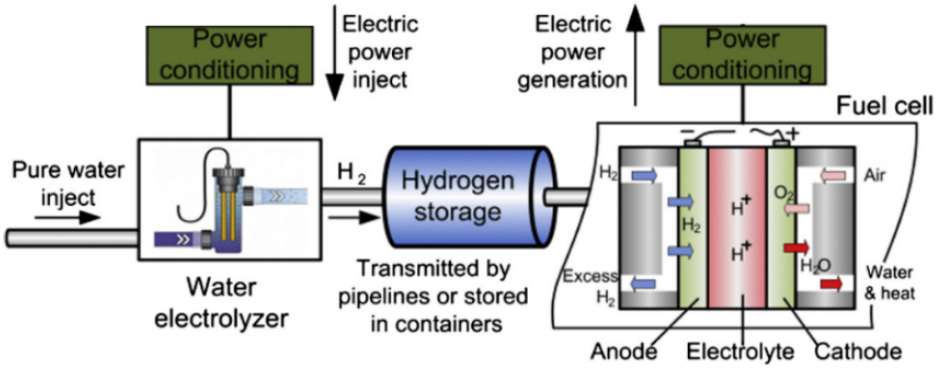

Figure 2.3 Fuel Cell / Electrolyze energy storage schematic diagram [1]

There are many types of fuel cells, but they all consist of an anode, a cathode, and an electrolyte that allows positively charged hydrogen ions (protons) to move between the two sides of the fuel cell. At the anode a catalyst causes the fuel to undergo oxidation reactions that generate protons (positively charged hydrogen ions) and electrons. The protons flow from the anode to the cathode through the electrolyte after the reaction. At the same time, electrons are drawn from the anode to the cathode through an external circuit, producing direct current supply. At the cathode, another catalyst causes hydrogen ions, electrons, and oxygen to react, forming water. Fuel cells are classified by the type of electrolyte they use and by the difference in start-up time ranging from 1 second for Proton Exchange Membrane Cell Cells (PEMFC) to 10 minutes for solid oxide fuel cells (SOFC) that operate at high temperature. The list below shows the main fuels and electrolytes used in fuel cell ESS technologies.

- Proton exchange membrane fuel cells (PEMFCs)
- Solid Oxide Fuel Cell (SOFC)
- Phosphoric acid fuel cell (PAFC)
- Solid acid fuel cell (SAFC)
- Alkaline fuel cell (AFC)

The most deployed fuel cell technologies both in research projects and in the industry are currently the PEMFC and SOFC. Several significant projects that are representatives of the rated power and energy range that this ESS technology may reach are listed in Table 2.2.

Project Name, location	Technology	Rated Power [MW]	Rated Energy [MWh]	Application
MYRTE, Corsica [5]	PEMFC	0.21	0.5	PV Peak Shaving
Santa Rita Jail, California [6]	SOFC	5	-	Microgrid application

Table 2.2: Example of Fuel Cell ESS technology facilities in grid application

2.1.1.3 Redox Flow Batteries

Flow batteries store and release electrical energy with the help of reversible electrochemical reactions in two liquid electrolytes. An electrochemical cell has two loops physically separated by an ion or proton exchange membrane. Electrolytes flow into and out of the cell through separate loops and undergo chemical reaction inside the cell, with ion or proton exchange through the membrane and electron exchange through the external electric circuit. There are some advantages to using the flow battery when compared with a conventional secondary battery. The capacity of the system has the ability to scale by increasing the amount of solution in electrolyte tanks. The battery can be fully discharged and has little loss of electrolyte during cycling. Because the electrolytes are stored separately, flow batteries have a low self-discharge. The disadvantage is a low energy density and specific energy [1]–[3], [7].

- Vanadium Redox Flow Battery (VRB)
- Polysulfide Bromine (PSB)
- Zinc Bromine (ZnBr)

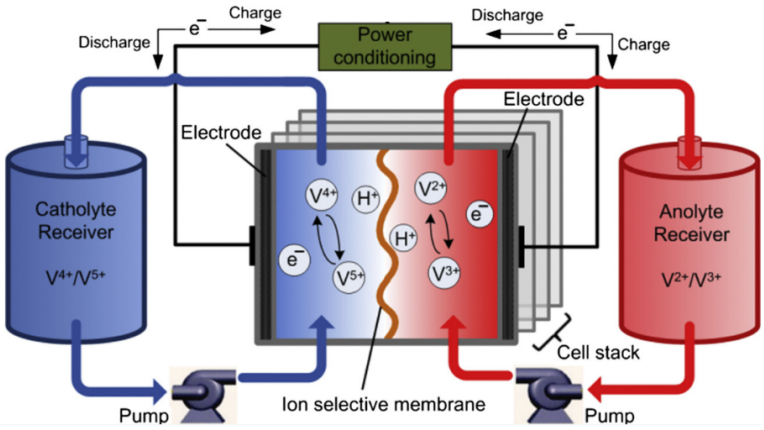

Figure 2.4 Vanadium Redox Flow Battery schematic diagram [1]

Project Name, location	**Technology**	**Rated Power** [MW]	**Rated Energy** [MWh]	**Application**
Kwansei University , Japan [8]	VRB	0.5	5	Frequency Control
Oxnard, USA [9]	VRB	0.6	3.6	Peak shaving
Wind Farm EES project, Ireland	VRB	2	12	Load levelling
Little Barford, UK [8]	PSB	15	120	Load levelling
TSA, Mississippi , USA [8]	PSB	12	120	Load levelling
Kyushu EPC, Japan [10]	ZnBr	1	4	Peak shaving

Table 2.3: Example of Fuel Cell ESS facilities in grid application

2.1.2 Electrostatic

In this kind of ESS, there is no transformation of energy as it is stored electrically by means of an electric field between two electrodes. The inconvenience of this ESS technology lies in the very high power capabilities and very low rated energy. Due to the internal losses of the electrostatic ESS device, self-discharge is generally very high. In contrast, the lifetime of such a device will be very long as there are no moving parts or chemical reaction. Figure 2.5 represents the schematic diagram of a double layer capacitor. The main devices storing energy in an electrostatic form are Capacitor and the Super Capacitor (SC). It should be noted that like electrochemical ESSs, high voltages can be reached using several elements in series. The use of a BMS is necessary to insure a proper operation of the device but also to maximise its lifetime [11].

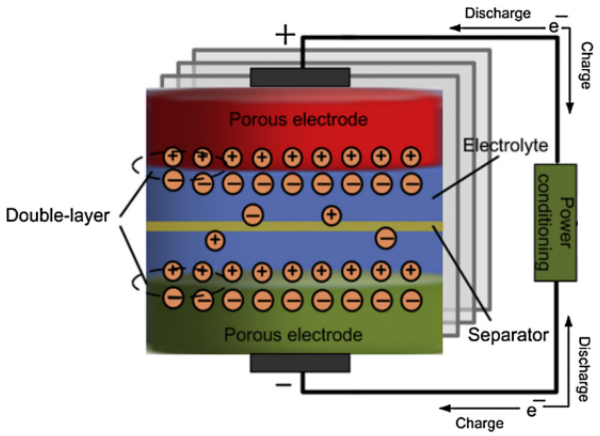

Figure 2.5 Double Layer Capacitor schematic diagram [1]

Project Name, location	Technology	Rated Power [MW]	Rated Energy [MWh]	Application
Deep Water Port, Shanghai [12]	SC	3	0.017.2	Transmission Line Support
Oahu island, Hawaiian [13]	SC	10	-	Wind power smoothing

Table 2.4: Example of Electrostatic ESS technology facilities in grid application

2.1.3 Electromechanic

Energy can be stored as a mechanical form either as a kinetic or potential mechanical energy. Unlike kinetic energy storage, which uses the motion of a mass (rotation or translation) to store energy, potential energy can be expressed by different means. The two major types of potential energy are gravitational and elastic. The gravitational potential energy is the consequence of a mass in a gravitational field, which while moved will release or consume energy. In a different way, elastic potential energy uses the deformation of either a solid (spring) or a liquid/gas (water or air) to store energy. The list below shows several ESS technologies using kinetic and potential energy storage:

- Pumped Hydro Energy Storage (PHES)
- Flywheel (FW)
- Compressed Air Energy Storage (CAES)

PHES stores energy in the form of gravitational potential energy of water pumped from a lower reservoir to a higher reservoir. This ESS technology has been historically the first large scale ESS technology developed thanks to the large capacity of such installation, the relatively high performance and low startup time which is widely used to store the energy from nuclear plants during low consumption periods, and support the grid during the peaks [14].

CAES works on the basis of conventional gas turbine generation. It decouples the compression and expansion cycles of a conventional gas turbine into two separated processes and stores the energy in the form of elastic potential energy of compressed air. Even though most CAES plants developed so far use fuel like natural gas during generation stage, it is still considered a potential large scale and sustainable ESS technology mainly because the recent development of

adiabatic CAES shows that better efficiency can be reached without using an external source of heat based on fossil fuel [15]. Figure 2.6 shows the schematic diagram of a diabatic CAES plant.

Finally the FW technology uses a motor/generator to store kinetic energy in a spinning mass. This technology has many advantages like a very good lifecycle, high power density and efficiency, but it suffers from a high self-discharge and from scalability issues [16].

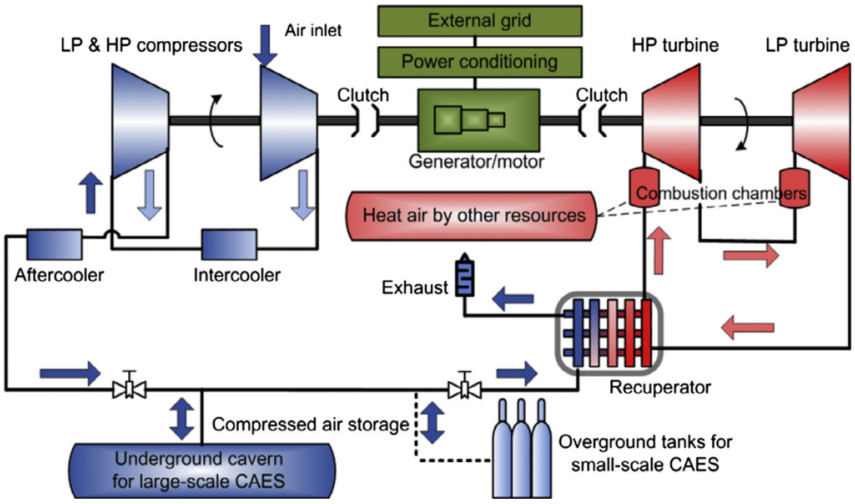

Figure 2.6 CAES schematic diagram [1]

Project Name, location	**Technology**	**Rated Power** [MW]	**Rated Energy** [MWh]	**Application**
Grand'Maison, France [17]	PHES	1800	316 500	Load Leveling, Frequency
Ikaria Island, Greece [1]	PHES	2.65	-	Load Leveling, Frequency
Larne, Ireland [18]	CAES	330	1 980	Load Leveling, Frequency
Norton, Ohio, USA [15], [19]	CAES	800	43 200	Load Leveling, Frequency

Table 2.5: Example of Electromechanical ESS technology facilities in grid application

2.1.4 Electromagnetic

Superconducting Magnetic Energy Storage (SMES) systems store energy in the magnetic field created by the flow of a direct current in a superconducting coil. This superconducting coil is cryogenically cooled to a temperature below its critical

temperature and thus losses are limited to the auxiliary systems which means SMES technology is very efficient. The low response time and high power capability of such ESS make it very attractive for power quality and stability purposes [1]. Table 2.6 displays some SMES application characteristics.

Project Name, location	Technology	Rated Power [MW]	Rated Energy [MWh]	Application
Liquid crystal factory, Japan [20]	SMES	5	0.002	Power quality
2 GJ Class YBCO, Japan [21]	SMES	100	0.667	Power System Stabilizer
Hosoo power station, Japan [22]	SMES	100	5.55	Wind Power Leveling
Upper Wisconsin TSO, USA [1]	SMES	3	0.83	Power quality

Table 2.6: Example of Electromagnetic ESS technology facilities in grid application

2.2 ESSs technologies comparison

From the above ESS technologies description, it is clear that every ESS technology has different drawbacks and advantages. To compare ESS technologies it is necessary to define criteria. The following list shows the main criteria used to describe ESS technology:

- Rated power (MW): maximum power that an ESS can release/store.
- Rated energy (MWh): maximum energy quantity that an ESS can store.
- Specific power (W/kg): the power of the ESS per mass unit.
- Specific energy (Wh/kg): the capacity of the ESS per mass unit.
- Power density (W/l): the power of the ESS per volume unit.
- Energy density (Wh/l): the capacity of the ESS per volume unit.
- Power capital cost: the cost of the ESS per power unit.
- Energy capital cost: the cost of the ESS per energy unit.
- Life time/cycle life: defines the life time/number of cycles of an ESS.
- Self-discharge: defines the energy losses of an ESS during non-use time.
- Round-trip efficiency: the ratio between the energy stored and released.
- Response time: the time needed by the ESS to reach the rated power.

Moreover, additional constraints have to be taken into account to ensure proper operation of some ESS technologies. These constraints vary and depend on the technology. As an example, the maximum Depth of Discharge (DOD) constraint

on Li-Ion ESS should be fulfilled to avoid premature failure of the ESS. The main constraints to take into account for a normal ESS operation are the following:

- Maximum DOD (%): lower state of charge allowed
- Temperature range (°C): maximum and minimum operation temperatures
- Power gradient (W/s): maximum admitted power variation

2.2.1 Technological comparison

The abundance of ESS technologies available result in a wide area covered for criteria such as specific power/energy and density. Table 2.7 presents a recent review of these criteria for a large panel of ESS technologies. Figure 2.7 and Figure 2.8 present these results in graphs. These figures allow an estimation of the weight and volume of large ESS in grid applications to be calculated. For example, considering the highest specifications available, a 1MWh Li-Ion ESS would weight approximatively 5 tons for 2 m^3 volume. These last figures illustrate how Li-Ion technology is particularly interesting as it reaches both the highest specific power/energy and density among all other electrochemical ESS technologies apart from fuel cells.

Using these values, these ESS technologies can be classified in three distinct groups. power-oriented ESS technologies which includes the SC, FW and SMES; energy-oriented like fuel cells and flow batteries along with PHES and CAES; and versatile headed by Li-ion and followed by all others static electrolyte subgroup (LA, NiCd, NaS) which shows balanced power and energy abilities.

Unlike versatile and power-oriented ESS technologies, energy-oriented ESSs are characterized by a power decoupled from the energy. As such, fuel cells, flow batteries, PHES, and CAES energy capabilities can be increased simply by extending the capacity of the reservoir. As a consequence, and thanks to this specificity, a fuel cell can be charged passively by injecting the fuel produced somewhere else or by another process in the reservoir(s), and a flow battery by replacing its electrolytes. From an operational point of view, applications where availability and redundancy are important are suited to these types of ESSs.

2.2 - ESSs technologies comparison

PHES and CAES present lower specific power/energy and density values because the rated power and energy that this type of facility can reach is very high and depends on geological parameters. These two ESS technologies are then best suited for large scale energy storage.

Although these figures allow an estimate of weight and volume to be calculated, which gives an idea on raw material utilization and allowing long term analysis of the sustainability of ESS technologies, most of the grid applications use stationary facilities which imply the consideration of weight and volume as secondary criteria.

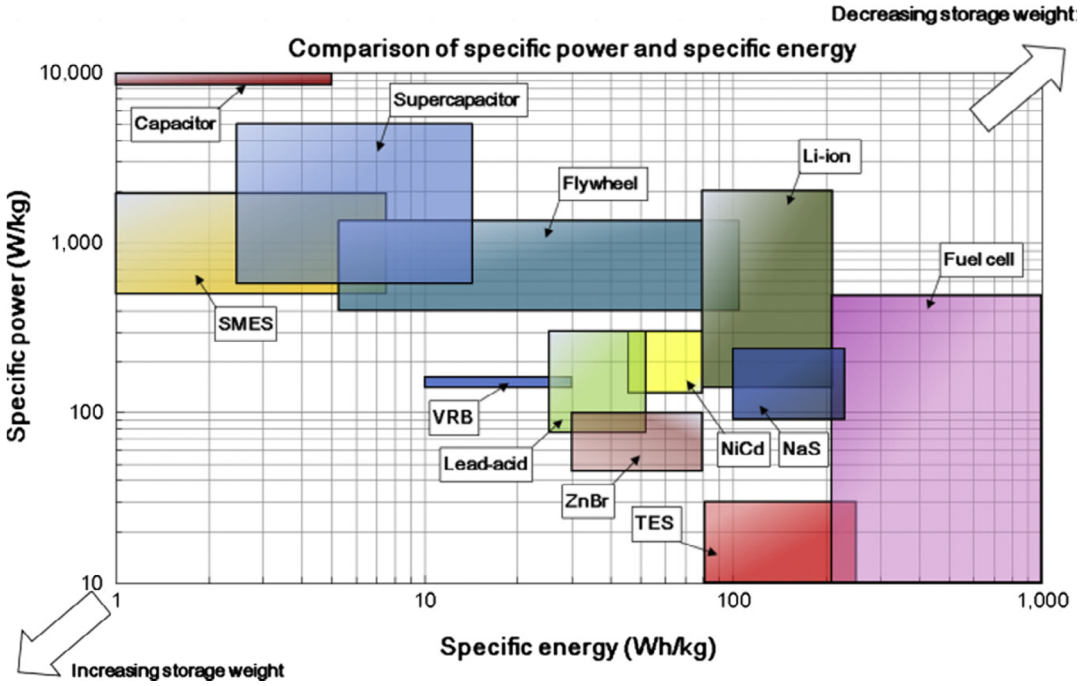

Figure 2.7 ESS specific energy and power comparison [1]

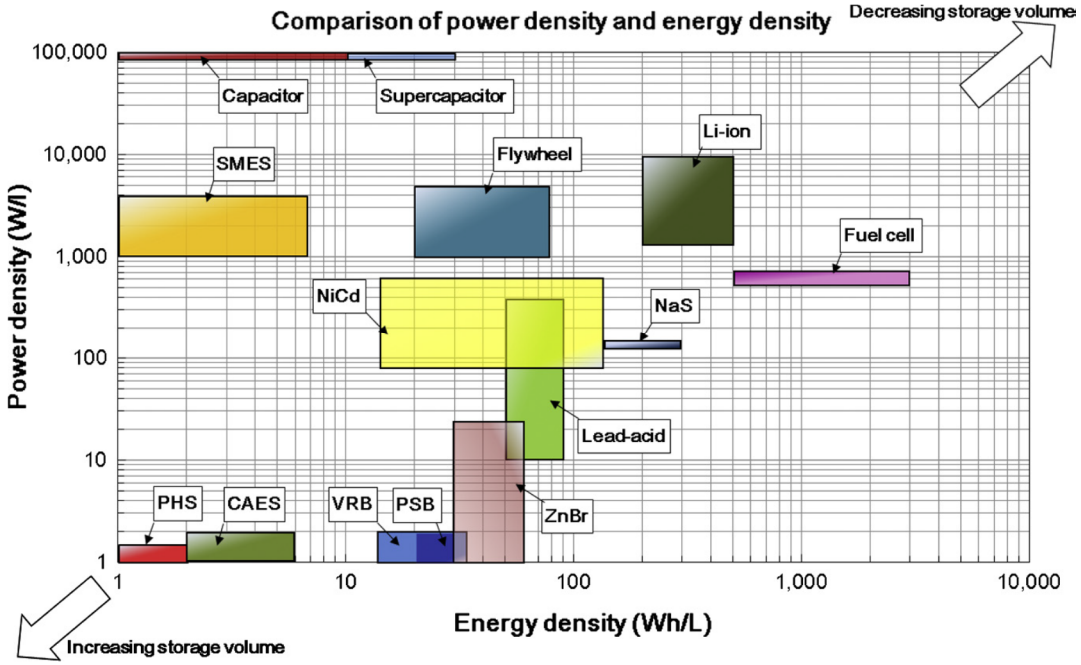

Figure 2.8 ESS energy and power density comparison [1]

ESS Technology	Specific Power [W/kg]	Specific Energy [Wh/kg]	Power Density [W/L]	Energy Density [Wh/L]
Lead-acid	75-250	25-50	10-400	50-90
Li-Ion	150-2,000	75-240	1,500-10,000	200-500
NaS	90-230	100-240	140-180	150-300
Ni-Cd	150-300	45-80	80-600	15-150
VRB	166	10-30	~ 2	16-35
ZnBr	45-100	30-80	~ 25	30-65
PSB	-	15-30	~ 2	20-30
FC	5-800	150-10,000	~ 500	500-3,000
SC	500-10,000	0.05-15	>100,000	10-30
FW	400-1,500	10-100	1,000-5,000	20-80
PHES	-	0.5-1.5	0.5-1.5	0.5-2
CAES	-	30-60	0.5-2	2-6

Table 2.7: ESS technological comparison [1]

2.2.2 Performance comparison

For performance comparison purposes, criteria such as efficiency, response time, self-discharge and cycle life will be taken into account. Table 2.8 shows the performance criteria of a large panel of ESS technologies and Figure 2.9 presents a graph representation of their respective round trip efficiencies.

Similarly to the previous comparison, the Li-Ion technology shows remarkable performances especially in term of round trip efficiency and cycle life. Although its relative high self-discharge compared with flow batteries and fuel cells, which technologically do not allow self-discharge, Li-Ion technology suffers from its dependence on the DOD and the cycle life and thus long term energy storage capabilities for this technology is contrasted. On the contrary, FW and SC suffer from a very high self-discharge which make these technologies suitable for short term storage only. Also, the cycle life of these last being very high allow repetitive usage under heavy conditions.

Fuel cells along with the redox flow batteries use pumps to ensure the right flow of fuel/electrolyte in the stack. These pumps affect the round trip efficiency and slow down the response time as well. A trade-off has been found for this type of ESS to provide either faster response time or higher efficiency. Moreover, some "fuel starvation" phenomena which can impact lifetime may occur in the stack during high amplitude power variation while supplying a dynamic load [3], [23], thus power output gradient of these ESSs should be limited to ensure good cycle life.

Among all redox flow batteries, the VRB has received a lot of attention in recent years and benefit from a technological breakthrough. Compared with PSB and ZnBr, the VRB has higher efficiency and cycle life, yet acceptable in an industrial application. In a weak grid context, thanks to the absence of self-discharge, its flexibility and good round trip efficiency the VRB is a performant solution for long term ESS.

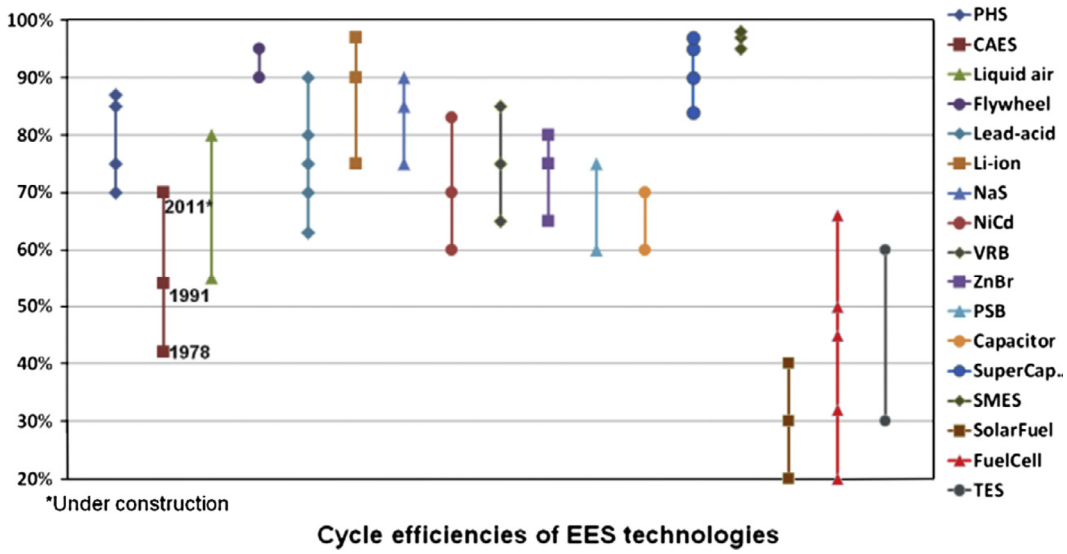

Figure 2.9: Comparison of round trip efficiency [1]

ESS Technology	Round-trip Efficiency [%]	Cycle Life [cycles]	Daily Self-discharge [%]	Response time
Lead-acid	63-97	200-1,800	0.1-0.2	milliseconds
Li-Ion	75-97	1,000-20,000	0.1-5	milliseconds
NaS	75-90	2,000-4,500	~ 0	-
Ni-Cd	60-83	2,000-3,500	0.03-0.6	milliseconds
VRB	65-85	>12,000	~ 0	seconds
ZnBr	65-80	1500-2000	~ 0	seconds
PSB	60-75	-	~ 0	milliseconds
FC	20-66	1000-20,000	~ 0	seconds-minutes
SC	84-97	50,000-100,000	5-40	milliseconds
FW	90-95	>20,000	100	seconds
PHES	70-85	10,000-30,000	~ 0	minutes
CAES	40-70	8000-12,000	~ 0	minutes

Table 2.8: ESS performance comparison [1]

2.2.3 Economical comparison

ESS technologies show a high variability in economic criteria depending on the form in which the energy is stored. Figure 2.10 shows a graph representation of capital cost per power unit versus energy unit from data in Table 2.9. Similarly, with specific power/energy and density, it appears that there is a correlation between capital costs per power/energy as well. This can be partly explained by

the similar price of raw material like lithium, lead or vanadium for example. This graph also allows comparison of power/energy costs effectiveness, and thus the lower the ESS is on the graph the better it for energy management, and the further it is on the left of the graph the better it is for power application.

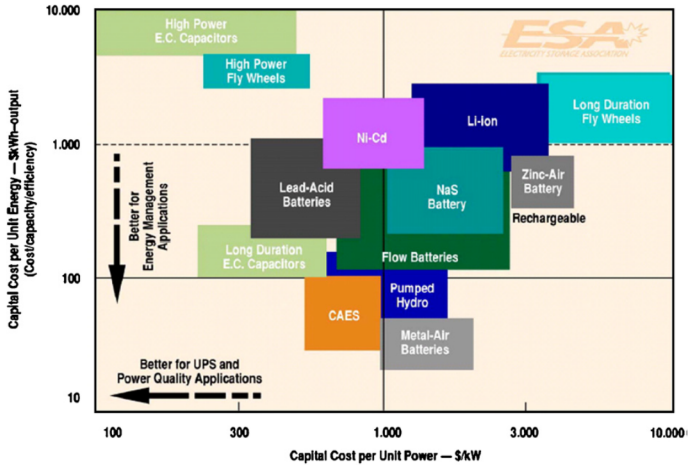

Figure 2.10: Comparison of energy and power capital cost [1]

To compare the economic performance of ESS technologies, the capital cost per cycle is a good indicator and is represented in Figure 2.11. Despite the Operation and Maintenance (O&M) costs not being taken into account in this graph, this indicator remains relevant thanks to the relative similarity of O&M cost for ESSs of the same family. This graph shows that PHES, CAES, FW, and flow batteries are cost-effective solutions compared with static electrolyte electrochemical ESSs like NAS, Li-Ion, Ni-Cd and LA technologies.

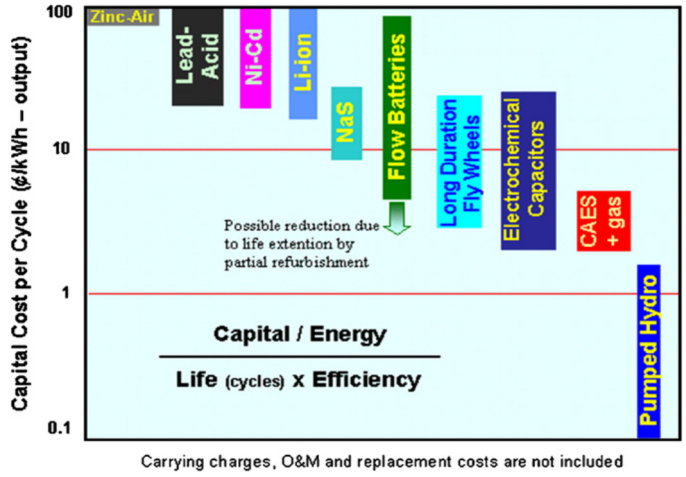

Figure 2.11: Comparison of capital cost per cycle [1]

ESS Technology	Capital Cost Power [$/kW]	Capital Cost Energy [$/kWh]	O&M Cost	Maturity
Lead-acid	200-600	50-400	50 $/kW/year	Mature
Li-Ion	900-4000	600-3800	-	Early commercialized
NaS	350-3000	300-500	80 $/kW/year	Commercialized
Ni-Cd	500-1500	400-2400	20 $/kW/year	Commercialized
VRB	600-1500	150-1000	70 $/kW/year	Early commercialized
ZnBr	200-2500	150-1000	-	Demonstration
PSB	700-2500	150-1000	-	Developing
FC	500-3000	2-15	0.0019-0.015 $/kW	Developing
SC	100-450	300-2000	6 $/kW/year	Commercialized
FW	250-350	1000-14,000	0.004 $/kWh/year	Early commercialized
PHES	2000-4300	5-100	3 $/kW/year	Mature
CAES	400-1000	2-120	19-25 $/kW/year	Commercialized

Table 2.9: ESS economical comparison [1]

2.2.4 ESS market overview

The ESS market is particularly competitive due to large worldwide demand, resulting in price drops in recent years. Figure 2.12 shows the price per kWh from 2014 to now, and the projection until 2024. These trends illustrates how the redox flow and Li-Ion batteries are highly interesting thanks to reasonable costs, and is corroborated by the price drop of these past few years. Moreover, the trends around the aforementioned ESSs technologies show a convergence under 400$ per kWh by 2020, which would unleash global sales and strengthen market confidence over these early commercialized but not yet mature technologies.

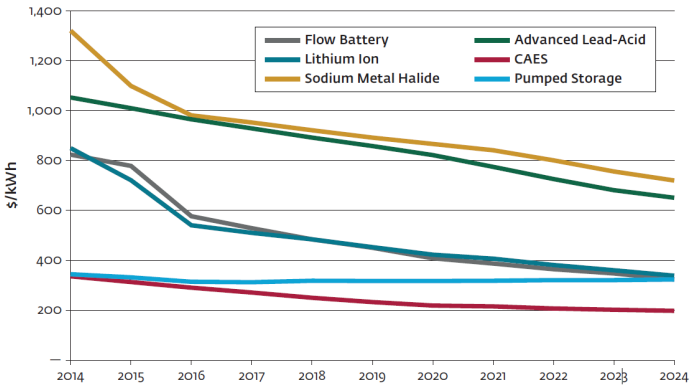

Figure 2.12 Utility scale ESS cost trends by technology, global averages: 2014–2024 [24]

2.3 Usage of ESS with RES in grid applications

The integration of RES in the grid, and especially in weak grids, involves problems described in Chapter 1. There is a consensus on the use of ESS to overcome these issues. Indeed, if most of the energy production has to come from RES in the near future, ESS will be necessary to overcome the variability of the production and ensure its availability to the consumer. But ESS can not only improve RES integration, they can be used as well to provide services to both customers and operators. This section analyses the different possible services and the ESS technology suited for such application.

2.3.1 Capacity Firming

Capacity firming is probably the most needed service in a weak grid with high penetration of RES. In order to ensure stability of weak grids, a generating capacity reserve has to be available in case of a generator or transmission line failure, which lead the T&D system operator to maintain some conventional plants with low power output and thus high marginal costs. If a large part of the production of this weak grid is based on variable and uncontrolled RES, like solar or wind, maintaining the stability margin to an acceptable level would lead to unacceptable costs.

Capacity firming uses ESS along with a variable RES based plant to control the power output and thus makes the hybrid ESS and RES plant dispatchable from the T&D system operator point of view. The plant operator thus commits a production plan (typically day ahead) to the T&D system operator as illustrated in Figure 2.13.

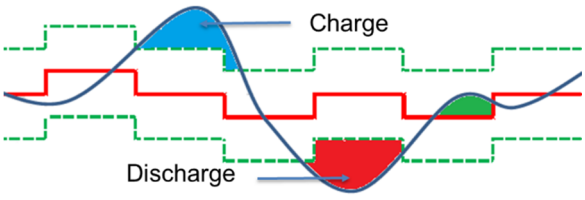

Figure 2.13 Day ahead production plan with tolerance

Capacity firming abilities rely mainly on the accuracy of forecasts, which themselves depend on a large number of factors. A wind farm production forecast will have to take into account the regional wind profile but also the local topology of the plant and so on. In the same way, a solar plant production forecast should take into account the irradiance but also atmospheric conditions such as clouds. This technical limitation of forecast accuracy implies that the fewer forecasts are accurate, the higher the ESS rated energy need is. Still broadly speaking, the ESS used for capacity firming service should have the following characteristics:

- High rated power
- High rated energy
- Moderate to fast response time
- Good cycling abilities
- Large DOD
- Good efficiency

Moreover, it should be noted that the smaller the plant is, the harder it is to get accurate forecasts, mechanically increasing the ESS rated energy to fulfil the production plan. Reversely, increasing the size of a plant, along with mixed energy source (solar plus wind for example), benefits from the aggregation effect.

2.3.2 Frequency Regulation

To ensure stable operation of a power system, the production should meet the demand at any time. When production and consumption are unbalanced the frequency of the network is affected and, depending on its magnitude, could cause a different kind of failures or even a blackout. As afore-mentioned it is then necessary for the T&D system operator to plan a generating capacity reserve in order to face any contingency. Although specific application depends on local grid code, the frequency reserve mechanism can be described as in Figure 2.14. It is composed of a primary reserve that contains the frequency deviation, and a secondary reserve that brings the frequency back to its initial value. The primary reserve is a fast response capacity obtained by increasing or decreasing the output power of the already connected generators through the primary mover governor or the power electronic interface. The secondary reserve, on the contrary, uses fast

startup generators to take over the extra power delivered by the primary reserve generators.

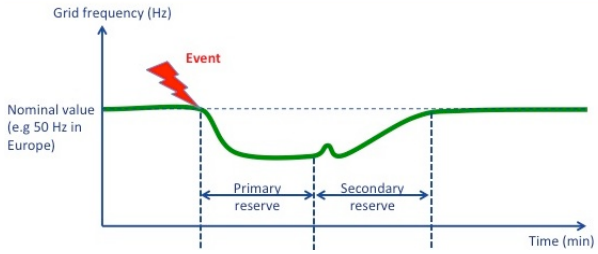

Figure 2.14 Frequency primary and secondary reserve mechanism

RES such as wind and solar plants cannot participate in primary frequency regulation without energy waste. The addition of ESS enable control over the power plant and thus allow to increase or decrease the output active power to fulfill frequency regulation requirements. The practical implementation of the primary frequency regulation uses mainly droop control technique, which is a simple proportional control with a dead band around the base frequency as described in Figure 2.15. The controller gain is generally expressed as a percentage of the static gain of the power system (in MW/Hz) and is fixed by the T&D system operator.

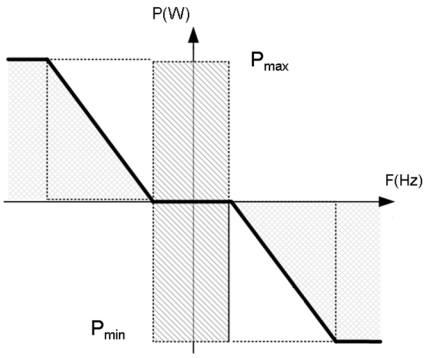

Figure 2.15 Frequency droop control

This service enabled by the installation of ESS along with RES based power plant is particularly important in weak grids. The weak nature of island grids or microgrids makes them very sensitive to active power variations and thus primary frequency regulation increase stability margins. Most of the ongoing worldwide projects on hybrid ESS and RES plants propose primary frequency regulation services. The UK National Grid, for instance, invested 201MW worth of Li-Ion

ESS for eight stationary plants [25]. In France, such applications are currently though field test under the Venteea project [26].

ESS technology selection criteria to realize frequency regulation service are the following:

- High rated power
- Fast response time

2.3.3 Voltage Regulation

The voltage support is as important as frequency to ensure grid stability. Large variations in the voltage would result in damaged equipment or even cascaded generator disconnection of the grid and thus network collapse. In the same way frequency is dependent on the active power, voltage is dependent on the reactive power fluxes. In the past, reactive power requirements were limited to the capabilities of synchronous generators only and variable RES like solar and wind was considered as negligible. Nowadays, the opportunity offered by distributed generators for voltage support has been taken into account, and voltage regulation functionalities are implemented in wind farms or PV plants as required by grid codes [27]. Like the frequency control, voltage regulation is mainly realized through droop control, a proportional controller described by Figure 2.16. The controller gain is generally expressed as a percentage of the static gain of the power system (in MVAR/kV) and is defined by the T&D system operator.

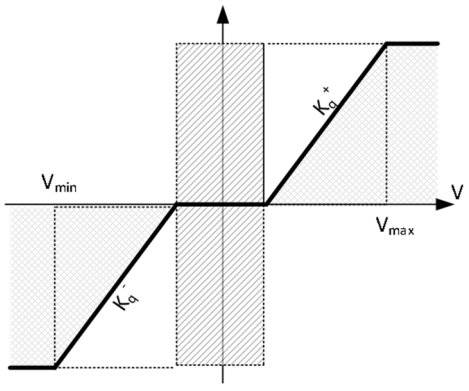

Figure 2.16 Voltage droop control

Power electronic interfaces offer better flexibility for reactive power supply than a conventional synchronous generator that must operate within the appropriate PQ chart. Also, the reliability of grid tie power converter against disturbance involved by default and the ride-through specification imposed by grid codes has been particularly improved these past decades [28]. So the aggregation of voltage control among a RES plant and an ESS offers an increased capacity as well as improved reliability. The remaining problem being the coordination of voltage control participation [28] and the economics associated with the use of ESSs for this purpose [29].

2.3.4 Peak Shaving

Without energy storage, the short duration peak loads are normally supplied by fast-acting peak load generators such as gas turbines. These are expensive assets, generally with lower thermal efficiency than the base load generators, and they may have a load factor of only 2% or less due to the limited time that they are required. Peak shaving refers to the clipping of the demand for immediate generating capacity during the short periods of peak demand and supplying the loads instead of stored energy sources. Peak generating or transmission capacity can thus be reduced by the total potential of all storage plus deferrable loads saving the expense of this capacity. The result is increased load factor, reduced generating costs, possible reduced power charges, and increased return on investment.

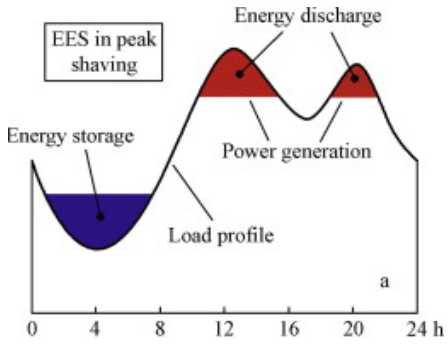

Figure 2.17 Peak shaving principle [8]

Peak shaving can also be implemented by large industrial consumers to reduce their peak load consumption and the associated peak rate energy charges from the grid systems operators. Independent system operators (ISOs) may also offer

incentives to consumers to reduce their peak demand on the network or encourage them to export excess electricity back onto the grid.

2.3.5 Load Leveling

Load Levelling is the rescheduling of the loads on the generating assets to cut the requirements during periods of high demand and to increase the production of energy during off-peak periods for immediate storage and subsequent use during high demand periods.

T&D system operators have used PHES systems for many years to shift generation from peak to off-peak periods.

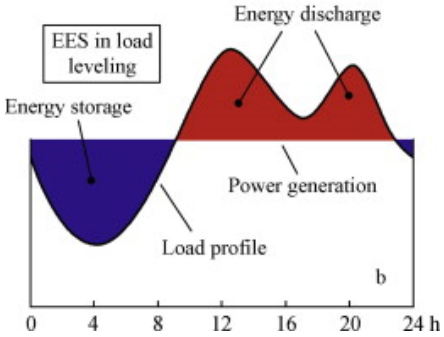

Figure 2.18 Load levelling principle [8]

2.3.6 Power quality

Power quality describes the electrical network's ability to supply a clean and stable power flow. Poor power quality delivery can result in customer equipment malfunctions or even destruction. Several different criteria are used to measure power quality:

- **Voltage Sags:** Line voltage lower than the nominal voltage for short periods due to excessive loading on the system or network faults.
- **Voltage Swells:** Increased line voltage caused by switching off large loads, switching on capacitor banks or by power surges from wind turbines.

- **Harmonics:** Voltages at multiples of the supply frequency caused by high power switching systems and electronic loads such as variable speed drives and power controllers.
- **Flicker:** Random or repetitive variations in the voltage caused by intermittent high consumption industrial processes such as electric arc furnaces and welding equipment.
- **Voltage Unbalances:** Unbalances in load due to monophasic load causes, depending on the line parameters, the unbalanced voltage in the three-phase system.

Maintaining power quality is realised by various specifications of the user end usage or devices. Grid code provides limitation against a financial fine for power factor, harmonic content or even demand peak while big loads like large motors are connected to ensure a good power quality delivery. These measures to enforce power quality have to be managed by the customers themselves. Companies have to install their own power factor correction devices like capacitor banks or Static Var Compensators (SVC) or power filter for harmonic content mitigation.

Still, the power quality has to be managed on the T&D system operator side as well. Reactive power is consumed also by the grid's component itself like a transformer or long capacitive lines. Three phase system are also sensitive to load unbalances as aforementioned. Power electronic-based devices like Static Compensators (STATCOM) and Active Power Filter (APF) allow tackling power quality issues on the grid's side.

In recent years, ESS has been seen as a promising solution to increase STATCOM and APF abilities to manage power quality issues [30]–[32]. In the proposed hybrid systems, power quality issues like voltage sags, swell and flicker caused by fast active and reactive power variation are managed along with basic reactive power regulation for STATCOM and harmonic mitigation for APF. This result in cost effective versatile power quality devices.

2.4 ESS Hybridization

As mentioned in the previous chapter and as detailed in the previous section, no single ESS technology is yet mature enough to provide several of the aforementioned functionalities. Even though the performance of one ESS

technology fulfills the performance needs of both capacity firming and frequency regulation, for example, the sizing would result in a non-optimal solution and probably high capital cost. Following the same example, a HESS offers another degree of freedom by decoupling specific energy, specific power, response time and efficiency. It is then possible to adjust the sizing of both ESSs to closely fit the application needs while decreasing the costs and increasing the lifetime, the efficiency and the reliability, thanks to the redundancy that offers an extra electrical source.

2.4.1 HESS Composition

Selection of ESSs to realize a HESS can be done using simple methods like rule-based heuristic methods, or more complex solutions which would lead to optimal selection and sizing. The selection process can be straightforward depending on the targeted functionalities. To realize a high-performance HESS that can provide all the services described in the previous section, two of the most complementary ESSs should be selected, while preserving efficiency and cycle life.

Considering a HESS composed of a short and long term ESS providing power and energy respectively, the Degree of Hybridization (DOH) expressed in (2.1) has been used for HESS composition and comparison. This ratio allows for quantifying the power/energy split of the HESS among each ESSs, and give a clear insight of the composition.

$$DOH_P = \frac{P_{long\ term}}{P_{short\ term}} \; ; \; DOH_E = \frac{E_{short\ term}}{E_{long\ term}} \tag{2.1}$$

For the sake of simplicity, the DOH will be considered equal for both energy and power from now. As a consequence, the sized energy and power split will be symmetrical. Following this assumption, and considering a 1MW/1MWh HESS it is possible to compare the performance of several HESS compositions as presented in Table 2.10. In this table, the weight and volume are calculated using the specific power and density of the power short term ESS, and the specific energy and density of the long term ESS given in Table 2.7. The round trip efficiency and the capital cost are calculated in the same way using Table 2.8 and Table 2.9 respectively.

This last approximation is acceptable as far as the DOH is low enough, but this ratio cannot be too small either as it will result in a long term ESS with too low rated power, and a short term ESS with too small rated energy. These extreme DOH values could be relevant for some applications, but in order to realise a versatile HESS a DOH of 20% will be considered. This result in a HESS composed of an 800kW/200kWh short term and a 200kW/800kWh long term ESS.

ESSs couples Long term Short term	Rated Power [kW]	Rated Energy [kWh]	Weight [tons]	Volume [m^3]	Capital Cost [k$]	Round Trip Efficiency [%]
Lead-acid	200	800	21,1	12,4	260	82,1
SC bank	800	200	26,7	10,0	450	
VRB	200	800	41,2	131,4	1070	78,1
SC bank	800	200	26,7	10,0	450	
Li-Ion	200	800	6,0	2,3	2250	87,3
Flywheel	800	200	4,7	4,3	1740	
PEMFC	200	800	0,5	0,9	356,8	51,6
Li-Ion	800	200	2,2	0,7	2400	
VRB	200	800	41,2	131,4	1070	77,2
Li-Ion	800	200	2,2	0,7	2400	

Table 2.10: Comparison of different ESS couples global performance

For this work, a Li-Ion battery along with a VRB are selected to realize a high-performance HESS for versatile grid application. Thanks to its remarkable performance, the Li-Ion ESS provides fast response time and power abilities to the HESS while the VRB provides cost-effective and flexible energy capabilities. Moreover, these technologies are both early commercialized and market trends show that reasonable costs and improved reliability could be reached in the near future.

2.4.2 HESS Sizing

Depending on the application, HESS sizing can be very variable. In this work, a versatile HESS has to be constituted which implies that both energy and power energy are needed, with a good round trip efficiency and response time. Therefore rated energy and power of the HESS has to be sized in accordance with the

specification of the application and will depend on various elements like RES plant installed power, forecast accuracy, local grid code specificities or even economic criteria [33]–[36].

In this work, and for the sake of clarity, the rated power has been selected to be 1 MW with a 1MWh rated energy. From the above HESS comparison, the DOH is seen as good criteria for power/energy split sizing. The DOH should be subject to an optimisation but this topic is out of the scope of the present work. An extreme DOH value will result in a short term ESS with very low rated power and a long term ESS with very low rated energy. Therefore using extreme DOH lead to long charging time for the long term ESS and low power availability of the overall HESS. Thus the DOH has been selected at 20% in order to mitigate the aforementioned issue. This leads to a HESS composed of a Li-Ion short term ESS of 800kW rated power and 200kWh rated energy, and a VRB long term ESS of 200kW rated power and 800kWh.

2.5 Chapter References

[1] X. Luo, J. Wang, M. Dooner, and J. Clarke, "Overview of current development in electrical energy storage technologies and the application potential in power system operation," *Appl. Energy*, vol. 137, pp. 511–536, Jan. 2015.

[2] J. Sawin, K. Seyboth, and F. Sverrisson, "Renewables 2017 Global Status Report," 2017.

[3] R. Hemmati and H. Saboori, "Emergence of hybrid energy storage systems in renewable energy and transport applications – A review," *Renew. Sustain. Energy Rev.*, vol. 65, pp. 11–23, Nov. 2016.

[4] O. Gomis-Bellmunt *et al.*, "Battery Energy Storage System (BESS) and Battery Management System (BMS) for Grid-Scale Applications," *Proc. IEEE*, vol. 102, no. 6, pp. 1014–1030, Jun. 2014.

[5] "MYRTE hydrogen energy storage test powers up in Corsica," *Fuel Cells Bull.*, vol. 2014, no. 6, p. 8, Jun. 2014.

[6] A. Hirsch, Y. Parag, and J. Guerrero, "Microgrids: A review of technologies, key drivers, and outstanding issues," *Renew. Sustain. Energy Rev.*, vol. 90, no. March, pp. 402–411, 2018.

[7] F. J. Gimeno-Sales, J. Fu, T. Wang, X. Wang, and J. Sun, "Dynamic Flow Rate Control for Vanadium Redox Flow Batteries," *Energy Procedia*, vol. 105, pp. 4482–4491, May 2017.

[8] H. Chen, T. N. Cong, W. Yang, C. Tan, Y. Li, and Y. Ding, "Progress in electrical energy storage system: A critical review," *Prog. Nat. Sci.*, vol. 19, no. 3, pp. 291–312, Mar. 2009.

[9] "|." [Online]. Available: http://energystorage.org/energy-storage/case-studies/peak-shaving-and-demand-charge-avoidance-prudent-energy-vanadium-redox. [Accessed: 31-Aug-2017].

[10] K. C. Divya and J. Østergaard, "Battery energy storage technology for power systems—An overview," *Electr. Power Syst. Res.*, vol. 79, no. 4, pp.

511–520, Apr. 2009.

[11] S. Shili, A. Hijazi, A. Sari, X. Lin-Shi, and P. Venet, "Balancing Circuit New Control for Supercapacitor Storage System Lifetime Maximization," *IEEE Trans. Power Electron.*, vol. 32, no. 6, pp. 4939–4948, 2017.

[12] Maxwell, "POWER GRID Maxwell ultracapacitors." [Online]. Available: http://www.maxwell.com/images/documents/PowerGrid_CaseStudies_3001287_EN_1.pdf.

[13] G. Delille, B. François, and G. Malarange, "Dynamic frequency control support by energy storage to reduce the impact of wind and solar generation on isolated power system's inertia," *IEEE Trans. Sustain. Energy*, vol. 3, no. 4, pp. 931–939, 2012.

[14] M. Yekini Suberu, M. Wazir Mustafa, and N. Bashir, "Energy storage systems for renewable energy power sector integration and mitigation of intermittency," *Renew. Sustain. Energy Rev.*, vol. 35, pp. 499–514, Jul. 2014.

[15] C. Matos, P. Pereira Da Silva, and J. Carneiro, "Revisiting Compressed Air Energy Storage," in *2nd Meeting on Energy and Environmental Economics*, 2015, no. September, pp. 14–22.

[16] X. Tan, Q. Li, and H. Wang, "Advances and trends of energy storage technology in Microgrid," *Int. J. Electr. Power Energy Syst.*, vol. 44, no. 1, pp. 179–191, Jan. 2013.

[17] J. P. Deane, B. P. Ó Gallachóir, and E. J. McKeogh, "Techno-economic review of existing and new pumped hydro energy storage plant," *Renew. Sustain. Energy Rev.*, vol. 14, no. 4, pp. 1293–1302, 2010.

[18] Vbonz, "Project-CAES Larne, NI." [Online]. Available: http://www.gaelectric.ie/energy-storage-projects/project-caes-larne-ni/. [Accessed: 30-Jun-2017].

[19] J. Kaur, *Energy Storage: A Nontechnical Guide*. PennWell Books, 2006.

[20] P. Tixador, "Superconducting Magnetic Energy Storage : Status and Perspective," *IEEE/CSC ESAS Eur. Supercond. News Forum*, no. 3, pp. 1–

14, 2008.

[21] H. Nakabayashi, S. Nagaya, A. Yogarathinam, A. Mahmud, H. Kawashima, and K. Higashikawa, "System Coordination of 2 GJ Class YBCO SMES for Power System Control," *IEEE Trans. Appl. Supercond.*, vol. 19, no. 3, pp. 2012–2018, Jun. 2009.

[22] L. Chen *et al.*, "Field Test Result of 10MVA/20MJ SMES for Load Fluctuation Compensation," *IEEE Trans. Appl. Supercond.*, vol. 19, no. 3, pp. 1993–1998, Jun. 2009.

[23] P. Thounthong, S. Raël, and B. Davat, "Energy management of fuel cell/battery/supercapacitor hybrid power source for vehicle applications," *J. Power Sources*, vol. 193, no. 1, pp. 376–385, Aug. 2009.

[24] A. Eller and D. Gauntlett, "Energy storage trends and opportunities in emerging markets," in *Energy storage trends and opportunities in emerging markets*, 2017, p. 2009.

[25] P. W. Lehn, "UK's National Grid Goes Big Into Energy Storage With 201MW of Fast-Acting Batteries," Aug-2016. [Online]. Available: https://www.greentechmedia.com/articles/read/uks-national-grid-goes-big-into-energy-storage-with-201mw-of-fast-acting-ba. [Accessed: 09-May-2017].

[26] N. R. Chaudhuri *et al.*, "The Proof Is in the Putting: Large-Scale Demonstrations of Renewables Integration Showcase Real-World Solutions," *IEEE Power Energy Mag.*, vol. 13, no. 1, pp. 75–83, Jan. 2015.

[27] Y. Yang, P. Enjeti, F. Blaabjerg, and H. Wang, "Suggested grid code modifications to ensure wide-scale adoption of photovoltaic energy in distributed power generation systems," in *Conference Record - IAS Annual Meeting (IEEE Industry Applications Society)*, 2013, pp. 1–8.

[28] F. Blaabjerg and K. Ma, "Future on Power Electronics for Wind Turbine Systems," *IEEE J. Emerg. Sel. Top. Power Electron.*, vol. 1, no. 3, pp. 139–152, Sep. 2013.

[29] Y. Riffonneau, S. Bacha, F. Barruel, Y. Baghzouz, and E. Zamaï, "Optimal

reactive supervision of grid connected PV systems with batteries in real conditions," *Int. Rev. Electr. Eng.*, vol. 7, no. 3, pp. 4607–4615, 2012.

[30] M. A. Dybko and S. V. Brovanov, "Active power filter with battery energy storage based on NPC inverters," in *2015 16th International Conference of Young Specialists on Micro/Nanotechnologies and Electron Devices*, 2015, pp. 415–421.

[31] "IEEE Guide for Application of Power Electronics for Power Quality Improvement on Distribution Systems Rated 1 kV Through 38 kV," Apr. 2012.

[32] F. Díaz-González, A. Sumper, O. Gomis-Bellmunt, and R. Villafáfila-Robles, "A review of energy storage technologies for wind power applications," *Renew. Sustain. Energy Rev.*, vol. 16, no. 4, pp. 2154–2171, May 2012.

[33] D. ABBES, A. MARTINEZ, G. CHAMPENOIS, and J. P. GAUBERT, "Multi-Objective Design Optimization of a Hybrid PV-Wind-Battery System," in *Electrimacs*, 2011, no. June, pp. 6–8.

[34] W. Yuan *et al.*, "Design and advanced control strategies of a hybrid energy storage system for the grid integration of wind power generations," *IET Renew. Power Gener.*, vol. 9, no. 2, pp. 89–98, 2015.

[35] H. Babazadeh, W. Gao, and X. Wang, "Controller design for a Hybrid Energy Storage System enabling longer battery life in wind turbine generators," in *2011 North American Power Symposium*, 2011, pp. 1–7.

[36] B. Li, R. Roche, D. Paire, and A. Miraoui, "Sizing of a stand-alone microgrid considering electric power, cooling/heating, hydrogen loads and hydrogen storage degradation," *Appl. Energy*, vol. 205, pp. 1244–1259, Nov. 2017.

Chapter 3

HESS and RES interfacing

Contents

3.1 Power electronic topology and control for RES and HESS integration

Power electronics are used almost everywhere and in any kind of application involving an energy storage device or an energy source. Using a power electronic allows not only the interface of several devices to make them interoperable, but also realisation of precise functionalities and to optimize their global operation. The PV installation with a battery pack represents a good example because its power electronic interface (a DC/DC buck or boost converter) can be controlled to both maximize the energy harvesting of the PV array through a Maximum Power Point Tracking (MPPT) algorithm, and to provide a controllable output voltage/current which can be used to control the power delivered to the battery.

As these interfaces are widely developed and because they enable a large number of configurations, control techniques, and functionalities, a literature review shows that there are three main categories of MG architecture. The main one is the most developed architecture worldwide and realises interconnection of any production or storage device on an AC bus. It has been inherited from the beginning of the first industrial revolution because, among other factors, the AC allows the use of transformers to increase voltage level through magnetic conversion which enables long distance transmission and was the most cost-effective solution at the time. The second structure is based on DC interconnection and has only begun to receive attention thanks to the development of DC-based energy storage and production devices, along with rising power electronics hardware and control device improvements. It enabled DC-based MGs which have proven easier and cheaper to develop compared with the AC power system architecture. High Voltage DC (HVDC) transmission lines also allow a 40% rated power increase for the same cable section used in AC and at the same time require less line than AC ones [1]. Also long HVDC lines suffer far less from capacitive effects compared to AC ones. The last limiting factor for wider use of DC networks was the higher cost for protections and switch gears which is an active research topic [2], [3].

Finally, a third MG architecture that receives increasing attention is a hybrid structure using both AC and DC to take advantage of each technology's benefits

and mitigate their drawbacks. Both pure AC and DC electrical network technologies and practices are well advanced whereas the interface between AC and DC is still subject to improvement. Hybrid MGs, and to an extent any power system, are seen in the literature as an opportunity to increase the efficiency and the reliability of the utility grid, to ease the expansion of the network while decreasing the costs, and last but not least it could enable an increased integration of RES and thus ease the worldwide ambition for greener energy transition.

In this chapter the three different MG architectures, in a context of high RES penetration and using ESS to support the network, are going to be described, along with the power electronic architectures and control methods available. Then the power electronic topologies used to interface a HESS and RES of a DC-based microgrid to an AC microgrid are going to be reviewed. This will show that it is possible to interface two ESSs along with a RES of a DC microgrid to another AC one using only one multilevel inverter. This power converter, a Three Level Neutral Point Clamped (3L-NPC) in which a fourth leg will be added to be able to work on four wire networks will then be described and its capabilities developed.

3.1.1 AC Microgrid Topologies and Control

The AC interconnection is the most developed worldwide because of historical reasons. Three-phase networks are the most employed as they benefit from two configurations depending on the load. Large industries, small scale factories, and even workshops use mainly three-phase loads (heater, motor, induction furnace and so on) while each residential consumer needs less power and thus only one phase is distributed along with a neutral line which is connected to the star coupling middle point of the distribution transformer's Low Voltage (LV) side. On the production side, the high power plants are connected on High Voltage (HV) transmission lines, medium power plants on the Medium Voltage (MV) network and smaller generators can be connected to the LV distribution grid.

With the increasing share of RES based DG integration on both MV and LV distribution networks and the associated issues of a stochastic production, the concept of MG has been proposed as a solution to transform distribution networks in clusters where DG along with ESS can be aggregated and managed in limited

and homogeneous areas. From a T&D operator's point of view, MGs would concentrate aggregate production, forecasts, and load profile data and thus ease dispatching while increasing network efficiency by maximising local consumption.

Depending on the conditions, each cluster could operate either connected or islanded from the main grid which is the most challenging issue of the MG concept. Indeed, AC weak grids like MGs have a decreased stability in islanded mode, and the combination of variable production and the abundance of small generators interfaced with power electronics make it necessary for all generators to participate in the stability effort.

The AC MG structure inherited through historical precedence and practical reasons shows an increased complexity the smaller it gets. Maintain the same stability and power quality in a clustered AC distribution network required to implement new control strategies of increased flexibility and reliability.

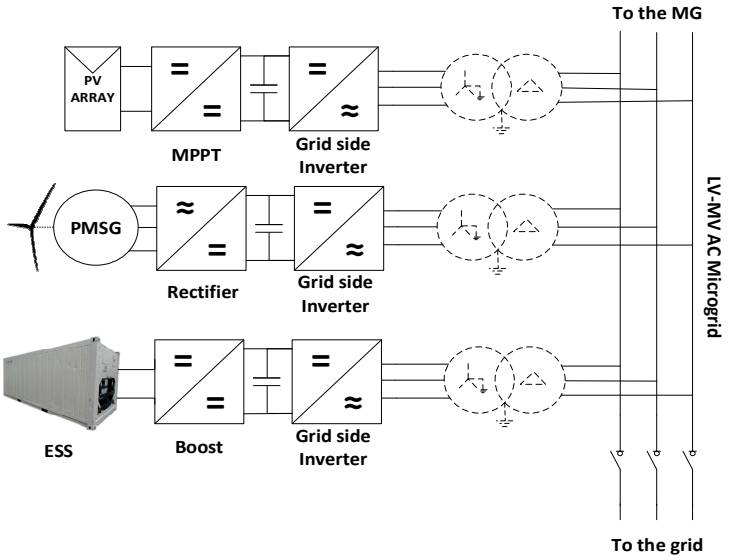

Figure 3.1 Common AC bus microgrid topology

Figure 2.1 shows the basic structure of several types of sources connected on an AC MG. It can be seen that inverters are necessary for DC sources and also for variable frequency AC systems like synchronous generator based wind turbines. The inverter's control and interoperability is, therefore, a major concern because the entire operation of the MG relies on it. Control strategies can be classified into three main categories depending on the role of the inverter in the microgrid, this

role being subject to change in order to adapt to the MGs inherent variable conditions.

- **Grid forming:** the voltage and frequency are fixed by these inverters which are thus considered as a voltage source. This control is used on the highest power generator while the MG operates in islanded mode. It generates a stable reference for other inverters to be able to connect to the MG.
- **Grid feeding:** once the inverters are synchronised and tided to the MG, this mode allows control of the active and reactive power injected on the AC bus and the inverter behaves as a current source. In this mode, the active and reactive power set points result from a control objective independent from the AC side variables. This mode is suited for maximal RES injection or ESS charging.
- **Grid supporting:** this mode relates to the previous one and uses AC side variables for active and reactive power set points calculation to realise frequency and voltage regulation. Depending on the conditions, the inverter can result either in a voltage or current source.

Figure 3.2 shows the basic control structures for these three different modes which define the role of the source in the MG. Grid supporting control strategies are the most important to ensure stable operation of the MG and every connected source should theoretically implement such control mode and participate in the frequency and voltage regulation. A large number of publications have focused on the dispatch of the stability effort using the basic proportional gain know as droop controller [4]–[6]. Some others propose to use the associated information system necessary for MG deployment to implement a cooperative frequency and voltage regulation [7]–[9]. But such controls applied on RES such as wind and solar will result in a non-optimal operation if not backed by an ESS. In the case of a positive frequency deviation due to a positive power balance, the grid-feeding control would reduce the active power set point and therefore RES harvesting would operate under its optimal point. This shows that in AC MGs there is a need for ESS, but also that a developed information system is required to coordinate the sources and use RES as a support for the grid only when necessary.

Finally, it can be seen that most ESS and RES technologies are intrinsically or for energy harvesting optimisation purposes in DC, and then interfaced to the

microgrid through an inverter which, even though the power electronic interfaces present very high efficiencies and advanced control strategies, makes the AC microgrid structure costly and complex the smaller it gets.

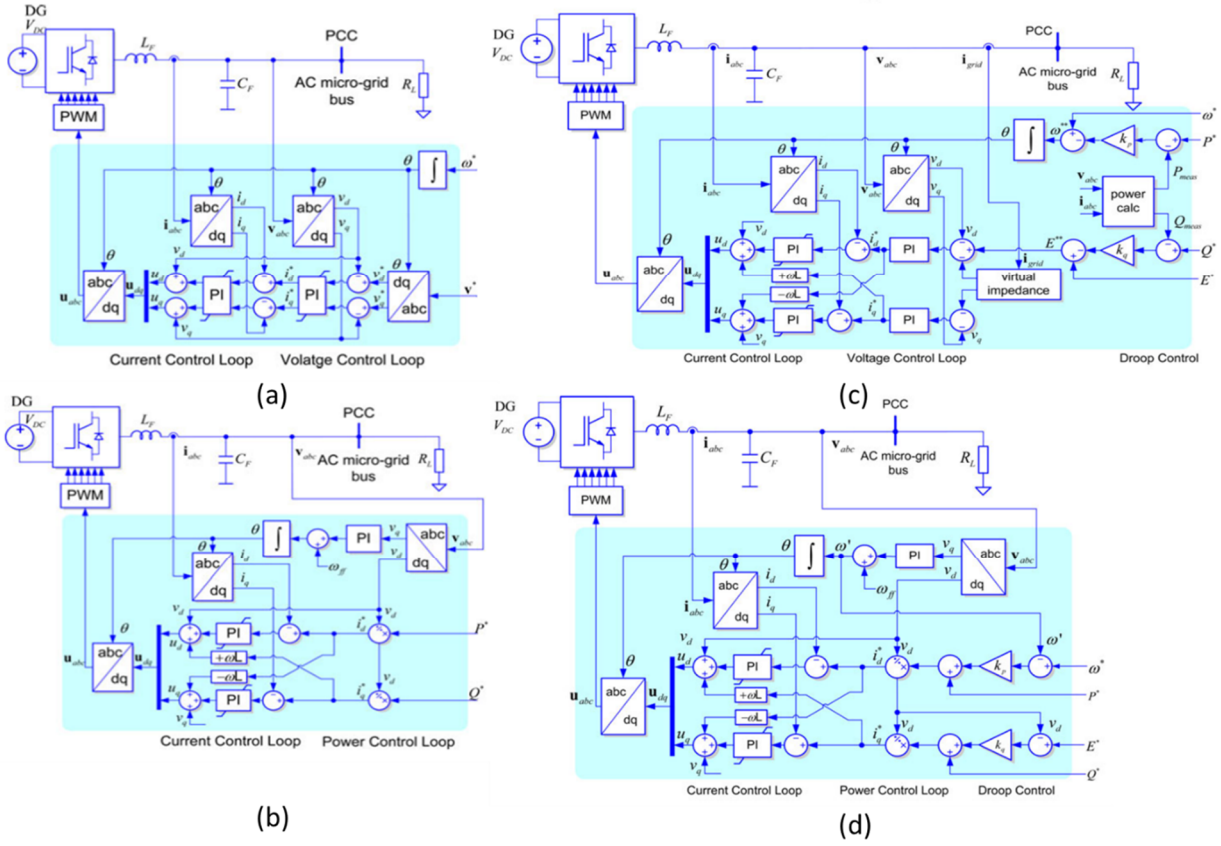

Figure 3.2 Basic control structure of (a) grid forming (b) grid feeding and grid supporting (c) as a current source and (d) as a voltage source [4]

3.1.2 DC Microgrid Topologies and Control

The interconnection of RESs and ESSs on a DC MG present several advantages compared with the AC MG. Among others, the use at nominal power in DC of a cable designed for AC is theoretically higher by a factor $\sqrt{2}$ which is considerable [1]. The direct connection of localised DC-based sources like PVs and ESSs require less power electronic devices which will increase the efficiency. Another important point is the control and coordination straightforwardness compared with the above

described AC MG complexity. Several studies show that DC MG shows better performance and decreased complexity, especially for small scale or remote area MG and micro sources integration [9]–[14].

Figure 3.3 shows the basic DC MG architecture composed of RESs and ESSs connected through an inverter to a grid or another AC MG. The most developed power electronic topologies used to interface a device to a common DC bus are known as buck and boost converter while variable speed synchronous generators use rectifiers. Figure 3.3 shows the schematic of such structures, along with the combined buck-boost topology that realises both voltage step down and step up functionalities.

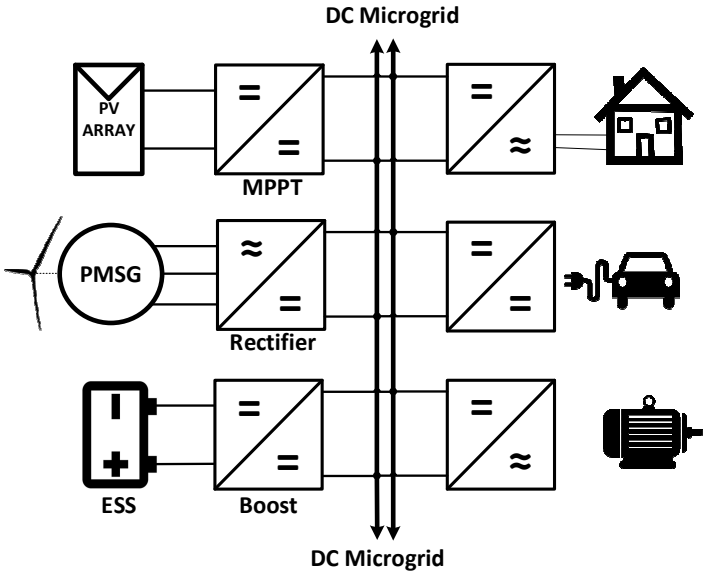

Figure 3.3 Common DC bus MG topology

The stability of the DC MG is directly related to the voltage at the common point of coupling of an equipment. Also, because no synchronisation system is involved, it can be stated that DC MG control is simpler than the AC one. But still the same control categories as the AC MG can be considered:

- **Grid forming:** the voltage is fixed by these converters thus it is controlled as a voltage source.
- **Grid feeding:** the converters are connected to a bus of given voltage which can be variable and is controlled as a current source to a given power set point.

- **Grid supporting:** this mode is derived from the grid feeding one and implements DC bus control abilities.

Grid supporting and to an extent, any control strategies in DC MG are simpler than AC ones because only the voltage at the coupling point needs regulation. The main grid supporting control strategies developed in the literature use simple droop controller, exactly like the AC MG grid supporting ones, but the inherited DC simplicity enables improved coordinated and optimal controls [9], [10], [15], [16]. Moreover, unlike the AC MG case, RES like solar or wind participation in the MG support would not affect the energy harvesting maximisation. Indeed, thanks to the ability of DC/DC converter to behave as a voltage source with low output impedance, and considering the line resistance low enough to be negligible, any kind of device plugged on the DC MG can implement a grid supporting control and effectively regulate the MG voltage without power limitation [17].

Pure DC MG show a decreased complexity for large integration of small RES and an increased efficiency because most of ESS and RES are DC-based. But even though a large amount of devices nowadays are DC-based and could be switched in a pure DC MG model, AC is used worldwide and a transition to pure DC MG is unrealistic. Still the study of DC MG represents an opportunity for certain regions and to fill the theoretical and experimental lacks in the literature.

3.1.3 Hybrid AC/DC Microgrids

Both AC and DC MGs show advantages and drawbacks, therefore, several research works suggest that both AC and DC can be used together to realise a hybrid MG [15], [18]–[22]. The RES based generation and ESS would benefit from an easier and more efficient integration in the DC subgrid of the hybrid MGs, while the majority of loads and the connection to the main grid will remain on the AC subgrid. This configuration takes advantage of the existing infrastructure and any consolidation or extension of the network would implement the DC subgrid which is a realistic transition scheme.

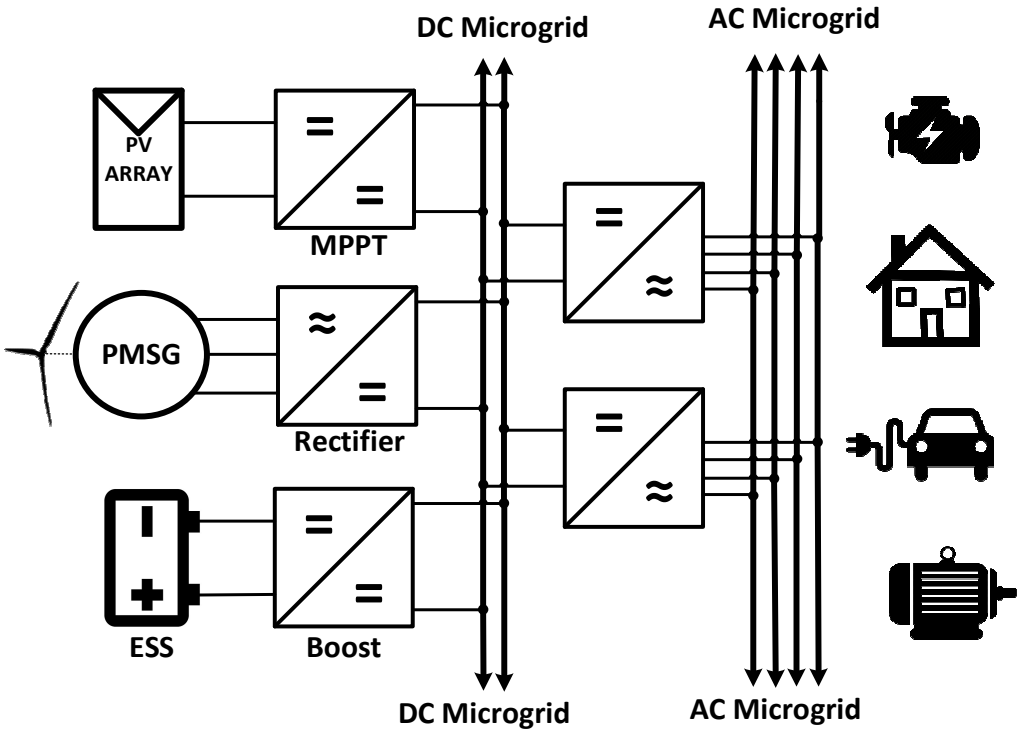

Figure 3.4 Hybrid AC-DC MG structure

Figure 3.4 shows the structure of a hybrid AC-DC MG composed of two subgrids tied together through bidirectional inverters. The interface between AC and DC becomes the main focus of interest in this kind of structure, and enables multiple interconnections with other DC or AC MG or the main grid through redundant power electronic interfaces that improve reliability. As a result, the degrees of freedom of such structures is increased, and several research report an improved ability to support the MG while at the same time increasing efficiency [23].

3.2 NPC topology for HESS and RES interface to MGs

The previous section showed that ESSs and RES based DG integration in a hybrid MG composed of a AC and DC subgrids could potentially increase the interest of the MG concept itself and enable its development, and at the same time increase the efficiency and reliability. With this perspective, the power electronic structures to interface several ESSs and RES to an AC MG are investigated.

3.2.1 HESS power electronic structure review

To interface several ESS, several possibilities have been investigated in the literature. Figure 3.5 shows the main power electronic structures available, namely the floating, parallel and NPC.

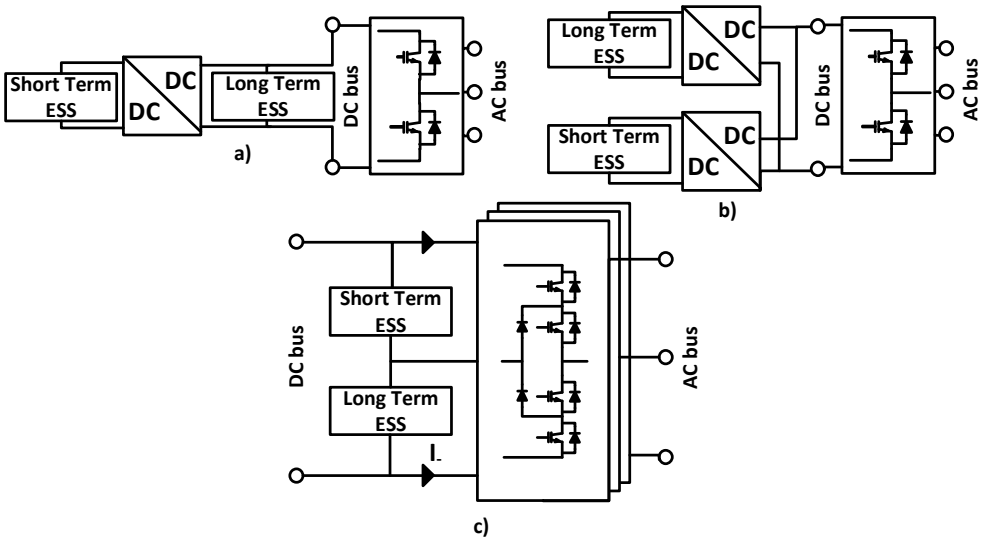

Figure 3.5 Hybrid AC/DC MG topologies a) floating b) parallel c) NPC

The floating topology has been investigated in [24]–[27]. In these only one power converter is used to control the power flow of the short term storage (a SC bank), while the long term storage (lead-acid batteries) is directly connected to the DC bus. The topology allows to reduce the power variation and thus increase its lifecycle. The main drawback is that the DC bus voltage is dependents on the battery SOC, which can be a problem for fixed voltage applications.

The parallel topology has been extensively investigated in [28]–[35]. This is the most common approach to realize a HESS for MG applications given its ability to manage the power flow and SOC of each ESS independently. Unlike the floating topology, the DOD rate of the ESS is not limited as the DC bus voltage does not depend on the SOC of one of the ESS, and consequently, the ESSs can be exploited to their limits whatever the technology being used.

Finally, the 3LNPC topology has been investigated for MG applications in [36]–[38]. The simulation and experimental results show that this topology is able to

smooth the power variation of a RES directly connected to the DC bus, and split the power between the long term storage (vanadium redox flow battery) and the short term storage (a SC bank). This topology has also proven its ability to face disconnection from the main grid and provide a fast variation of power from the SC bank with short settling time thanks to an adapted control. As the 3LNPC topology involves only one AC/DC power converter, the power losses are proven to be reduced by 40% and 50% compared to the floating and parallel topologies respectively [39].

3.2.2 NPC Benefits

The multilevel NPC topology presents several levels of output voltage. Thus the voltage across each switch is reduced compared with a two-level inverter. As a consequence, the maximum DC bus voltage can be increased and so the power delivered by the inverter too which results in increased specific power for a multilevel NPC inverter compared with a two-level one.

In the meantime, inverter's losses occur within the static switches through switching and conduction losses. The switching losses depend strongly on the voltage across the switches. Compared with a two-level inverter and for the same DC bus voltage and switching frequency, a multilevel inverter will show a reduced voltage across the switches (half the DC bus voltage for a three level) and thus reduced losses compared with a two-level inverter.

Another important benefit of multilevel inverters is the decreased harmonic content of the AC side signal. The reduced voltage between two levels of voltage implies that the output current's variation of the inductive filter is reduced too, and thus the Total Harmonic Distortion (THD). Finally, and despite the number of level increase complexity, it is accepted that the more level there is, the lower THD can be [40]. Several levels of voltage increase the degrees of freedom in control and modulation strategy and recent advances have made multilevel inverters the best suited for a wide range of application where power quality is a major concern [41].

Finally, even though the NPC topology used as a unique power electronic interface involves drawbacks detailed below, it presents several economic and operational advantages, especially compared with the parallel structure, thanks to the increased efficiency and the use of less passive components [42].

3.2.3 NPC Drawbacks

In the context of ESS hybridization, the flexibility encompasses the ability of a power electronic interface and controller to use each ESS technology to its maximal potential, while preserving a correct lifetime. More specifically, the parameters to evaluate the flexibility of a HESS interface are the following:

- SOC control over each ESS
- Response time of each ESS
- Power flow distribution between the ESSs

As aforementioned, the main drawback of NPC structure used as HESS interface is reduced flexibility compared with other solutions using intermediary DC/DC power converter, and particularly with the parallel topology which offers the best flexibility [39], [43].

The lack of flexibility of the NPC topology comes from the structure of the ESSs connection itself, and of the resulting lack of control over both ESSs at the same time. As described more precisely later on, the direct series connection of both ESSs results in only one degree of freedom, and in some way the NPC topology is equivalent to the floating one in term of flexibility.

Moreover, the power division between ESSs is strongly dependant on the ESSs rated voltage unbalances, which is the main structural limit of this scheme [44] and is detailed in the next section. Thus the larger the ESSs voltage unbalance is, the poorer the flexibility.

Another minor drawback has been observed in the capacitor middle point voltage oscillation of the 3L-NPC [45] which involves current ripples on the DC bus. The current oscillation amplitude depends mainly on the modulation technique and the capacitance of the DC link filter [46]. This issue is related to the largely commented "capacitor voltage balancing" of the NPC topology and can be simply tackled by

oversizing the DC link filter or using active methods developed later on. This issue still receives attention today [47].

Finally using only one power converter to realize both AC and DC side control makes the overall control more complex, especially because of the coupling between the two sides and the impact of voltage levels unbalances, which along with the modulation index will play a role in the limitation of the topology, and will be discussed in Section 3.4.

3.2.4 HESS and RES interface specifications

As described in Chapter 2, ESS hybridization has been described as an opportunity to increase performance and efficiency while reducing capital and operational costs. The profitability of HESS mass deployment for grid application and RES integration also require diversification of services provided to T&D operators. The HESS's power converters used to interface the different energy sources must then fulfill several specifications to be able to ensure the aforementioned services, and are listed below:

- Fast response time
- Disturbance and parametric robustness
- DC side HESS control
- AC side grid forming, feeding or supporting abilities

3.3 Multipurpose NPC interface modelling

The NPC topology has been extensively studied in the literature. A particular issue that has received a lot of attention is the so-called "capacitor voltage unbalance" problem. Thanks to the abundant studies of this problem, there is a clear understanding on how to deal with unbalanced voltage levels, and thus on how to use the NPC topology to realize a HESS and RES interface.

Figure 3.6 shows the schematic representation of the 4-Leg 3L-NPC inverter used as a HESS interface for RES and HESS integration to a MG. This topology requires the RES to be a current source and in particular, could be adapted if placed either after a Maximum Power Point Tracking (MPPT) converter for a

solar plant, or instead of the grid-side converter of a back to back set up for wind turbines. The fourth leg gives another degree of freedom and allows to manage islanded unbalanced networks as well as improve the power quality in grid-connected mode.

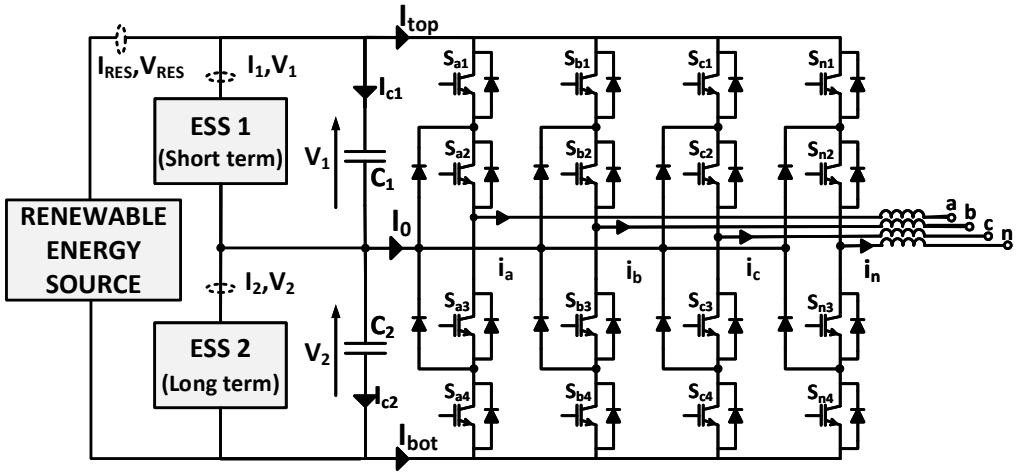

Figure 3.6 4 Leg 3L-NPC topology for HESS and RES interface

3.3.1 Switching model

The 4 Leg 3L-NPC inverter has four switches per phase. Only two are independent while the others are complementary ($S_{i1} = \overline{S_{i3}}$ and $S_{i2} = \overline{S_{i4}}$, where *i=a, b, c, n*) to avoid combinations that lead to short circuit. Another state must be avoided because of the inductive nature of the AC side filter where S_{i2} and S_{i3} are opened which result in a blocked clamping diode and thus a floating potential of the phase. This situation could result in switches and clamping diode destruction due to large overvoltage. Thus only three combinations are available per arm which result in three level of output voltage as described in Table 3.11.

Output level for leg x	State of the switches for leg x				Corresponding voltage
	S_{x1}	S_{x2}	S_{x3}	S_{x4}	
n	0	0	1	1	0
o	0	1	1	0	Uc2
p	1	1	0	0	Uc1+Uc2

Table 3.11: Possible switching states for a single leg

The 4 leg 3L-NPC has then $3^4 = 81$ different switching states enumerated in Table 3.12 and whose 3D space vector diagram is represented in $\alpha\beta 0$ frame in Figure 3.7 considering the DC link capacitor voltages equal. It can be seen that some vectors can be obtained by more than one switching state, those are called redundant vectors. Despite that, from the AC point of view, there is equivalence between two redundant vectors, it causes on the DC side an inverse middle point current i_0 which can affect the capacitors voltage equality if the average value of this current is not null. Therefore the redundant vectors use and control is widely developed in the literature for capacitors voltage balancing issue [48]–[51].

Using two voltage sources in parallel with the DC link capacitors as depicted in Figure 3.6, the same principle applied to the redundant vector result in the ability to draw more current on one source or the other if the middle point current i_0 average value is not null. The power split between the two voltage sources can then be controlled using one or the other of the redundant vectors.

Vector	State	Vector	State	Vector	State
1	nnnn	28	onnn	55	pnnn
2	nnno	29	onno	56	pnno
3	nnnp	30	onnp	57	pnnp
4	nnon	31	onon	58	pnon
5	nnoo	32	onoo	59	pnoo
6	nnop	33	onop	60	pnop
7	nnpn	34	onpn	61	pnpn
8	nnpo	35	onpo	62	pnpo
9	nnpp	36	onpp	63	pnpp
10	nonn	37	oonn	64	ponn
11	nono	38	oono	65	pono
12	nonp	39	oonp	66	ponp
13	noon	40	ooon	67	poon
14	nooo	41	oooo	68	pooo
15	noop	42	ooop	69	poop
16	nopn	43	oopn	70	popn
17	nopo	44	oopo	71	popo
18	nopp	45	oopp	72	popp
19	npnn	46	opnn	73	ppnn
20	npno	47	opno	74	ppno
21	npnp	48	opnp	75	ppnp
22	npon	49	opon	76	ppon
23	npoo	50	opoo	77	ppoo
24	npop	51	opop	78	ppop
25	nppn	52	oppn	79	pppn
26	nppo	53	oppo	80	pppo
27	nppp	54	oppp	81	pppp

Table 3.12: 4 Leg 3L-NPC switching

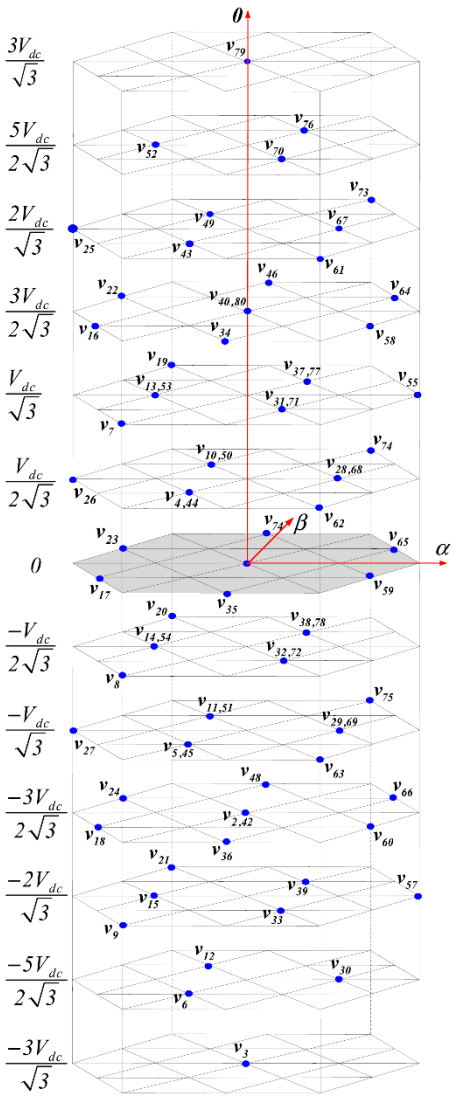

Figure 3.7 4 Leg 3L-NPC space vector [48]

Although, using ESSs as voltage sources implies that the voltage across the capacitors cannot be equal, and even vary depending on the SOC. Thus the previous switching states change and the redundant vectors do not provide the same output space vector any more. Figure 3.8 shows a projection of the three dimension space vector diagram on αβ for U_{c1}=U_{c2}. If the DC link voltages are unbalanced this projection becomes the one in Figure 3.9. Most of the proposed solutions for capacitor balancing assumes balanced DC voltages models, therefore

these solutions along with this hypothesis cannot be retained for this present work. This issue and its solution are further discussed in section 3.3.6.

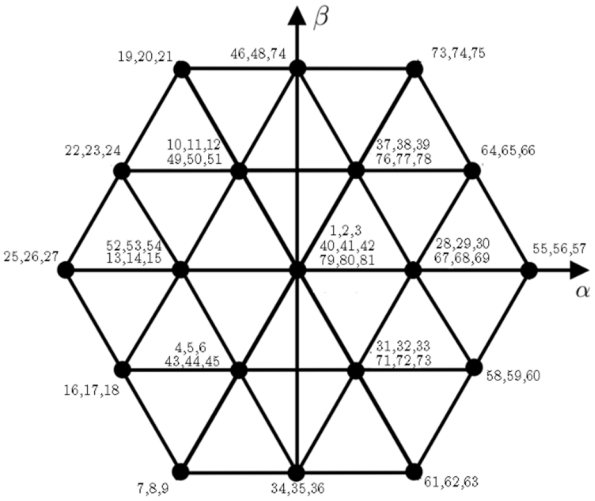

Figure 3.8 space vector projection on αβ for $U_{c1}=U_{c2}$

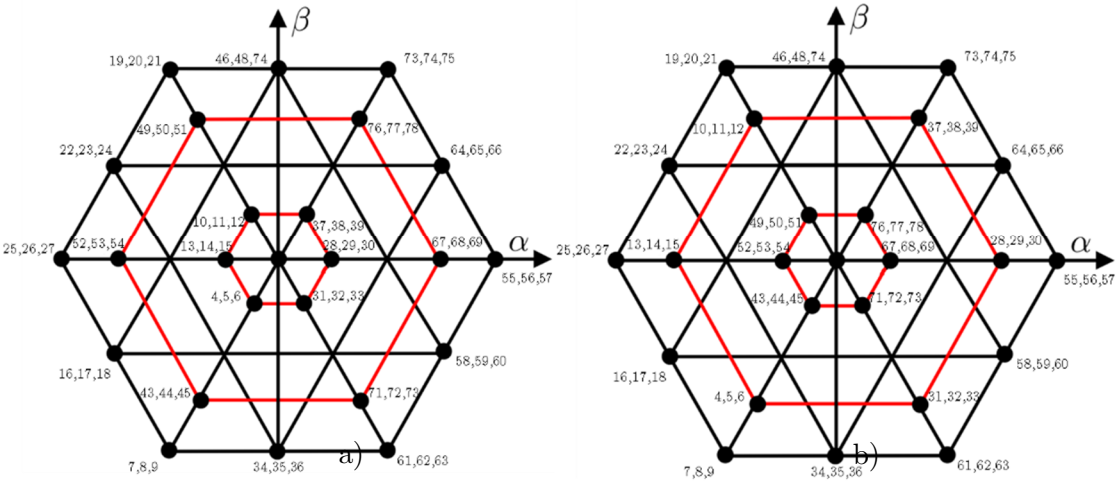

Figure 3.9 space vector projection on αβ for a) $U_{c1}>U_{c2}$ b) $U_{c1}<U_{c2}$

3.3.2 Modulation strategy

Modulation strategies can be classified into two major groups, the Carrier Based Pulse Width Modulation (CB-PWM) and the Space Vector Pulse Width Modulation (SV-PWM). The flourishing emergence of new modulation techniques

for multilevel inverters has also shown the use of mixed strategies where both CB-PWM and SV-PWM coexist [42].

The SV-PWM methods tend to use a mathematical combination of the switching states to match the reference output voltage vector. It often involves an algorithm with different degrees of complexity to find the appropriate switching state, depending on the control targets. The issue with SV-PWM applied to multilevel inverters, which is exacerbated for four legs inverters, lies in the high number of switching states. This causes the SV-PWM to remain too complex and computing consuming. Even though fast SMV technique, generalized to N level has been proposed and shown good results [50], [52], it is still an active major topic to realize efficient and robust multi-criteria control targets using pure SV-PWM methods and to improve the implementation process in an industrial environment.

On the other hand, CB-PWM is the most employed modulation strategy thanks to its easier implementation on industrial controllers. Carrier-based methods use a modulation signal generated by a controller and compared with a higher frequency carrier signal to generate the switches order. Classical two-level inverters generally use a single fixed frequency triangle signal as a carrier. In the case of multilevel inverters and due to the increased number of voltage levels, several methods have been developed in the literature. A common approach is to use N-1 carriers with N the number of levels, then the disposition is subject to various kinds of arrangements [53] which have a different impact on harmonics [54], switching losses [53] or capacitor voltage balancing [55] among others. Another equivalent method to the level shifted carriers one is to use a single carrier and apply a transform on the modulation signal instead, which leads to easier hardware implementation.

Finally, comparisons between the two modulation strategies have been investigated in [55]–[57] and have shown that there is an equivalence between SV-PWM and CB-PWM, the only difference lies in the increased degree of freedom offered by the SV-PWM. Therefore, and to balance out the drawbacks and advantage of these two modulation techniques, the use of a hybrid modulation scheme has been investigated in [58]–[60]. This shows that it is possible to take advantage of the simplicity of the CB-PWM and use SV-PWM principles to get another degree of freedom to realize a specific target.

3.3.3 Hybrid modulation strategy

In this work, a hybrid modulation strategy is developed to overcome the difficulty of the SV-PWM theory to manage a large number of switching states (i.e. 87 for the 4 leg 3L-NPC) and benefit from the large resources available for CB-PWM techniques applied to the NPC.

Several CB-PWM methods have proven their ability to overcome efficiently issues like DC link capacitor voltage unbalances and power division of the 3 leg 3L-NPC using level shifting and zero sequence injection. On the other hand, SV-PWM strategies are the most used for 4 leg 3L-NPC and fast algorithms have been developed for neutral 4^{th} leg management.

To take advantage of both modulation techniques, the modelling of the converter is split into two part in which simplification is carried out. Using an appropriate hypothesis, it is possible to consider the 4 leg 3L-NPC as the combination of a 3 leg 3L-NPC and a 4 leg two-level inverter. Indeed, considering a specific design of CB-PWM for the 3 leg 3L-NPC can result in an equivalent model as a two-level one. Then it is possible to extend this model to a four leg one to apply the SV-PWM modulation technique.

3.3.4 4^{th} leg signal generation

Due to the increasing number of low voltage power electronic devices connected to the grid, four leg inverter and rectifier have received particular attention for power quality applications. Several works have developed methods for 4^{th} leg generation with both CB-PWM and SV-PWM modulation techniques in the literature. But to the knowledge of the author, no algorithm has yet been developed for 4 Leg 3L-NPC with unbalanced DC link. Therefore, and as aforementioned, the inverter is considered as a classical 4 leg two-level inverter for the 4^{th} leg modulation signal generation. The validity of this hypothesis lies in the ability of the additional CB-PWM modulation to manage the NPC DC link voltage unbalances and is developed in Section 3.3.6.

The algorithm chosen for this work is based on a SV-PWM technique for vector selection and calculation in ABC coordinates developed in [61]. This algorithm

called 3D-SVM has been chosen for its computational performance due to its relative simplicity and because no lookup tables or transforms are involved. It has been successfully implemented in both simulations and experiments in [62] and shows good transient performance. Figure 3.10 shows the output of the 3D-SVM algorithm developed in [61] for different modulation index values.

The only drawback of the 3D-SVM lies in the discontinuities of the output modulation signal at every voltage vector switch which occurs every 60°. These transients involve extra harmonics on AC waveforms and thus increased output THD. This phenomenon is logically exacerbated for high or low modulation index (m>0.8 or m<0.4). It should be noted that every discontinuous PWM strategy result in an increased THD.

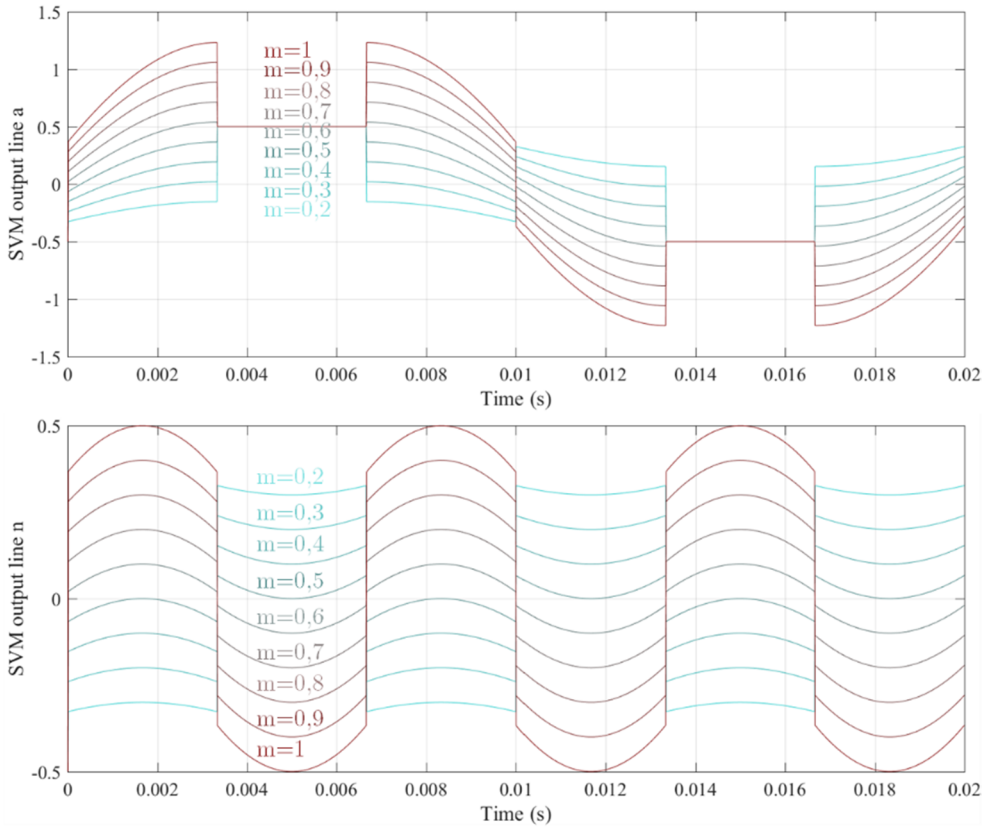

Figure 3.10 3D-SVM output for different modulation index a) line a b) line n

The 3D-SVM processing steps will not be developed further as they are out of the scope of this present work. Thus the 3D-SVM will be considered as a transform applied to the three input modulation signals d_{abc} which give the four output

modulation signals denoted d_{abcn}^{SVM}. As can be seen in Figure 3.10 the amplitude of the 3D-SVM output do not vary linearly. The maximum values of d_{abcn}^{SVM}, which will play an important role in the structural limits definition, can be expressed as in (3.1). This expression is also valid for unbalanced modulation signals d_{abc} as can be seen in Figure 3.11.

$$\begin{aligned} \left|min(d_{abc}^{SVM})\right| &= max(d_{abc}^{SVM}) = 0.5 && for\ m \leq \frac{\sqrt{3}}{3} \\ \left|min(d_{abc}^{SVM})\right| &= max(d_{abc}^{SVM}) = \sqrt{3}\,.m - 0.5 && for\ m > \frac{\sqrt{3}}{3} \end{aligned} \tag{3.1}$$

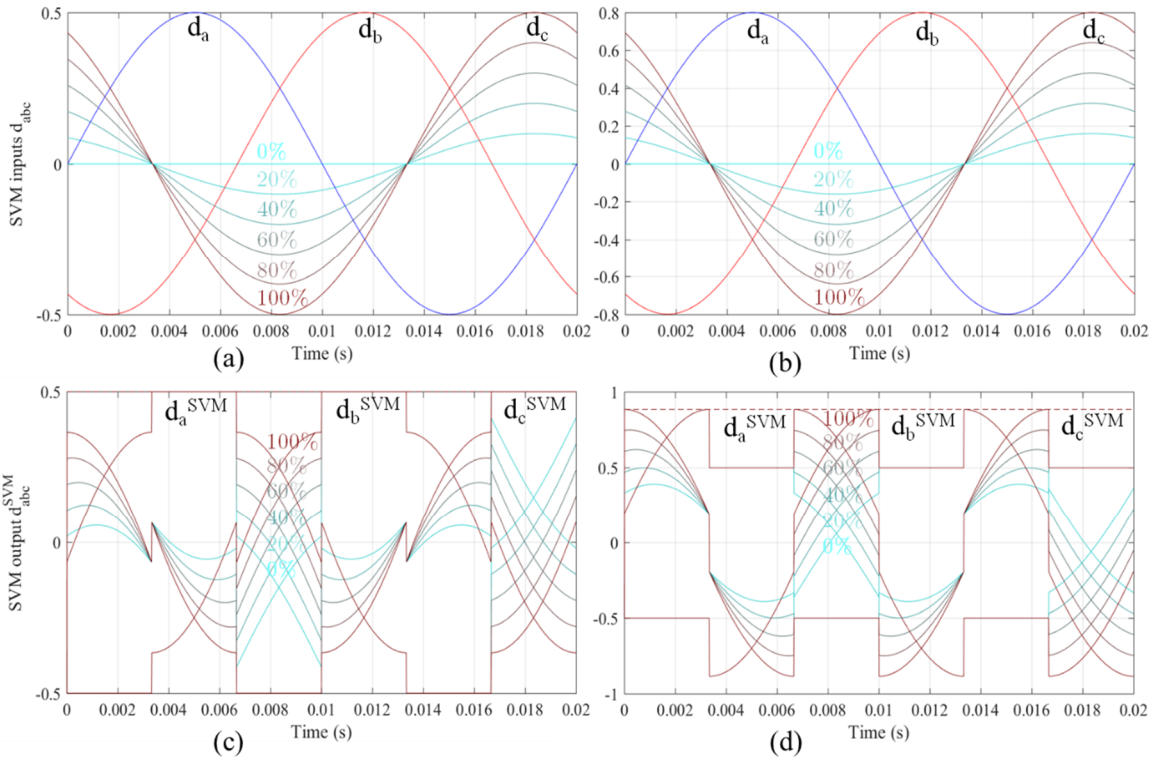

Figure 3.11 3D-SVM output d_{abc}^{SVM} for d_c unbalances (a)(c) m=0.8 (b)(d) m=0.5

3.3.5 Power division strategy

The power division of a HESS using a 3L-NCP inverter is realized through the appropriate redundant vectors selection. This selection using SV-PWM methods has been investigated in [38] and shows good results. CB-PWM although shown

the ability to process to the selection of redundant vectors using a simple zero sequence injection in the modulation signals [55]. This principle has been successfully implemented for HESS power control and a comparison between the two techniques has been carried out in [63]. Even though SV-PWM theoretically allow higher power division between the two ESSs, the author states that the proper vector selection would be much more complicated to design and implement from a practical point of view.

The main advantage of the CB-PWM technique over SV-PWM for power division lies also in the easier mathematical integration of the power division process in the global model of the system, especially if other control objectives are realized. Moreover, due to the aforementioned lack of flexibility of the NPC topology, the limits of the system have to be investigated and the SV-PWM modulation technique does not enable a clear analysis of these limits. Thus the zero sequence technique is chosen in this work to realize power flow division among the HESS.

For power division control, a zero sequence signal Z_s will be then added to the modulation signal output of the 3D-SVM algorithm to obtain $d_{abcn}^{Z_s}$ as in (3.2). The control of this variable will be described in the next chapter.

$$d_{abcn}^{Z_s} = Z_s + d_{abcn}^{SVM} \tag{3.2}$$

3.3.6 ESSs voltage unbalance

The DC voltage unbalances and variations caused by the use of two ESSs as a voltage source causes uneven voltage levels on the AC side and thus non-zero average output voltages. This issue has been addressed mostly using CB-PWM level shifting techniques and developed in [64]. To compensate the level distortion in multicarrier configuration, the carrier's amplitudes are modified using the factors in (3.3) which result in zero average output signals. This solution efficiency compared to its simplicity makes it the most relevant from a practical point of view.

$$\begin{cases} A_1 = \dfrac{2V_1}{V_1 + V_2} \\ A_2 = \dfrac{2V_2}{V_1 + V_2} \end{cases} \tag{3.3}$$

Following the same principle, it has been shown that this method can be transposed by shifting the modulation signal itself instead of the carriers [63]. The transform in (3.4) applied to the modulation signals result in the same output voltage correction. Finally, it is possible to use only one carrier for an easier implementation by applying the transform in (3.5) which splits the modulation signal d_k^1 and d_k^2 in their positives and negatives, and only the positive part of d_k^1 and the negative part of d_k^2 are kept, the last one being shifted as well to have d_k^{top} and d_k^{bot} in the range [0,1] and thus only one carrier required.

$$\begin{cases} d_k^1 = \dfrac{A_1 - 1 + d_k}{A_1} \\ d_k^2 = \dfrac{A_1 - 1 + d_k}{A_2} \end{cases} \qquad k = a, b, c, n \tag{3.4}$$

$$\begin{cases} d_k^{top} = d_k^{top} \dfrac{1 + sign(d_k^1)}{2} \\ d_k^{bot} = d_k^{bot} \dfrac{1 - sign(d_k^2)}{2} + 1 \end{cases} \qquad k = a, b, c, n \tag{3.5}$$

3.3.7 Complete model

The complete block diagram of the operation realized on the modulating signals are described in Figure 3.12. Using equations (3.2), (3.3), (3.4) and (3.5), the relationship between the 3D-SVM output signals and the switches modulation signals can be obtained (3.6). Considering that the carrier frequency is much higher than the fundamental frequency, the average model is used to express the relationship between the DC currents and the modulation signals and is given in (3.7).

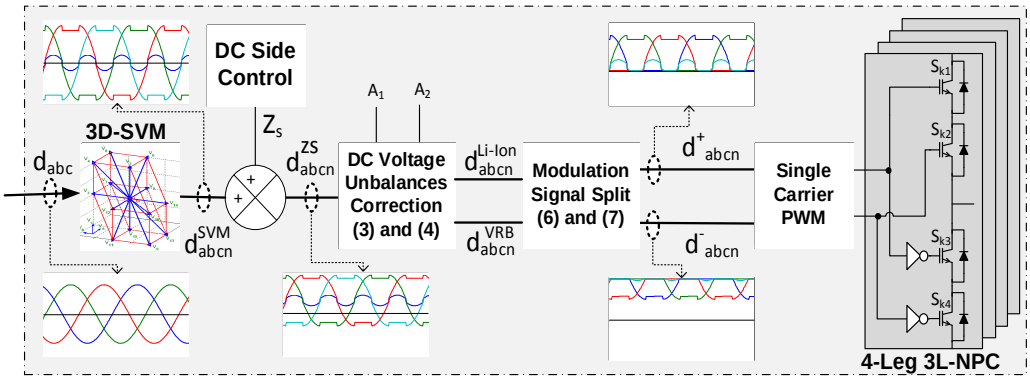

Figure 3.12 Block diagram of the modulation processing chain

$$\begin{cases} d_k^{top} = \dfrac{A_1 - 1 + d_k^{SVM} + Z_s}{A_1} P_k \qquad with\ P_k = \dfrac{1 + sign\left(\dfrac{A_1 - 1 + d_k^{SVM} + Z_s}{A_1}\right)}{2} \\ d_k^{bot} = \dfrac{A_1 - 1 + d_k^{SVM} + Z_s}{A_2} M_k + 1 \ with\ M_k = \dfrac{1 - sign\left(\dfrac{A_1 - 1 + d_k^{SVM} + Z_s}{A_2}\right)}{2} \end{cases} \tag{3.6}$$

$$\begin{cases} i_{top} = i_a d_a^{top} + i_b d_b^{top} + i_c d_c^{top} - (i_a + i_b + i_c) d_n^{top} \\ i_{bot} = i_a d_a^{bot} + i_b d_b^{bot} + i_c d_c^{bot} - (i_a + i_b + i_c) d_n^{bot} \end{cases} \tag{3.7}$$

Using the Kirchhoff's law and considering ESS simplified models as a voltage source and series resistors (neglecting self-discharge and capacitance dynamics), the DC side variables can be linked to the AC side ones as in (3.8)

$$\begin{cases} i_{top} = i_{RES} + i_1 + R_{s1} C_1 \dfrac{di_1}{dt} - C_1 \dfrac{dE_1}{dt} \\ i_{bot} = -i_{RES} - i_2 - R_{s2} C_2 \dfrac{di_2}{dt} + C_2 \dfrac{dE_2}{dt} \end{cases} \tag{3.8}$$

Finally, in spite of the use of a hybrid modulation technique, the relationship between the modulation index and the AC side line to neutral voltage amplitude can be considered as in the sinusoidal CB-PWM case. This relationship on the modulation index given in (3.9) results in the equivalence of this index and the

amplitude of the modulating signals before the 3D-SVM. It should be noted also that the relationship given in (3.9) reflects that the hybrid modulation scheme does not benefit from the SV-PWM advantage of an increased AC voltage amplitude compared with the classical sinusoidal CB-PWM modulation technique.

$$V_{rms} = m\,\frac{Udc}{2\sqrt{2}} = m\,\frac{V_1 + V_2}{2\sqrt{2}} \tag{3.9}$$

3.4 Structural limits

Although the 4 Leg 3L-NPC topology shows good specification (low current THD, high efficiency, and high power capabilities), Section 3.2.3 shows that the power division between the sources has some limits that are carefully investigated in this section.

3.4.1 Power division index

Several works have been carried out to explore the limits of the NPC topology where the DC link power has to be purposely unbalanced among the capacitors. [45], [55], [60]. These works focus on the DC link middle point current and voltage oscillation. In [65] the current division limits of the NPC topology used as an HESS interface are investigated. This comprehensive study uses the ratio between the current of each ESS over the RMS AC side current to analyse the current division limits. It comes that this current division indicator and thus the limits are dependent on the DC voltage unbalances, the modulation index and the power factor. Because these limits are dependent on several factors, and because the indicator itself is based on a ratio between AC and DC currents which is nonlinear, the limits are hard to appreciate and the implementation of these limits into the control system is difficult.

In this thesis, a new power division index is proposed. This index will be expressed using the DC mean power and AC active power instead of currents. Using a power based index will give a clearer and simpler insight of the limits which will ease the implementation in the final controller. In a first approach, the limits are going to be described considering no RES current injection on the DC bus and the DC link

capacitors removed. The next section will then implement and discuss these limits while a current is injected on the DC bus.

As aforementioned, the power division indexes K_{top} and K_{bot} can be expressed relatively to the AC side variables as the ratio between the DC mean power over one period of the fundamental frequency absorbed by the top and bottom half branches of the inverter, P_{top} and P_{bot} expressed in (3.10), and the AC active power P_{AC} in (3.11) whose current and voltage RMS values are calculated too over one period. Using (3.9) the expression of these power division indexes can be derived and result in (3.12) and (3.13), where m is the modulation index and $\cos(\varphi)$ the power factor. For the sake of clarity, these calculations are carried out considering ideal switches. This hypothesis and the consequences of the real operational limits will be discussed later on.

$$\begin{aligned} P_{top} &= \frac{1}{T}\int_0^T i_{top}\,dt * U_{C1} = < i_{top} > * U_{C1} \\ P_{bot} &= \frac{1}{T}\int_0^T i_{bot}\,dt * U_{C2} = < i_{bot} > * U_{C2} \end{aligned} \tag{3.10}$$

$$P_{AC} = V_{rms}(I_{aRMS} + I_{bRMS} + I_{cRMS})\,cos(\varphi) \tag{3.11}$$

$$K_{top} = \frac{P_{top}}{P_{AC}} = \frac{< i_{top} >}{\frac{m}{2\sqrt{2}}\left(1 + \frac{A_2}{A_1}\right)(I_{aRMS} + I_{bRMS} + I_{cRMS})\,cos(\varphi)} \tag{3.12}$$

$$K_{bot} = \frac{P_{bot}}{P_{AC}} = \frac{< i_{bot} >}{\frac{m}{2\sqrt{2}}\left(1 + \frac{A_1}{A_2}\right)(I_{aRMS} + I_{bMS} + I_{cRMS})\,cos(\varphi)} \tag{3.13}$$

Using the definition of I_{top} and I_{bot} in (3.7), the power flow distribution between each ESS can be explored for each index parameter variation. Using AC side currents of arbitrary amplitude and no zero sequence injection (Z_s=0), Figure 3.13 can be obtained for DC voltages and modulation index variations. The RMS AC side currents and DC side current mean values are calculated over one period of the fundamental frequency (i.e. 20ms). It is clear that both power division indexes are strongly dependent on the DC voltage unbalances, and to a lesser extend to the modulation index, which is consistent with the previous work carried out on this topic.

The advantage of the power based index can be noted in the variation range in [0,1]. A null index means no power is provided by the concerned ESS while if equal to one means all the power is supported by that ESS. This gives a clearer representation of the power distribution between ESSs depending on the operating point.

Also, both surfaces appear to be symmetrical and their sum is equal to one which verifies the energy conservation law as expected. Thus the power flow split among the HESS can be determined using only one index, the other one being dependent on the first one. This last consequence leads to an easier implementation in the final controller.

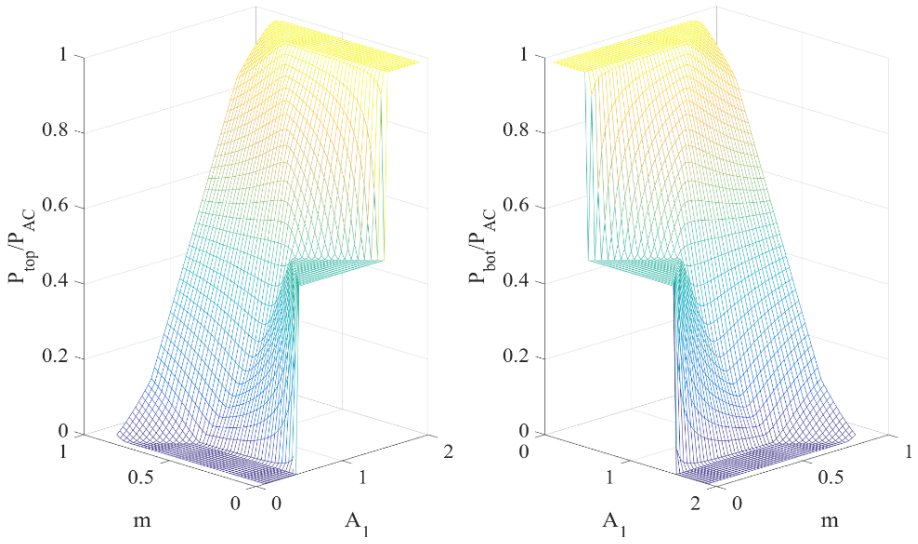

Figure 3.13 Power division indexes for DC voltages and modulation index variations (while balanced AC currents, $\cos(\varphi)$=0 and Z_s=0)

Finally, another advantage of this power based index lies in the insensitivity to the power factor or current unbalances. Indeed, even though these parameters appear in the power division indexes, the same calculation carried to obtain Figure 3.13 for different values of power factor or unbalanced currents gives exactly the same surfaces, whatever the power factor or AC current unbalances.

The constant power division among the HESS over power factor variations can be explained by the direct compensation in (3.12) and (3.13) of the DC currents I_{top}

and I_{bot} on the one hand, and the power factor on the other hand. This is corroborated by the fact that reactive power by nature does not exist in DC, and therefore does not affect the DC side mean power in a general way, and more specifically the power division.

The constant behaviour of the power index over AC side current unbalances is compensated in the same way. For an unbalance on any line, the current's RMS values of this line will be reduced in the numerator's indexes in (3.12) and (3.13). A reduction of the same magnitude can be observed in the instantaneous currents i_{top} and i_{bot} in (3.7).

So it can be concluded that the proposed power division indicators benefit from a clear representation and show the non-dependence of the power flow division between each ESS to both the power factor and AC side current unbalances. The dependence of the two indexes K_{top} and K_{bot} will finally ease further investigation and eventually the implementation in a controller.

3.4.2 RES injection on the DC bus

The previous power division analysis among the HESS has been carried out without any RES current injection on the DC bus. The power division indexes K_{top} and K_{bot} have been previously studied with the expression of I_{top} and I_{bot} in (3.7) where the RES current does not take part. Although, it takes part in the expression of these currents in (3.8). This last equation is then going to be used to generalise the power division while a RES current is injected on the DC bus.

Considering the DC link capacitor still removed and the assumption that the ESSs are constant voltage sources, equation (3.8) can be rewritten as in (3.14). Rearranging (3.3) with the DC bus voltage expression gives (3.15). Then, multiplying each member of (3.14) by V_1 and V_2 respectively, the power of each ESS can be expressed by equations (3.16). Finally, using the definition of K_{top} and K_{bot} as the ratio of the power of each ESS over the AC side active power, equations (3.16) which link the injected RES power, the AC side active power and the power division index to each ESS power can be derived.

$$\begin{cases} i_{top} = \ i_{RES} + i_1 \\ i_{bot} = -\ i_{RES} - i_2 \end{cases} \tag{3.14}$$

$$\begin{cases} V_1 = \dfrac{U_{dc}A_1}{2} \\ V_2 = \dfrac{U_{dc}A_2}{2} \end{cases} \tag{3.15}$$

$$\begin{cases} P_1 = -\dfrac{P_{res}A_1}{2} + P_{top} \\ P_2 = -\dfrac{P_{res}A_2}{2} + P_{bot} \end{cases} \tag{3.16}$$

$$\begin{cases} P_1 = -\dfrac{P_{res}A_1}{2} + K_{top}P_{ac} \\ P_2 = -\dfrac{P_{res}A_2}{2} + K_{bot}P_{ac} \end{cases} \tag{3.17}$$

Finally, even though ideal switches and ESSs have been considered to obtain these equations, it can be stated that the power flow on the DC side depending on AC side setting point is well described by (3.17) thanks to the reasonable hypothesis of a limited share of the losses and ESSs dynamics in the energy balance.

3.4.3 Structural limits exploration

The equations established in the previous section provide a relationship between the AC and DC side variables, thus the structural limits of the NPC topology can be investigated from now on. The power division among the HESS, which is defined using the indexes K_{top} and K_{bot} and has been shown to depend on DC side voltage unbalances as well as modulation index, is also dependent on the zero sequence injection signal Z_s. This last variable being used for power division control, its implication on the limits is thus preponderant. Also, among the final equations that describe the whole system power flow given in (3.17), only the power division indexes depend on Z_s, therefore the structural limits of the topology are going to be preliminary investigated relatively to the power division indexes.

It can be considered that the limits are reached when the modulation signals after the whole processing chain reach the carrier boundaries, which is in the range [0,1]. This can be traduced by letting d_{abcn}^{top} and d_{abcn}^{bot} defined in (3.6) being equal to

one and zero respectively. Using the definition of the modulation signals d_{abcn}^{SVM} maximum and minimum values in (3.1) it comes that maximum and minimum zero sequence can be expressed as in (3.18). It is interesting to see that these extremes values of the zero sequence signal depend only on the max/min values of the 3D-SVM output's modulation signals and do not depend on the DC voltage unbalances factors which is unintuitive.

$$\begin{cases} Z_s^{max} = 1 - max(d_{abcn}^{SVM}) \\ Z_s^{min} = min(d_{abcn}^{SVM}) - 1 \end{cases} \tag{3.18}$$

These extreme values that the Z_s a variable can reach represents the boundary of the power division control range, and thus the operational limits of the system. To analyse these limits in term of power division, and to include the sensitivity on DC voltage unbalances and modulation index, the indexes K_{top} and K_{bot} can be drawn out again for those extreme values of Z_s.

Figure 3.14 and Figure 3.15 show the previously defined power division indexes for maximum and minimum zero sequence injection respectively, and still, no RES current injected on the DC bus. As expected the surfaces are in the range [0,1] and the sum of both in each case is equal to one. It is clear from these results that the DC voltage unbalances is the main factor for power division between each ESS. The effect on the limits of the modulation index, and thus the 3D-SVM output modulation signals amplitude, appears to have an effect from $m>\sqrt{3}/3$ which matches the transition from constant to variable values of $\max(d_{abcn}^{SVM})$ as described by (3.1) and observed in Figure 3.10. The benefit of the power based indexes to interpret the power division limits is clear. In the case of maximum Z_s injection and $V_1>V_2$ for example (equivalent to $A_1>1$), it can be seen that the total AC side power can be supplied by the top ESS ($K_{top}^{Zs\,max}=1$) as long as $m<\sqrt{3}/3$.

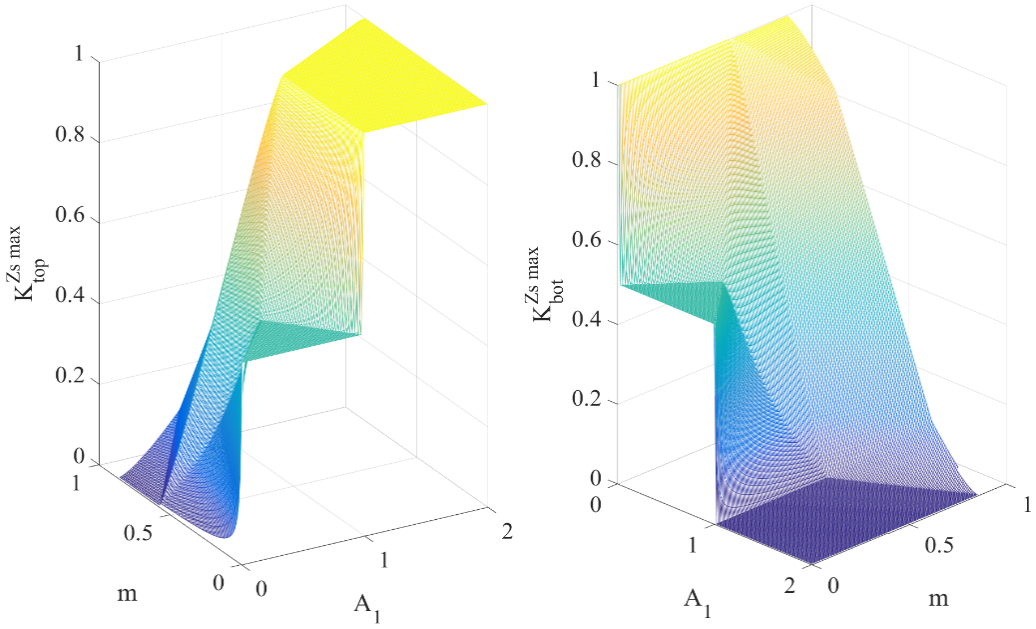

Figure 3.14 Power division indexes for maximum zero sequence injection while DC voltages and modulation index variations

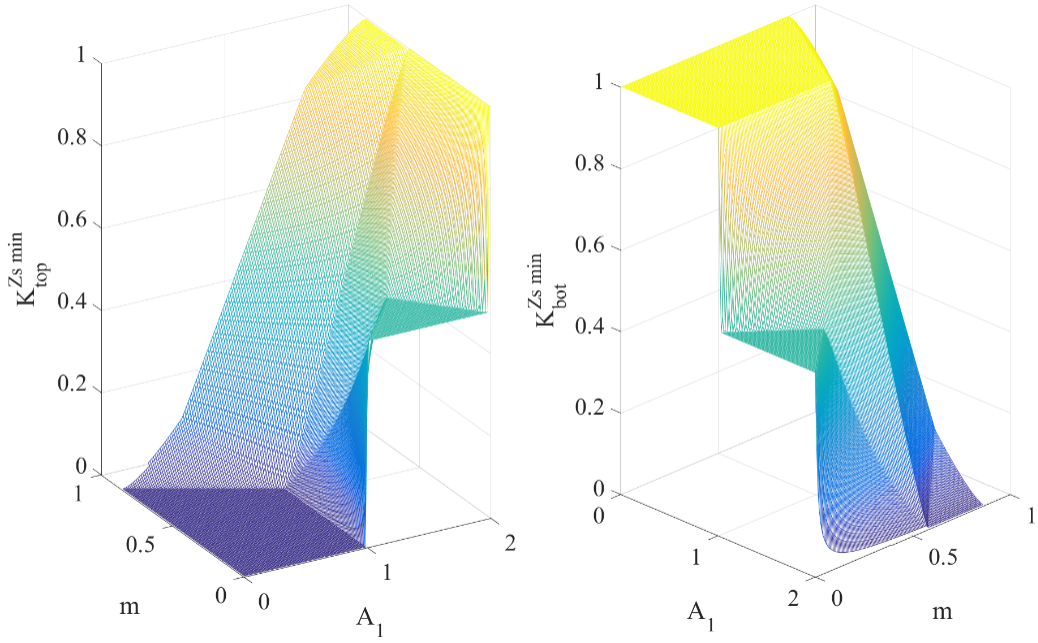

Figure 3.15 Power division indexes for minimum zero sequence injection while DC voltages and modulation index variations

In the same way as the previous observations, the power division indexes at maximum and minimum zero sequence injection can be drawn again for several values of power factor and AC side current unbalances. Regardless of the setting points, the surfaces remain unchanged which allow the assumption that the power division limits do not depend on both power factor and unbalanced AC currents.

In the case of RES current injection, the indexes remain the same as well, and thus the power division limits for maximum and minimum zero sequence injection too. Therefore these surfaces can be implemented in (3.17) to obtain the upper and lower power limits of each ESS, for any variation of RES current injected. This can be expressed for the top ESS by equation (3.19) and can be obtained symmetrically for the bottom ESS, or using the complementarity property of the power division index which results in (3.20).

$$\begin{cases} P_1^{max} = -\dfrac{P_{res}A_1}{2} + K_{top}^{Z_s\,max}\,P_{ac} \\ P_1^{min} = -\dfrac{P_{res}A_1}{2} + K_{top}^{Z_s\,min}\,P_{ac} \end{cases} \tag{3.19}$$

$$\begin{cases} P_2^{max} = -\dfrac{P_{res}A_1}{2} + (1 - K_{top}^{Z_s\,max})\,P_{ac} \\ P_2^{min} = -\dfrac{P_{res}A_1}{2} + (1 - K_{top}^{Z_s\,min})\,P_{ac} \end{cases} \tag{3.20}$$

Finally, the whole structural limits of the NPC inverter used as a HESS and RES interface to the grid can be implemented using (3.19) and one of the surfaces in Figure 3.14 and Figure 3.15 in the final controller, which enable tracking in real time the power flow limits of each ESS. Even though the power division maximum and minimum surfaces have to be implemented in a look-up table, the computational cost of the limits calculation is low thanks to the simplicity of equations (3.19) and (3.20). The accuracy of the calculated limits assuming ideal switches and ESSs will be discussed in the next section.

3.4.4 Structural limits validation

It has been shown that the structural limits of the NPC topology used as a unique interface for HESS and RES integration to the grid lies in the zero sequence

injection maximum range defined in (3.18). The equation (3.19) and (3.20) are also considered to describe the upper and lower power bounds that each ESS can reach, whatever the modulation index, the DC voltage unbalances, the RES power injected, the AC current unbalances and the power factor.

To test these limits, simulations have been carried out using a detailed model of the 4 Leg 3L-NPC inverter in Matlab/Simulink using real IGBTs model. The ESSs are replaced by variable voltage sources to obtain a constant DC bus voltage of 1000V. A small resistor of 0.1Ω is placed in series with the voltage source so the DC link capacitive filter can be effective and remove the highest frequency current harmonics. The RES injection is modelled by an ideal current source whose setpoint is defined for the desired RES power divided by the bus voltage. The modulation signals processing chain has been implemented along with the 3D-SVM algorithm as an S-Function in Simulink. The inverter operates in open loop so the modulation index can be set manually, and feed a balanced star connected resistor of 7.3Ω. The schematic of the whole simulation configuration is given in Figure 3.16. Finally, the power upper and lower bounds of each ESSs are calculated using (3.19) and (3.20), and using the maximum and minimum power division indexes surfaces of Figure 3.14 and Figure 3.15 implemented as look up tables.

To assess the modelled limits developed previously for a wide range of parameter variations, the variables involved in the structural limits will vary as follow:

- **RES power injection**: a sinusoidal signal of a 1Hz frequency and 20kW amplitude using the DC bus voltage to determine the current set point.
- **Zero sequence injection**: sinusoidal signal of 10Hz frequency and amplitude defined in equation (3.18).
- **DC voltages**: linear variation from 600V to 400V for V_1 and the opposite for V_2 in order to keep the DC bus voltage constant at 1000V. It corresponds to the variation of A_1 from 1.2 to 0.8 and the opposite for A_2.
- **Modulation index**: linear variation from 0.2 to 0.8 of the 3D-SVM input modulation signals amplitude.

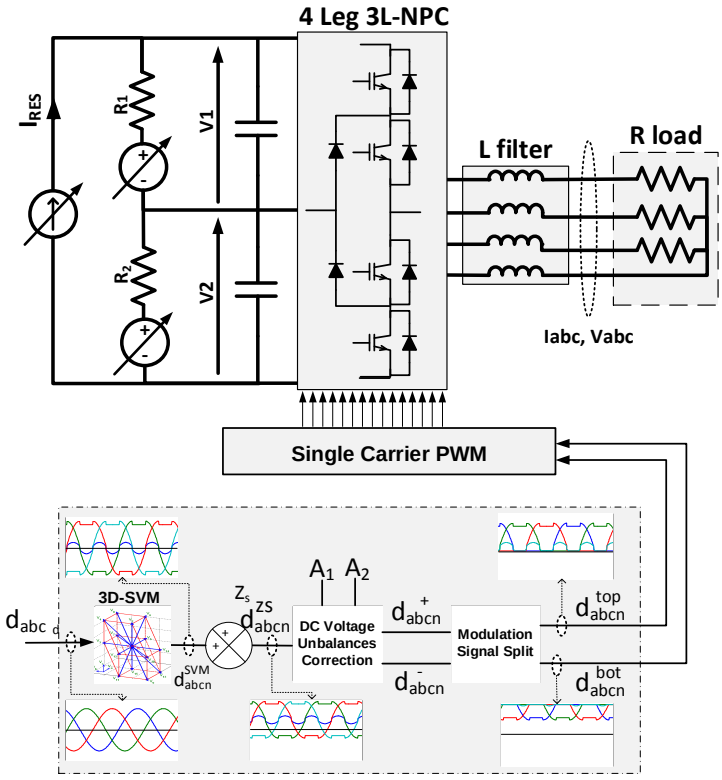

Figure 3.16 Simulation configuration for limits assessment

These variations can be observed in Figure 3.17 for the modulation index and the resulting value of $\max(d_{abcn}^{SVM})$ (a) which is used to compute the zero sequence amplitude (c) the evolution of the HESS voltages (d) and the RES power injected, along with the AC side active power variation resulting from modulation index variation (b). The evolution of these last variables is used to compute in real time the boundaries of both ESSs power while the zero sequence, and thus the power of each ESSs, alternate between their maximum and minimum allowed values as depicted in Figure 3.18. The amplitude of RES injection on the DC bus has been chosen according to the load active power in order to test cases where the RES power is strictly inferior to the load's one. The sine profile of RES injection at 1Hz has been chosen to test the ability of the limits model to be computed even though fast variations occurs on the DC bus.

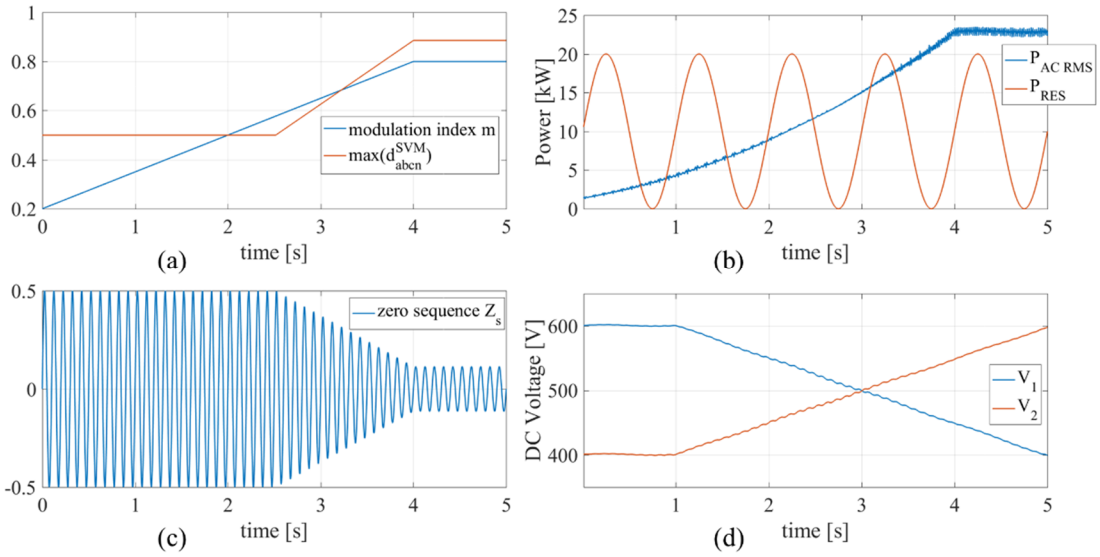

Figure 3.17 Limits model assessment: variation of modulation index (a) RES power and AC side active power (b) zero sequence injection (c) and DC voltages (d)

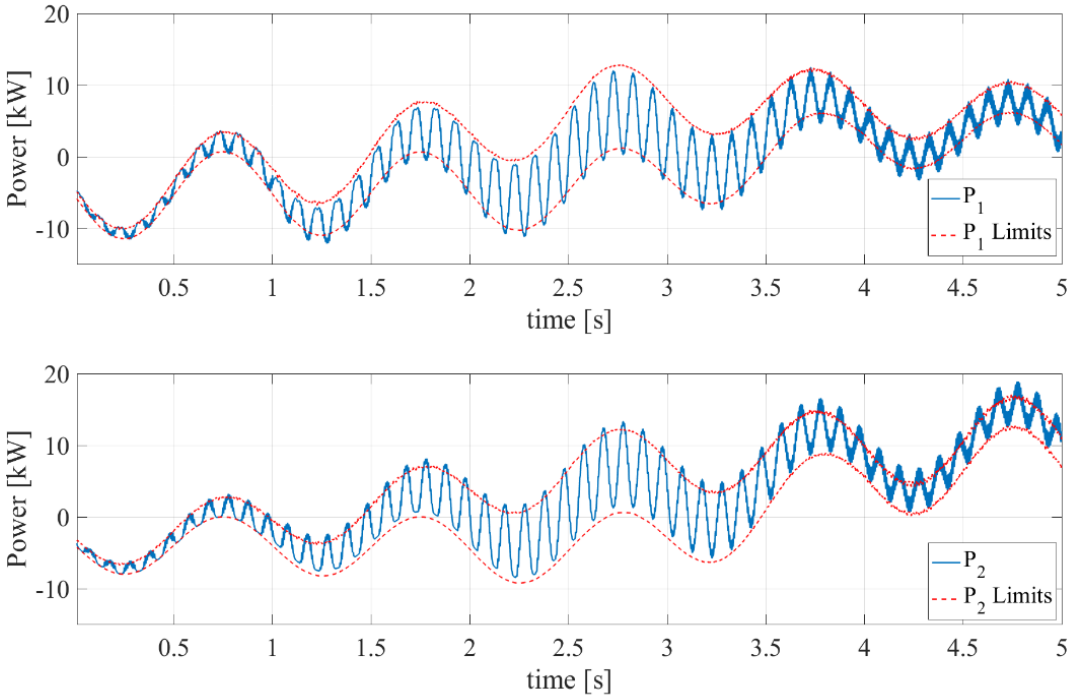

Figure 3.18 Limits model assessment: resulting power of top and bottom ESS along with the computed limits of (3.19) and (3.20)

In the first place it can be seen in Figure 3.18 there is a good agreement between the limits model given in (3.19) and (3.20) and the real boundaries of each ESSs

power. The slight shift that can be observed can be explained by the fact that a simplified model of the DC side has been considered to obtain the limits model. Another factor in these differences may come from the approximation made on the modulation index which has been considered equal to the amplitude of the 3D-SVM modulation signal input.

The maximum amplitude of both ESSs' power varies as a function of the modulation index and the DC voltage unbalances, but do not depend on the RES power injection which validates the assumption that the power division indexes K_{top} and K_{bot} at the limits can be determined considering no RES injection, and also that the surface of maximum and minimum zero sequence injection (Figure 3.14 and Figure 3.15) are only translated on z axis while RES injection. This can be observed in Figure 3.19 where the amplitude of both power ESSs do not present any 1Hz component.

Figure 3.19 shows also that the maximum power amplitude is equal for both ESSs which confirms the symmetries observed for $K_{top}^{Zs\,max}$, $K_{bot}^{Zs\,max}$ and $K_{top}^{Zs\,min}$, $K_{bot}^{Zs\,min}$ and thus their equivalence. Therefore it confirm the assumption that only one of those surfaces is necessary to compute the limits of both ESSs and will ease their implementation.

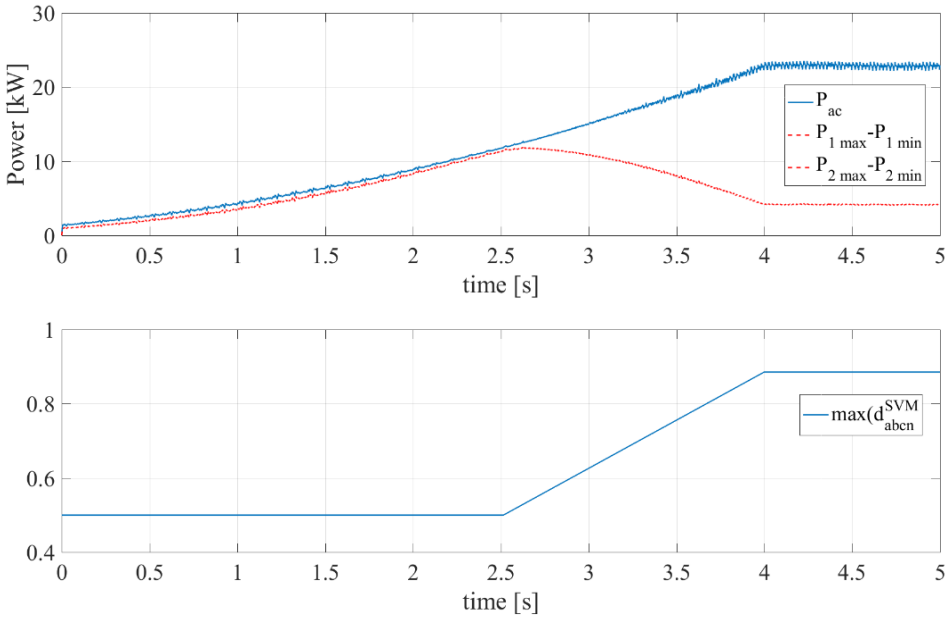

Figure 3.19 Active power and ESSs power maximum amplitude

Another point should be highlighted on the impact of the zero sequence signal injection on the AC side waveform. The active power signal noise reflects the harmonic content of the AC currents and voltages. It can be seen that even though the Z_s signal which is injected in the modulation signals oscillates at 10Hz, the impact on the AC side harmonic is limited, and especially considering that the system is in open loop.

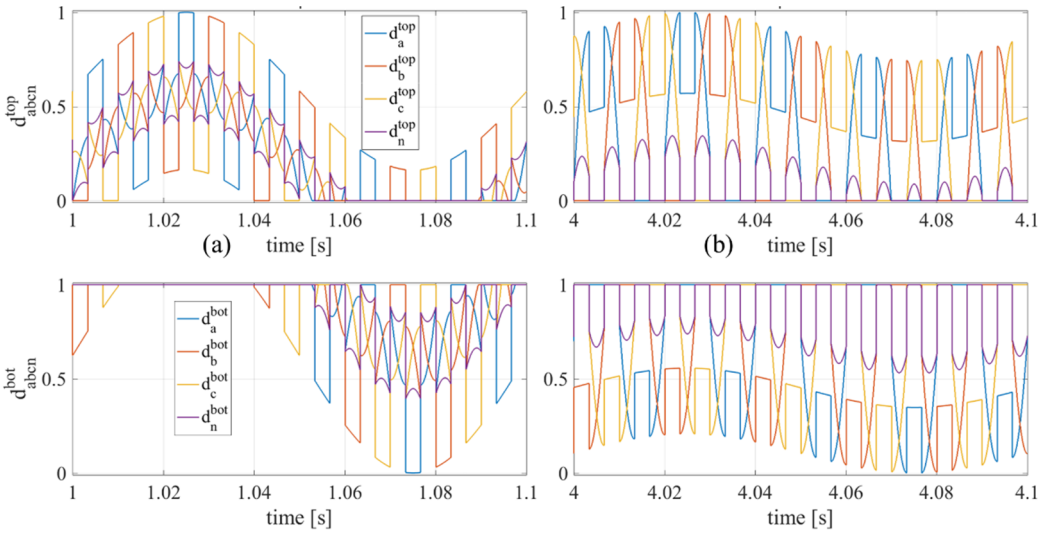

Figure 3.20 Modulation signals for (a) m=0.36 A1=1.19 (b) m=0.8 A1=0.9

The low noise on the active power suggests also that the over modulation bounds [0,1] are not reached, which can be observed for different setting points in Figure 3.20 and thus validate the equation (3.18).

3.4.5 Energy exchange among the HESS

It can be noted in Figure 3.19 that the maximum ESSs power amplitudes start decreasing from $m=\sqrt{3}/3$. Until this value these amplitudes are equal to the active power and thus the whole active power can be supplied by one or the other ESS. For RES power set points lower than the active power, it can be observed that the maximum power bound of one ESS is positive while the lower bound of the other ESS is negative. Thus the ESSs power can be of opposite signs which means that one ESS is charging while the other one is discharging and supplying the AC side load.

This phenomenon shows that the topology allows the RES power injected on the DC bus to split in two flows. One share of the RES power flow is directed to supply the AC side load and complete the power supplied by the first ESS, while the other share is used to charge the second ESS. This is equivalent to an energy exchange from one ESS to the other from a macro point of view, and enables management strategies like SOC balancing for instance.

3.5 Chapter conclusion

In this chapter different MG structures have been reviewed. The hybrid MG structure using both AC and DC subgrids presents an increased efficiency, flexibility, reliability and easier control than pure AC or DC MGs. To interface several ESS and RES, and more generally AC and DC subgrids, the NPC topology has shown advantages such as increased efficiency and power capabilities along with reduced AC side harmonic content. In addition to the reduced current THD of the NPC, the addition of a 4^{th} leg on the inverter allow even more improvement in power quality and work in critical conditions with unbalances/nonlinear loads. The NPC topology structural limits have been studied with a new power based indicator that gives a clear and accurate description of these limits. Despite the fact that this topology does not offer the full flexibility of the parallel topology, the NPC topology used as a HESS and RES interface to an AC grid still allow full power split between ESSs for modulation index under $\sqrt{3}/3$, and depends mainly on the DC voltage unbalances. It has also been shown that for certain RES power set points lower than AC side active power, it is possible to charge one ESS while discharging the other which is equivalent to an energy transfer from one ESS to the other.

3.6 Chapter references

[1] A. Kalair, N. Abas, and N. Khan, "Comparative study of HVAC and HVDC transmission systems," *Renew. Sustain. Energy Rev.*, vol. 59, pp. 1653–1675, 2016.

[2] M. Ashouri, C. L. Bak, and F. Faria Da Silva, "A review of the protection algorithms for multi-terminal VCD-HVDC grids," *Proc. IEEE Int. Conf. Ind. Technol.*, vol. 2018-Febru, pp. 1673–1678, 2018.

[3] M. Zia, E. Elbouchikhi, and M. Benbouzid, "Microgrids energy management systems: A critical review on methods, solutions, and prospects," *Appl. Energy*, vol. 222, pp. 1033–1055, Jul. 2018.

[4] J. Rocabert, A. Luna, F. Blaabjerg, and P. Rodríguez, "Control of Power Converters in AC Microgrids," *IEEE Trans. Power Electron.*, vol. 27, no. 11, pp. 4734–4749, Nov. 2012.

[5] J. Han, S. K. Solanki, and J. Solanki, "Coordinated predictive control of a wind/battery microgrid system," *IEEE J. Emerg. Sel. Top. Power Electron.*, vol. 1, no. 4, pp. 296–305, 2013.

[6] S. M. Nosratabadi, R. A. Hooshmand, and E. Gholipour, "A comprehensive review on microgrid and virtual power plant concepts employed for distributed energy resources scheduling in power systems," *Renewable and Sustainable Energy Reviews*, vol. 67. pp. 341–363, Jan-2017.

[7] V. Nasirian, Q. Shafiee, J. M. Guerrero, F. L. Lewis, and A. Davoudi, "Droop-Free Distributed Control for AC Microgrids," *IEEE Trans. Power Electron.*, vol. 31, no. 2, pp. 1600–1617, Feb. 2016.

[8] J. M. Guerrero, P. C. Loh, T. L. Lee, and M. Chandorkar, "Advanced control architectures for intelligent microgridsPart II: Power quality, energy storage, and AC/DC microgrids," *IEEE Trans. Ind. Electron.*, vol. 60, no. 4, pp. 1263–1270, Apr. 2013.

[9] U. B. Tayab, X. Lu, L. Setyawan, K. Sun, and J. C. Vasquez, "State-of-Charge Balance Using Adaptive Droop Control for Distributed Energy Storage Systems in DC Microgrid Applications," *IEEE Trans. Ind.*

Electron., vol. 61, no. 6, pp. 2804–2815, Jun. 2014.

[10] A. Maknouninejad, Z. Qu, F. L. Lewis, and A. Davoudi, "Optimal, Nonlinear, and Distributed Designs of Droop Controls for DC Microgrids," *IEEE Trans. Smart Grid*, vol. 5, no. 5, pp. 2508–2516, Sep. 2014.

[11] W. Jing, C. H. Lai, S. H. W. Wong, and M. L. D. Wong, "Battery-supercapacitor hybrid energy storage system in standalone DC microgrids: areview," *IET Renew. Power Gener.*, vol. 11, no. 4, pp. 461–469, 2016.

[12] J. Xiao, P. Wang, and L. Setyawan, "Hierarchical Control of Hybrid Energy Storage System in DC Microgrids," *IEEE Trans. Ind. Electron.*, vol. 62, no. 8, pp. 4915–4924, Aug. 2015.

[13] C. Yin, H. Wu, F. Locment, and M. Sechilariu, "Energy management of DC microgrid based on photovoltaic combined with diesel generator and supercapacitor," *Energy Convers. Manag.*, vol. 132, pp. 14–27, Jan. 2017.

[14] L. Dos Santos, M. Sechilariu, and F. Locment, "Day-ahead microgrid optimal self-scheduling: Comparison between three methods applied to isolated DC microgrid," in *IECON 2014-40th Annual Conference of the IEEE Industrial Electronics Society*, 2014, pp. 2010–2016.

[15] E. Jiménez, M. J. Carrizosa, A. Benchaib, G. Damm, and F. Lamnabhi-Lagarrigue, "A new generalized power flow method for multi connected DC grids," *Int. J. Electr. Power Energy Syst.*, vol. 74, pp. 329–337, 2016.

[16] B. Wang, M. Sechilariu, and F. Locment, "Intelligent DC Microgrid With Smart Grid Communications: Control Strategy Consideration and Design," *IEEE Trans. Smart Grid*, vol. 3, no. 4, pp. 2148–2156, Dec. 2012.

[17] A. Benchaib and M. J. Carrizosa, "Bidirectional multi-level DC/DC converter with an independent control module for each conversion stage," 2017.

[18] X. Lu, J. M. Guerrero, K. Sun, J. C. Vasquez, R. Teodorescu, and L. Huang, "Hierarchical Control of Parallel AC-DC Converter Interfaces for Hybrid Microgrids," *IEEE Trans. Smart Grid*, vol. 5, no. 2, pp. 683–692, Mar. 2014.

[19] J. M. Guerrero, D. Li, and F. Blaabjerg, "Autonomous Operation of Hybrid

Microgrid With AC and DC Subgrids," *IEEE Trans. Power Electron.*, vol. 28, no. 5, pp. 2214–2223, May 2013.

[20] J. M. Guerrero, J. C. Vasquez, J. Matas, L. G. de Vicuña, and M. Castilla, "Hierarchical Control of Droop-Controlled AC and DC Microgrids #x2014;A General Approach Toward Standardization," *IEEE Trans. Ind. Electron.*, vol. 58, no. 1, pp. 158–172, Jan. 2011.

[21] J. M. Guerrero, P. C. Loh, T. L. Lee, and M. Chandorkar, "Advanced control architectures for intelligent microgridsPart II: Power quality, energy storage, and AC/DC microgrids," *IEEE Trans. Ind. Electron.*, vol. 60, no. 4, pp. 1263–1270, Apr. 2013.

[22] T. Logenthiran, D. Srinivasan, A. M. Khambadkone, and H. N. Aung, "Multiagent System for Real-Time Operation of a Microgrid in Real-Time Digital Simulator," *IEEE Trans. Smart Grid*, vol. 3, no. 2, pp. 925–933, Jun. 2012.

[23] X. Liu, P. Wang, and P. C. Loh, "A Hybrid AC/DC Microgrid and Its Coordination Control," *IEEE Trans. Smart Grid*, vol. 2, no. 2, pp. 278–286, Jun. 2011.

[24] L. Gao, R. A. Dougal, and S. Liu, "Power enhancement of an actively controlled battery/ultracapacitor hybrid," *IEEE Trans. Power Electron.*, vol. 20, no. 1, pp. 236–243, Jan. 2005.

[25] L. Palma, P. Enjeti, and J. W. Howze, "An approach to improve battery run-time in mobile applications with supercapacitors," *IEEE 34th Annu. Conf. Power Electron. Spec. 2003. PESC '03.*, vol. 2, pp. 918–923, Jun. 2003.

[26] Z. Guoju, T. Xisheng, and Q. Zhiping, "Research on Battery Supercapacitor Hybrid Storage and its application in MicroGrid," in *Asia-Pacific Power and Energy Engineering Conference, APPEEC*, 2010, pp. 1–4.

[27] H. Babazadeh, W. Gao, and X. Wang, "Controller design for a Hybrid Energy Storage System enabling longer battery life in wind turbine generators," in *2011 North American Power Symposium*, 2011, pp. 1–7.

[28] J. D. Maclay, J. Brouwer, and G. S. Samuelsen, "Dynamic modeling of hybrid energy storage systems coupled to photovoltaic generation in residential applications," *J. Power Sources*, vol. 163, no. 2, pp. 916–925, Jan. 2007.

[29] C. Abbey, K. Strunz, and G. Joos, "A Knowledge-Based Approach for Control of Two-Level Energy Storage for Wind Energy Systems," *IEEE Trans. Energy Convers.*, vol. 24, no. 2, pp. 539–547, Jun. 2009.

[30] W. Li, G. Joos, and J. Belanger, "Real-Time Simulation of a Wind Turbine Generator Coupled With a Battery Supercapacitor Energy Storage System," *IEEE Trans. Ind. Electron.*, vol. 57, no. 4, pp. 1137–1145, Apr. 2010.

[31] P. Thounthong, S. Raël, and B. Davat, "Energy management of fuel cell/battery/supercapacitor hybrid power source for vehicle applications," *J. Power Sources*, vol. 193, no. 1, pp. 376–385, Aug. 2009.

[32] H. Zhou, T. Bhattacharya, D. Tran, T. S. T. Siew, and A. M. Khambadkone, "Composite Energy Storage System Involving Battery and Ultracapacitor With Dynamic Energy Management in Microgrid Applications," *IEEE Trans. Power Electron.*, vol. 26, no. 3, pp. 923–930, Mar. 2011.

[33] F. Liu, J. Liu, and L. Zhou, "A novel control strategy for hybrid energy storage system to relieve battery stress," in *Power Electronics for Distributed Generation Systems (PEDG), 2010 2nd IEEE International Symposium on*, 2010, pp. 929–934.

[34] Y. Z. Y. Zhang, Z. J. Z. Jiang, and X. Y. X. Yu, "Control Strategies for Battery/Supercapacitor Hybrid Energy Storage Systems," in *2008 IEEE Energy 2030 Conference*, 2008, pp. 5–10.

[35] A. L. Allègre, R. Trigui, and A. Bouscayrol, "Different energy management strategies of Hybrid Energy Storage System (HESS) using batteries and supercapacitors for vehicular applications," in *2010 IEEE Vehicle Power and Propulsion Conference, VPPC 2010*, 2010, pp. 1–6.

[36] S. D. G. Jayasinghe, D. M. Vilathgamuwa, and U. K. Madawala, "A new method of interfacing battery/supercapacitor energy storage systems for distributed energy sources," in *IPEC, 2010 Conference Proceedings*, 2010, pp. 1211–1216.

[37] S. D. G. Jayasinghe, D. M. Vilathgamuwa, and U. K. Madawala, "A direct integration scheme for battery-supercapacitor hybrid energy storage systems with the use of grid side inverter," 2011, pp. 1388–1393.

[38] S. S. G. Jayasinghe, D. M. Vilathgamuwa, and U. K. Madawala, "Diode-Clamped Three-Level Inverter-Based Battery/Supercapacitor Direct Integration Scheme for Renewable Energy Systems," *IEEE Trans. Power Electron.*, vol. 26, no. 12, pp. 3720–3729, Dec. 2011.

[39] A. Etxeberria, I. Vechiu, H. Camblong, and J.-M. Vinassa, "Comparison of three topologies and controls of a hybrid energy storage system for microgrids," *Energy Convers. Manag.*, vol. 54, no. 1, pp. 113–121, Feb. 2012.

[40] L. G. Franquelo, J. Rodriguez, J. I. Leon, S. Kouro, R. Portillo, and M. a M. Prats, "The age of multilevel converters arrives," *IEEE Ind. Electron. Mag.*, vol. 2, no. June, pp. 28–39, 2008.

[41] S. A. Amamra, K. Meghriche, A. Cherifi, and B. Francois, "Multilevel Inverter Topology for Renewable Energy Grid Integration," *IEEE Trans. Ind. Electron.*, vol. PP, no. 99, pp. 1–1, 2016.

[42] S. BACHA, I. MUNTEANU, and A. I. BRATCU, "Power Electronic Converters Modeling and Control," in *Advanced textbooks in control and signal processing*, 2014.

[43] Y. Touzani, L. Kefsi, G. Champenois, and J.-P. Gaubert, "Two-directional current double-boost quadratic DC/DC converter," 2015.

[44] I. Vechiu, A. Etxeberria, H. Camblong, and Q. Tabart, "Control of a microgrid-connected hybrid energy storage system," in *Renewable Energy Research and Application (ICRERA), 2014 International Conference on*, 2014, pp. 412–417.

[45] N. Celanovic and D. Boroyevich, "A comprehensive study of neutral-point

voltage balancing problem in three-level neutral-point-clamped voltage source PWM inverters," *IEEE Trans. Power Electron.*, vol. 15, no. 2, pp. 242–249, Mar. 2000.

[46] Q. Tabart, I. Vechiu, A. Etxeberria, and S. Bacha, "Hybrid Energy Storage System MicroGrids Integration for Power Quality Improvement Using Four Leg Three Level NPC Inverter and Second Order Sliding Mode Control," *IEEE Trans. Ind. Electron.*, vol. 65, no. 1, pp. 424–435, 2018.

[47] W. Zhao, X. Ruan, D. Yang, X. Chen, and L. Jia, "Neutral Point Voltage Ripple Suppression for a Three-Phase Four-Wire Inverter With an Independently Controlled Neutral Module," *IEEE Trans. Ind. Electron.*, vol. 64, no. 4, pp. 2608–2619, Apr. 2017.

[48] A. Chebabhi, M. K. Fellah, A. Kessal, and M. F. Benkhoris, "A new balancing three level three dimensional space vector modulation strategy for three level neutral point clamped four leg inverter based shunt active power filter controlling by nonlinear back stepping controllers," *ISA Trans.*, vol. 63, pp. 328–342, Apr. 2016.

[49] P. Acuña, L. Morán, M. Rivera, R. Aguilera, R. Burgos, and V. G. Agelidis, "A Single-Objective Predictive Control Method for a Multivariable Single-Phase Three-Level NPC Converter-Based Active Power Filter," *IEEE Trans. Ind. Electron.*, vol. 62, no. 7, pp. 4598–4607, Jul. 2015.

[50] F. Sebaaly, H. Vahedi, H. Y. Kanaan, N. Moubayed, and K. Al-Haddad, "Design and Implementation of Space Vector Modulation-Based Sliding Mode Control for Grid-Connected 3L-NPC Inverter," *IEEE Trans. Ind. Electron.*, vol. 63, no. 12, pp. 7854–7863, Dec. 2016.

[51] F. Umbría, F. Gordillo, F. Gómez-Estern, F. Salas, R. C. Portillo, and S. Vázquez, "Voltage balancing in three-level neutral-point-clamped converters via Luenberger observer," *Control Eng. Pract.*, vol. 25, pp. 36–44, 2014.

[52] Y. Deng, K. H. Teo, C. Duan, T. G. Habetler, and R. G. Harley, "A Fast and Generalized Space Vector Modulation Scheme for Multilevel Inverters," *IEEE Trans. Power Electron.*, vol. 29, no. 10, pp. 5204–5217, Oct. 2014.

[53] M. Barghi Latran and A. Teke, "Investigation of multilevel multifunctional grid connected inverter topologies and control strategies used in photovoltaic systems," *Renewable and Sustainable Energy Reviews*, vol. 42. pp. 361–376, Feb-2015.

[54] C. Zang, Z. Pei, J. He, G. Ting, J. Zhu, and W. Sun, "Comparison and analysis on common modulation strategies for the cascaded multilevel STATCOM," in *Proceedings of the International Conference on Power Electronics and Drive Systems*, 2009, pp. 1439–1442.

[55] J. Pou, J. Zaragoza, S. Ceballos, M. Saeedifard, and D. Boroyevich, "A Carrier-Based PWM Strategy With Zero-Sequence Voltage Injection for a Three-Level Neutral-Point-Clamped Converter," *IEEE Trans. Power Electron.*, vol. 27, no. 2, pp. 642–651, Feb. 2012.

[56] A. Iqbal and S. Moinuddin, "Comprehensive Relationship Between Carrier-Based PWM and Space Vector PWM in a Five-Phase VSI," *IEEE Trans. Power Electron.*, vol. 24, no. 10, pp. 2379–2390, Oct. 2009.

[57] W. Yao, H. Hu, and Z. Lu, "Comparisons of Space-Vector Modulation and Carrier-Based Modulation of Multilevel Inverter," *IEEE Trans. Power Electron.*, vol. 23, no. 1, pp. 45–51, Jan. 2008.

[58] X. Peng, X. He, P. Han, H. Lin, Z. Shu, and S. Gao, "Opposite Vector Based PSC-SVPWM for Extending the Voltage Balance Region in Single-phase 3LNPC Cascaded Rectifier," *IEEE Trans. Power Electron.*, vol. PP, no. 99, pp. 1–1, 2016.

[59] Z. Zhang, O. C. Thomsen, and M. a E. Andersen, "Discontinuous PWM modulation strategy with circuit-level decoupling concept of three-level Neutral-Point-Clamped (NPC) inverter," *IEEE Trans. Ind. Electron.*, vol. 60, no. 5, pp. 1897–1906, 2013.

[60] X. Wu, G. Tan, G. Yao, C. Sun, and G. Liu, "A Hybrid PWM Strategy for Three-Level Inverter With Unbalanced DC-links," *IEEE J. Emerg. Sel. Top. Power Electron.*, vol. PP, no. 99, pp. 1–1, 2017.

[61] M. A. Perales, M. M. Prats, R. Portillo, J. L. Mora, J. I. Leon, and L. G.

Franquelo, "Three-dimensional space vector modulation in abc coordinates for four-leg voltage source converters," *IEEE Power Electron. Lett.*, vol. 1, no. 4, pp. 104–109, Dec. 2003.

[62] I. Vechiu, O. Curea, and H. Camblong, "Transient Operation of a Four-Leg Inverter for Autonomous Applications With Unbalanced Load," *IEEE Trans. Power Electron.*, vol. 25, no. 2, pp. 399–407, Feb. 2010.

[63] A. Etxeberria, "Microgrid Hybrid Energy Storage Integration and Control using a Three-Level NPC Converter," *Ph.D. dissertation*, 2012.

[64] N. Celanovic, "Space Vector Modulation and Control of Multilevel Converters," 2000.

[65] A. Etxeberria, I. Vechiu, H. Camblong, S. Kreckelbergh, and S. Bacha, "Operational limits of a three level neutral point clamped converter used for controlling a hybrid energy storage system," *Energy Convers. Manag.*, vol. 79, pp. 97–103, Mar. 2014.

Chapter 4

Control of a 3L-NPC based HESS and RES multipurpose interface

Contents

4.1 Hierarchical control in hybrid power plants

Any aggregated systems in general, and particularly a power plant made of several DGs along with ESSs, can be decomposed in several layers with hierarchical relationships between each other. Control and management of such systems can then be split into several subsystems, each of them dedicated to a specific layer, and often associated with a specific time step range. Each control layer can either be implemented in a centralized or decentralised fashion as a consequence.

Several approaches have been explored for the standardisation of hierarchical control applied to MGs and virtual power plants. In [1], the hierarchical control design is based on existing frameworks such as the IEC/ISO 62264 which is equivalent to the ANSI/ISA-95 standard and aims to improve the interface between the business and the system control. The advantage of this approach lies in the scalability of such a framework as reported in [2]. Indeed the hierarchical control architecture suits small applications like MGs as well as larger systems such as VPPs, which makes it very popular in both MG and VPP research.

In this section, following the aforementioned standardisation of the hierarchical control based on IEC/ISO 62264, the definition and specification of the different layers are discussed, and the general structure of a hierarchical controller is developed. Finally, the hierarchical structure framework will be used to design both AC and DC side controls.

4.1.1 General structure and level definition

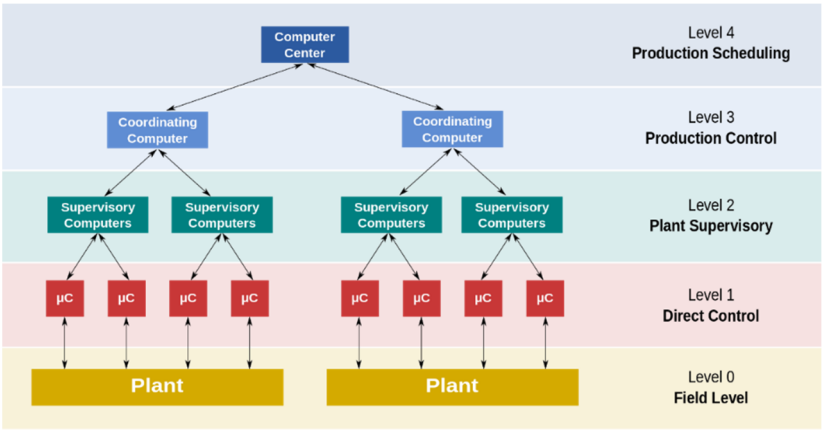

Figure 4.1 hierarchical control level definition

A hierarchical controller is composed of several homogeneous layers. The IEC/ISO 62264 standard recommends that the higher the level is, the more abstract the control is. Thus lower level executes precise control tasks using specific controllers, often at low sampling time, while a higher level realizes more abstract control objectives at a lower frequency. Figure 4.1 shows the different level definition and integration of a hierarchical control scheme. The standard specifies five levels, from field level control to production scheduling, but it can vary depending on the application complexity where more or fewer levels are needed. The general level definition and what each of them encompasses is the following:

- **Level 0 – Field level** contains sensors and control element devices.
- **Level 1 – Direct control** encompasses industrial modules and their associated electronic processors.
- **Level 2 – Plant supervisory** contains the supervisory computers, which collect information from the subsystem's nodes
- **Level 3 – Production control** monitor production and targets
- **Level 4 – Production scheduling** plans ahead using forecast and optimisation

4.1.2 Power plant hierarchical control

The aforementioned structure has been developed for any kind of industrial application, therefore some relevant modifications can be operated in order to suit the specification of a power plant hierarchical control. In the literature, most of the hierarchical controls developed have 3 to 4 levels maximum depending on the complexity [3]–[7]. When applied to the case study of a multipurpose power converter used to interface a HESS and a RES to the grid, the hierarchical control can be translated into the structure depicted in Figure 4.2.

In this work the first and second layers of the control will be developed, the third one being out of the scope of this thesis. The first layer encompasses the measurement and its associated data processing, along with the direct control of the power converter. This layer operates at high bandwidth and is set at 100µs. The second layer will contain the ancillary services and will be in charge of defining the set points values.

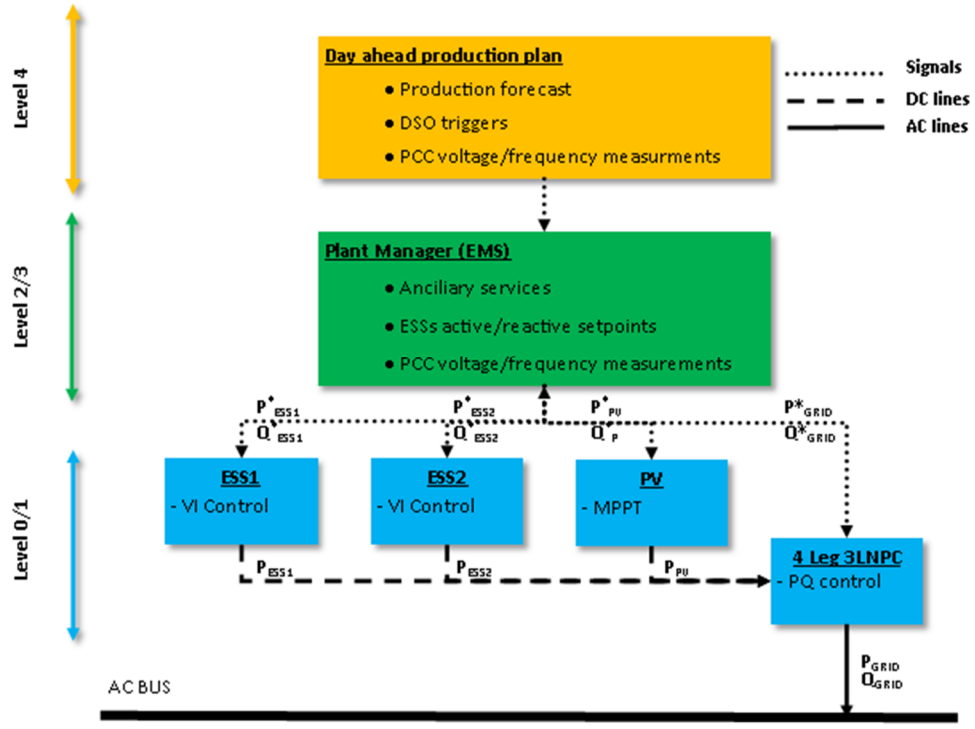

Figure 4.2 Hybrid power plant hierarchical control structure

4.2 HESS Control

The previous section pointed out that a hybrid architecture for hierarchical control is necessary because of the ESSs series connection on the DC bus and the resulting coupling. Thus only one state variable of the two ESSs can be controlled at a time. As detailed in Chapter 2 the HESS studied in this work is composed of one power oriented ESS (Li-Ion) along with an energy-oriented one (VRB). It has also been shown that the VRB power gradient should be kept as low as possible to avoid reduced lifetime and to preserve a high efficiency too. The choice of the controlled ESS is then straightforward and should be the VRB ESS, while the Li-Ion ESS power flow which cannot be controlled directly depends on the AC and DC side set points as described in Chapter 3.

Using appropriated hypothesis of a higher frequency of the modulation compared with the AC fundamental frequency (at least ten times), it comes that the DC and AC side control of the 3L-NPC inverter can be decoupled, and thus can be studied independently. This section details the DC side control design and tuning of two

different control techniques, namely the Second Order Sliding Mode Control (2SMC) and the more classic approach using Proportional Integral (PI) gains, in order to compare the performance of each solution.

For this work, the zero sequence injection in the modulating signals is used to control the power flow of the HESS. This last principle [8] is widely used for neutral point voltage ripple compensation and DC link capacitor voltage balancing in multilevel inverters [9]. The zero-sequence injection method has been adapted to this work, but with a different objective.

4.2.1 Second Order Sliding Mode Control

Sliding Mode Control (SMC) is a non-linear control method using a discontinuous control signal that influences a non-linear system to move along a crossed section of its manifold defined by a function called sliding or switching function. This technique has gained constant interest because of its superior robustness and particularly while the system's model parameters suffer from variations or uncertainties, which makes SMC scheme particularly adapted to the power converter field because of the variable conditions in which it operates. Moreover, SMC offers a high degree of flexibility in its design choices and thus is relatively easy to implement compared with other types of nonlinear controllers.

Although SMC has shown drastic improvement in robustness and stability compared with PI control, a chattering phenomenon may appear because of the switching nature of the control signal which could potentially inject harmonics into the system. Fortunately, increased order of the switching function can avoid the chattering as proposed in [10]. In addition, the convergence and stability analysis of the SMC can be straightforward for simple systems but can be subject to fastidious calculations for more complex systems [11]. This last issue can be overcome using an increased degree in sliding function, like Second Order SMC (2SMC), and the Super Twisting Algorithm (STA) derived from the increased order which insures convergence in finite time [12]. The classic SMC shows increased performance compared with PI controller as pointed out in [11], but the easier design and tuning of a 2SMC scheme as proposed in [13] makes it more attractive.

Considering the aforementioned benefits of the 2SMC using STA, the DC side control of the HESS power electronic interface will use this technique and the design and tuning process proposed in [13]. The tuning method is chosen especially for its similarity with the tuning of the PI controller which then allows a comparison of both techniques on a similar basis.

4.2.1.1 Design of 2SMC scheme

The chosen sliding function is shown in equation (4.21), where $e = i_{vrb\,ref} - i_{vrb}$ and c is a positive constant. The use of an integral part allows a null error in steady state.

$$s = e + c \int e\, dt \tag{4.21}$$

Taking the time derivative of (4.21) and using (3.6) and (3.7), the VRB current dynamics can be expressed as:

$$\frac{ds}{dt} = i_{vrb} + R_{vrb}C_2\left(\frac{d\, i_{vrb\,REF}}{dt} + ce\right) - \sum_{k=a,b,c,n}\left[i_k\left(\frac{A_1 - 1 + d_k^* + Z_s}{A_2}\right)M_k + i_k\right] \tag{4.22}$$

Considering the structure of (4.22), the control law can be expressed as (4.23) where the term with the subscript 'ST' corresponds to the super twisting algorithm (STA) by Levant [10] and is given in (4.24) where λ and w are positive gains to be tuned. The first term of (4.24) is used to guarantee *s=0* is reached in finite time. The subscript 'EQ' corresponds to the equivalent control term obtained by letting $ds/dt = 0$ and is given in (4.25).

$$Z_s = Z_{s\,ST} + Z_{s\,EQ} \tag{4.23}$$

$$Z_{s\,ST} = \lambda\sqrt{|s|}\,sign(s) + w\int sign(s)\;dt \tag{4.24}$$

$$Z_{s\,EQ} = \frac{R_{vrb}C_2\left(\frac{di_{vrb\,ref}}{dt} + c\,e\right) + i_{vrb} - f_1}{f_2} \tag{4.25}$$

$$f_1 = \sum_{k=a,b,c,n} \frac{i_k M_k}{A_2}(A_1 - 1 + d_k^{SVM}) \tag{4.26}$$

$$f_2 = \sum_{k=a,b,c,n} \frac{i_k M_k}{A_2} \tag{4.27}$$

4.2.1.2 Tuning of 2SMC scheme

Substituting the control law of (4.23), (4.24) and (4.25) into (4.22) results in equation (4.28).

$$\frac{ds}{dt} = -\frac{f_1}{R_{vrb}C_2}\left(\lambda\sqrt{|s|}\,sign(s) + w\int sign(s)\;dt\right) \tag{4.28}$$

The f_1 function that appears in (4.28) and is given in (4.26) is hardly expressible as it uses variables from the AC side as well as the zero sequence injection. For the sake of simplicity, it is assumed that the f_1 function is constant and equal to its maximum value $\widehat{f_1}$ on a given set point which is equal to the grid current peak value divided by the DC voltage unbalance index A_2. This assumption will be later discussed in Section IV. Then, taking the time derivative of (4.28) and given that $sign(s) = s/|s|$ it comes to (4.29) :

$$\frac{d^2s}{dt^2} = -\frac{\widehat{f_1}}{R_{vrb}C_2}\left(\frac{\lambda}{2\sqrt{|s|}}\frac{ds}{dt} + w\frac{s}{|s|}\right) \tag{4.29}$$

Assuming the sliding mode is reached, we can consider $|s|<\Delta$, with Δ positive constant close to zero. Considering the worst case $|s|=\Delta$ and using the definition of s in (4.21), the following equation on the error comes to:

Taking the time derivative of (4.30), a third order equation (4.31) of the error

$$\frac{d^2e}{dt^2}+\underbrace{\left(\frac{\widehat{f_1}\,\lambda}{2R_{vrb}C_2\sqrt{\Delta}}+c\right)}_{a_2}\frac{de}{dt}+\underbrace{\frac{\widehat{f_1}}{R_{vrb}C_2\sqrt{\Delta}}\left(\frac{\lambda\,c}{2}+\frac{w}{\sqrt{\Delta}}\right)}_{a_1}e + \underbrace{\frac{\widehat{f_1}\,w\,c}{R_{vrb}C_2\,\Delta}}_{a_0}\int e\,dt=0 \tag{4.30}$$

$$\frac{d^3e}{dt^3}+a_2\frac{d^2e}{dt^2}+a_1\frac{de}{dt}+a_0\;e=0 \tag{4.31}$$

dynamic while the sliding mode is obtained. The error dynamic can then be identified with the third order transfer function defined in (4.32) in order to select appropriate c, λ and w gains. The identification leads to a set of parameters λ, w and several parameters c (4.33). The best parameter for c can be identified later empirically by simulation means.

$$\begin{aligned}T_{fe}&=(p^2+2\xi\omega_n\,p+\omega_n^2)(p+\alpha\xi\,\omega_n)\\&=p^3+\underbrace{(2+\alpha)\,\xi\omega_n}_{a_2}p^2+\underbrace{(1+2\alpha\xi^2)\omega_n^2}_{a_1}p+\underbrace{\alpha\xi\,\omega_n^2}_{a_0}=0\end{aligned} \tag{4.32}$$

$$\begin{aligned}&c=\omega_n\;or\;c=\alpha\omega_n\\&\lambda=\frac{2\,\pi\,R_{vrb}C_2\sqrt{\Delta}\left[(2+\alpha)\xi\omega_n-c\right]}{\widehat{f_1}}\\&w=\frac{R_{vrb}C_2\,\Delta\,\alpha\,\xi\,\omega_n^3}{\widehat{f_1}\,c}\end{aligned} \tag{4.33}$$

Given that $\alpha\omega_n \gg \omega_n$, the transfer function has a dominant pair of pole, typically $\alpha=10$. For a damping ratio $\xi=1$, the natural pulsation, and thus the whole error dynamic, can finally be defined only by the settling time t_s at 2%, as it is expressed by the approximation in (4.34).

$$\omega_n=\frac{5.8}{t_s} \tag{4.34}$$

4.2.1.3 2-SMC tuning validation

As mentioned in Section 4.2.1.1 an assumption is made to design the 2-SMC. The validity of this assumption is tested by simulation means, in the same conditions as in the simulation for limits assessment in Chapter 3 (+). Figure 4.3 presents the results of a step from 25A to 50A (mid to near maximum current) on the VRB current reference compared to the transfer function that has been used to design the error dynamic (4.32). These results show a good agreement between the tuning process and the effective dynamic of the current, particularly for settling time value of 5ms, validating the above-mentioned assumption.

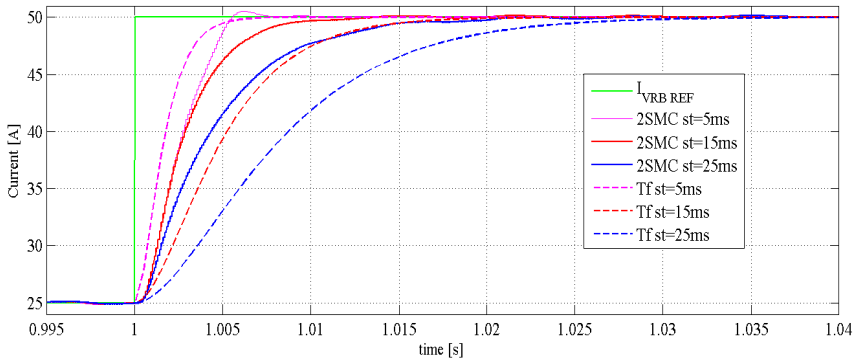

Figure 4.3 2-SMC step response for $\alpha = 10$, $\xi = 1$ and different settling time

4.2.2 PI control

A classic PI scheme is designed in order to compare the dynamic performance of the second-order SMC to control the power flow of the HESS. Taking the basic equation of the system defined in (3.6) and (3.7), and using the functions f_1 and f_2, the differential equation (4.35) is obtained.

$$Z_s f_2 + f_1 = i_{vrb} + R_{vrb} C_2 \frac{di_{vrb}}{dt} \tag{4.35}$$

From this equation, the control of the zero sequence is selected as in (4.36) where the subscript 'FF' can be considered as a disturbance injected in the direct chain as defined in (4.37). The term with the subscript 'PI' corresponds to a classic PI scheme in its parallel form and is defined in the Laplace domain in (4.38).

$$Z_s = \frac{Z_{sPI}}{f_2} + Z_{sFF} \tag{4.36}$$

$$Z_{sFF} = \frac{f_1}{f_2} \tag{4.37}$$

$$Z_{sPI} = K_p + \frac{1}{T_i p} \tag{4.38}$$

Considering the same approximation in the sliding mode control where the max value $\widehat{f_1}$ is taken for (4.35), and injecting the control law (4.36) in (4.35) the transfer function (4.39) is obtained.

$$T_f = \frac{I_{vrb}}{Z_{sPI}} = \frac{\widehat{f_1}}{1 + R_{vrb} C_2 \, p} \tag{4.39}$$

The pole placement technique is then used to get a first-order target error of settling time at 2% τ and lead to the PI gains in (4.40).

$$K_p = \frac{R_{vrb} C_2}{\tau \, \widehat{f_1}} \;\; ; \;\; T_i = \tau \, \widehat{f_1} \tag{4.40}$$

4.2.3 Dynamic performance comparative assessment

Several simulations have been carried out to validate and compare the proposed 2-SMC scheme with a classical PI-based control designed previously. Figure 4.4 shows the results obtained for VRB current reference ramp of 4A/ms from 20A to 60A for the same condition as aforementioned. As can be seen, the 2-SMC scheme shows better tracking ability and DC harmonics reduction compared to the PI controller. The maximum absolute error for the 2-SMC strategy being under 0.5A illustrates the good performance compared to the PI strategy that reaches more than 1A error.

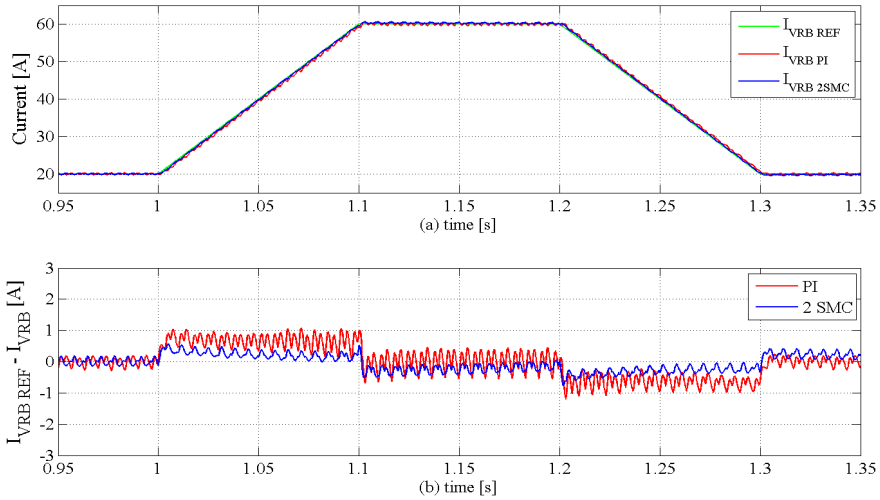

Figure 4.4 Dynamic performance comparison (a) currents (b) errors

4.2.4 Parametric robustness comparative assessment

In order to assess the parametric robustness of the two control schemes, the DC bus link capacitances C_1 and C_2 have been decreased by 50%, while the series resistor of the VRB R_{vrb} has been increased by 50% with both 2-SMC and PI gains kept at their previous settings. These values can be assimilated to a downgraded mode where both VRB and DC link filter have reached the end of their lifetime. In Figure 4.5 the results of a ramp of 4A/ms from 20A to 60A on the VRB current reference are displayed. It can be seen that the dynamics of the error for the 2-SMC is much closer to the performance observed without parametric uncertainties compared to the PI scheme. Also, the PI cannot compensate the current ripples in such configuration and a 3A peak to peak current error can be noticed even with a stationary reference.

It can be concluded from these simulation results that the 2-SMC design and tuning process is suitable both in terms of dynamic performance and robustness.

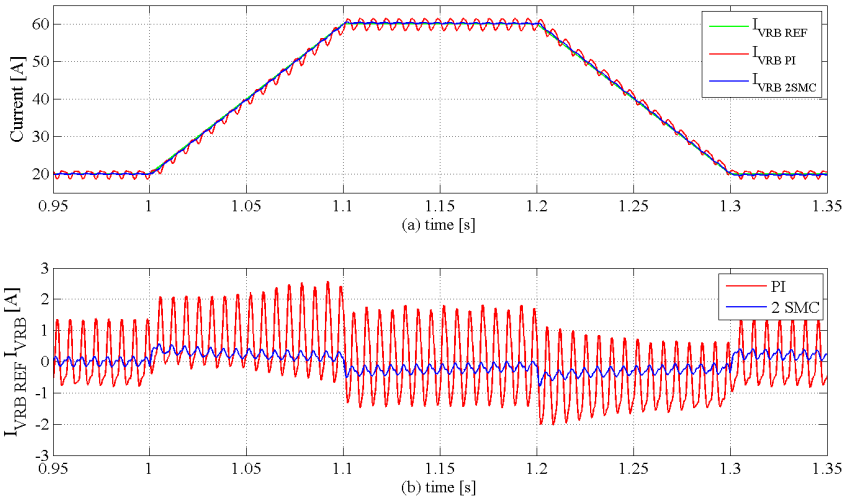

Figure 4.5 Dynamic performance comparison while parametric uncertainties (a) currents, (b) errors

4.2.5 HESS current harmonic reduction

The control algorithm designed for the HESS power flow management is also able to tackle the DC link voltage ripple issue of the NPC topology that involve HESS harmonics. Figure 4.6 presents the HESS currents for different zero sequence injection controls and for the same conditions as the previous simulations. As it can be seen in Figure 4.6, the 2-SMC scheme allows a significant improvement of the current harmonics suppression compared to the PI control. Also, the better results of the VRB harmonic suppression compared to the Li-Ion one are due to the fact that only the VRB current is controlled through zero sequence injection. It could be possible to reduce these harmonics even more using a smaller settling time, but the AC side harmonics would increase as a consequence.

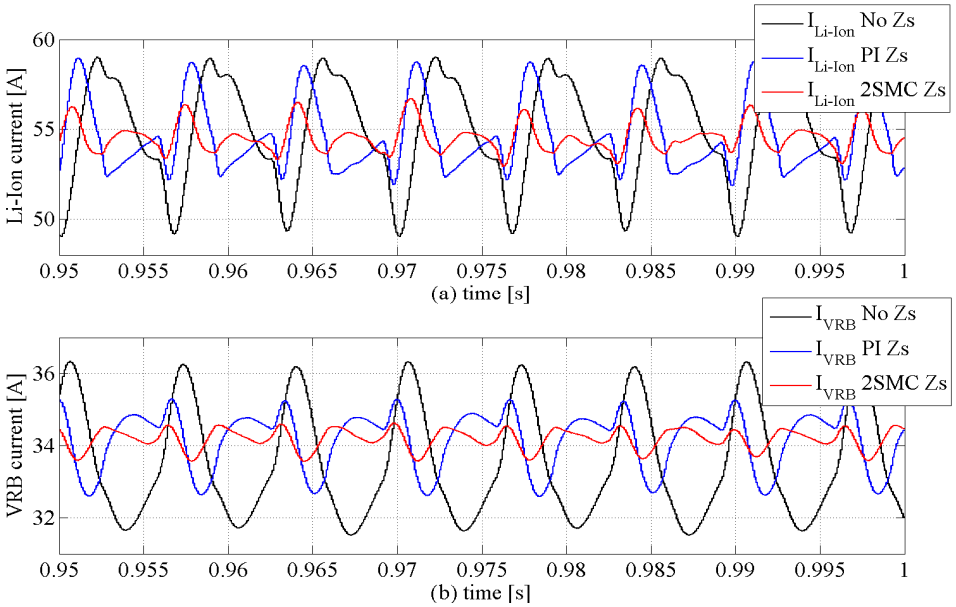

Figure 4.6 a) Li-Ion b) VRB current harmonics for different Zero Sequence injection regulation (black – constant zero sequence, blue – PI regulated zero sequence and red – 2SMC regulated zero sequence)

Zero sequence (Zs)	VRB	Li-Ion
Contant Zs	14.34%	18.2%
PI controlled Zs	7.92%	12.9%
2-SMC controlled Zs	3.08%	6.9%

Table 4.13: DC side current THD under different zero sequence injection

4.3 HESS Management

The ESS management task, in general, relate to the third and/or fourth level of control of hierarchical control architecture, thus the time scale of such control is higher than the previously developed controllers.

The HESS management consists of using each ESS depending on several objectives. There are as many management techniques as storage technologies exist. Indeed having several storage technologies enables another degree of freedom which can be used in a different way. But as mentioned in Chapter 3 the HESS is not fully controllable in the 3LNPC configuration, so only one ESS can be controlled at the time which complicates and restricts the management technique that can be used.

Moreover, the 3LNPC topology has shown energy exchange possibilities among the HESS depending on the power flow set point, but this is limited according to the model developed in Chapter 3. Thus the choice for HESS management strategy is limited and several identified possibilities will be described in the next sections.

4.3.1 Frequency separation management

A common strategy to manage a HESS composed of several ESS technologies is to adjust the power flow gradient of each one according to the specification. This strategy is commonly used when both ESS technologies have far apart settling time or when the application requires large power gradients [14], [15]. The principle lies in the control of the power electronic interface of each ESSs to match the settling time of its ESS. This strategy is particularly relevant for a HESS composed of a fast and a slow response time ESS which allows the reduction of stress applied and thus extends lifetime.

In this work, the frequency separation strategy will be used to manage the HESS. The VRB technology presents a slow settling time compared to the Li-Ion one as it has been described in Chapter 2, and is particularly suited for this application. Also, the VRB settling time is directly linked to the electrolyte flow and it is thus possible to reduce the flow according to the power electronic interface settling time which allows control of the losses caused by the pumps.

4.3.2 Energy/Power ESS SOC balancing

When the HESS is realised with different technologies in a way that one ESS provides the energy while the other one the power, the SoC of one of the ESS can be balanced in order to provide the necessary power or energy reserve to fulfil ancillary services. For the VRB/Li-Ion HESS, an energy balancing management would control the VRB power set point in order to reach a given SoC. Depending on the targeted SoC, the reserve could either supply or absorb energy. If set to 50% the energy reserve is equal both in supply or absorb mode. This mode would be suited for capacity firming (section 2.3.1) and peak shaving (section 2.3.4) services.

In the same way, for power balancing the SoC of the Li-Ion ESS will be controlled to enable power reserve. This mode would enable the active power reserve necessary for frequency regulation service (section 2.3.2).

4.3.3 Optimal strategies

Optimal control strategies are commonly used for higher level purposes but are particularly suited for HESS management applications. Indeed hybrid systems can be classified as Multi Input Multi Output (MIMO) in opposition to Single Input Single Output (SISO) systems. These systems can be managed using optimal or predictive control strategies. These strategies include Model Predictive Control (MPC), Linear Quadratic Regulator (LQR), Particle Swarm Optimisation (PSO), Linear Programing (LP). These strategies use a cost function selected according to the control objective that is either minimised or maximised. The main control objectives include operating cost minimisation and lifetime maximisation [16]–[22].

4.4 AC side model and control

Power converters offer a large panel of functionalities which makes the AC side control of such a device an active research topic. Power quality issues like voltage regulation or harmonic mitigation, and stability issues while unbalanced grid conditions and for inertia emulation are particularly discussed in the literature. To address these issues a wide range of control technique are proposed, each of them present drawbacks and advantages. The main control found are PI controller along with Proportional Resonant (PR), sliding mode controllers and Model Predictive Controllers (MPC). Although the last controllers give more robust and performant responses, unbalanced grid conditions require an additional calculation for the grid-connected mode which complicates the controller design and tuning.

Therefore the Fortescue transform is used to decompose the three-phase signal into positive, negative and zero sequences in this thesis. A sequence-independent control approach is developed using PI controllers for both islanded and grid-connected mode. First of all, the symmetric component calculation and the model used for islanded and connected mode are established. Then a discussion on three

different methods to realize effective symmetric component decomposition of voltage and current measurement is proposed. Finally, the grid side control design and tuning methods proposed are detailed for both islanded and connected mode, and transition between these modes will be discussed.

4.4.1 Symmetric component sequence decomposition

Unbalanced grid voltages represent one of the most challenging issues for small to medium size DG integration, especially in weak LV and MV distribution grids where the impact of RES injection exacerbate fluctuation of the grid's parameters. In such conditions, several methods have been developed to control power converters. Analytical methods where the whole system is described are proven to lead to better performance and robustness [23], as has been shown for the DC side power flow controller, but more complex systems where several stages stacked present couplings and complex equations end up in hazardous calculations. Thus an empirical method inspired from well know technique using PI controllers that, although are not optimal, have proven to be efficient and benefit as well from wide use in both academic research and industrial devices. Thus the selected solution to analyse and realise the AC side control of the multipurpose power converter in a poor power quality environment will use the Fortescue transform to decompose the three-phase signal in the positive, negative and homopolar sequences. Having the symmetrical components ease the system analysis and thus enable implementation of classic control techniques like PI scheme.

To be able to use the linear controller like PI gains, it is necessary that the controlled variables are constant in steady state. In a balanced three-phase system, the classic approach consists of using Clark (4.46) and Park (4.47) transforms to switch the current and voltage sinusoidal signals in *abc* coordinates into constant values in a steady state *dq0* reference frame. But if the voltages or currents show unbalances, these variables in *dq0* frame won't be constant anymore, and PI controller tuning becomes difficult or even impossible.

Thus the use of the Fortescue transform expressed in (4.42) allows three representative sequences to be achieved, each of them, apart from the homopolar one, being balanced which allows use of the PI controller in the *dq0* reference frame. This approach has been initially developed in [24] in which the author proposes modification of homopolar matrix transform in order to obtain a three-phase balance signal for the zero sequence too, like the positive and negative ones. This modified homopolar transform matrix given in (4.43) realises simply a $2\pi/3$ phase shift on the second and third line to realise a three-phase balance system. This technique has shown good results in both simulation and experiment on an islanded two-level inverter and resistive loads. In this thesis, this method will be further developed and adapted to a three-level inverter both in islanded and connected mode.

$$\overline{F_+} = \begin{bmatrix} 1 & a & a^2 \\ a^2 & 1 & a \\ a & a^2 & 1 \end{bmatrix} \overline{F_-} = \begin{bmatrix} 1 & a^2 & a \\ a & 1 & a^2 \\ a^2 & a & 1 \end{bmatrix} \overline{F_0} = \begin{bmatrix} 1 & 1 & 1 \\ 1 & 1 & 1 \\ 1 & 1 & 1 \end{bmatrix} \tag{4.42}$$

$$\overline{F^{0*}} = \begin{bmatrix} 1 & 1 & 1 \\ a & a & a \\ a^2 & a^2 & a^2 \end{bmatrix} \text{ with } a = e^{i\frac{2}{3}\pi} \tag{4.43}$$

$$\begin{cases} \overline{V_{abc}^{+}} = \overline{F^{+}}.V_{abc} \\ \overline{V_{abc}^{-}} = \overline{F^{-}}.V_{abc} \\ \overline{V_{abc}^{0}} = \overline{F^{0*}}.V_{abc} \end{cases} \quad \begin{cases} \overline{I_{abc}^{+}} = \overline{F^{+}}.I_{abc} \\ \overline{I_{abc}^{-}} = \overline{F^{-}}.I_{abc} \\ \overline{I_{abc}^{0}} = \overline{F^{0*}}.I_{abc} \end{cases}$$

To be able to apply the Fortescue transforms of (4.42) and (4.43) which are expressed in complex space to the voltage and current measurements, these last signals have to be converted in complex values. This issue is not trivial and represents in fact a key problem in digital control. Thus several ways to effectively decompose a three-phase signal into its symmetrical components are explored and compared in the following sections.

Finally, to represent the unbalance magnitude of a three-phase system, the Voltage Unbalance Factor (VUF) and the Current Unbalanced Factor (CUF), which is the

ratio of the positive sequence over the negative one, are good indexes and are given in (4.44). An unbalance factor of 100% indicates that two lines on the three-phase system have a null voltage, the same for the current. This index will be used as a power quality indicator in the next chapter to observe the PCC's health.

$$VUF = \frac{\left|\overline{V_{abc}^{-}}\right|}{\left|\overline{V_{abc}^{+}}\right|} \; ; \; CUF = \frac{\left|\overline{I_{abc}^{-}}\right|}{\left|\overline{I_{abc}^{+}}\right|} \tag{4.44}$$

The controller maintains a voltage balanced at the PCC naturally, but the line current will depend heavily on the load and lines parameters. The grid impedance was considered equal on every line even on the neutral line in the previous section. It should be noted that in practice the neutral line could present a different impedance compared with the other lines and thus it should be taken into account in further developments.

4.4.2 Islanded mode modelling

The islanded mode occurs when the controlled power converter is either the only source in the local network, or when other DGs on the network supply a negligible power compared to the controlled power converter. The schematic of the islanded mode, considering the averaged model of a two-level inverter approximation instead of the 4 Leg 3LNPC one following the assumptions developed in Chapter 3, is given in Figure 4.7.

The equations resulting from the AC side connection in isolated mode can be obtained using Kirchhoff's laws and are given in (4.45) and (4.46). It can be seen that the load impedance parameters do not appear in these equations and only the filter parameters which justify taking into account the small resistor of the inductive filter.

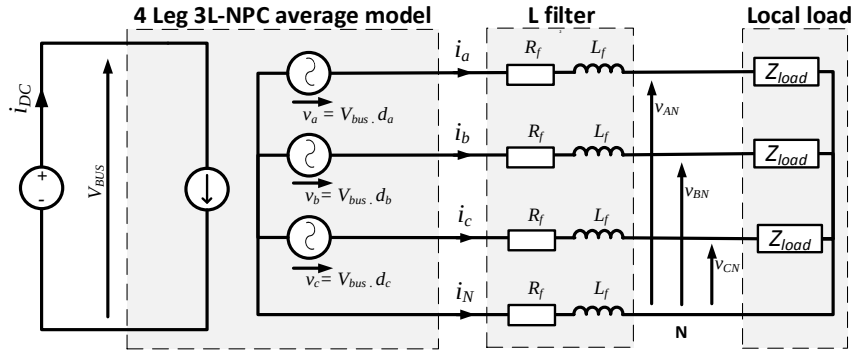

Figure 4.7 3LNPC power converter averaged model in islanded mode

$$\begin{bmatrix} v_a \\ v_b \\ v_c \end{bmatrix} = \begin{bmatrix} v_{AN} \\ v_{AB} \\ v_{AC} \end{bmatrix} + R_f \begin{bmatrix} i_a \\ i_b \\ i_c \end{bmatrix} + L_f \frac{d}{dt} \begin{bmatrix} i_a \\ i_b \\ i_c \end{bmatrix} - R_N \begin{bmatrix} i_n \\ i_n \\ i_n \end{bmatrix} - L_N \frac{d}{dt} \begin{bmatrix} i_n \\ i_n \\ i_n \end{bmatrix} \tag{4.45}$$

$$i_a + i_b + i_c + i_N = 0 \tag{4.46}$$

The control technique selected and developed later on will use linear controllers which require a coordinate transformation into the bi-phase system in $\alpha\beta 0$ frame using Clark transforms (4.46), and then to the rotating *dq0* rotating frame through Park transforms (4.47). Applying the previous Clark and Park transforms to (4.45) and using the derivative properties of these transforms, the equation on the inverter's voltage in *dq0* reference frame can be derived and is given in (4.49).

$$T_{\alpha\beta 0} = \frac{2}{3} \begin{bmatrix} 1 & -\frac{1}{2} & -\frac{1}{2} \\ 0 & \frac{\sqrt{3}}{2} & -\frac{\sqrt{3}}{2} \\ \frac{1}{2} & \frac{1}{2} & \frac{1}{2} \end{bmatrix} \quad T_{\alpha\beta 0}^{-1} = \frac{2}{3} \begin{bmatrix} 1 & 0 & 1 \\ -\frac{1}{2} & \frac{\sqrt{3}}{2} & 1 \\ -\frac{1}{2} & -\frac{\sqrt{3}}{2} & 1 \end{bmatrix} \tag{4.46}$$

$$T_{dq0} = \begin{bmatrix} cos(\omega t) & sin(\omega t) & 0 \\ -sin(\omega t) & cos(\omega t) & 0 \\ 1 & 1 & 1 \end{bmatrix} \quad T_{dq0}^{-1} = \begin{bmatrix} cos(\omega t) & sin(-\omega t) & 0 \\ sin(\omega t) & cos(\omega t) & 0 \\ 1 & 1 & 1 \end{bmatrix} \tag{4.47}$$

$$\begin{bmatrix} v_d \\ v_q \\ v_0 \end{bmatrix} = \begin{bmatrix} v_d \\ v_q \\ v_0 \end{bmatrix} + R_f \begin{bmatrix} i_d \\ i_q \\ i_0 \end{bmatrix} + L_f \frac{d}{dt} \begin{bmatrix} i_d \\ i_q \\ i_0 \end{bmatrix} + L_f \omega \begin{bmatrix} -i_q \\ i_d \\ 0 \end{bmatrix} - R_N \begin{bmatrix} 0 \\ 0 \\ -3i_0 \end{bmatrix} - L_N \frac{d}{dt} \begin{bmatrix} 0 \\ 0 \\ -3i_0 \end{bmatrix} \quad (4.49)$$

4.4.3 Connected mode modelling

The connected mode will be modelled according to the electrical diagram of Figure 4.8. The inverter is considered connected transformerless to the LV of a distribution network where the grid is modelled as an ideal voltage source in series with a line impedance Z_{grid} [25]. The weak grid context imposes that the MG impedance cannot be neglected, and its values depend on many parameters, some of them being distributed. The MG impedance is thus considered inductive with a high resistive value, like most distribution networks. The amplitude and frequency of the ideal voltage sources will also be considered variable, but the voltage and frequency response models of the system will be described in the next chapter.

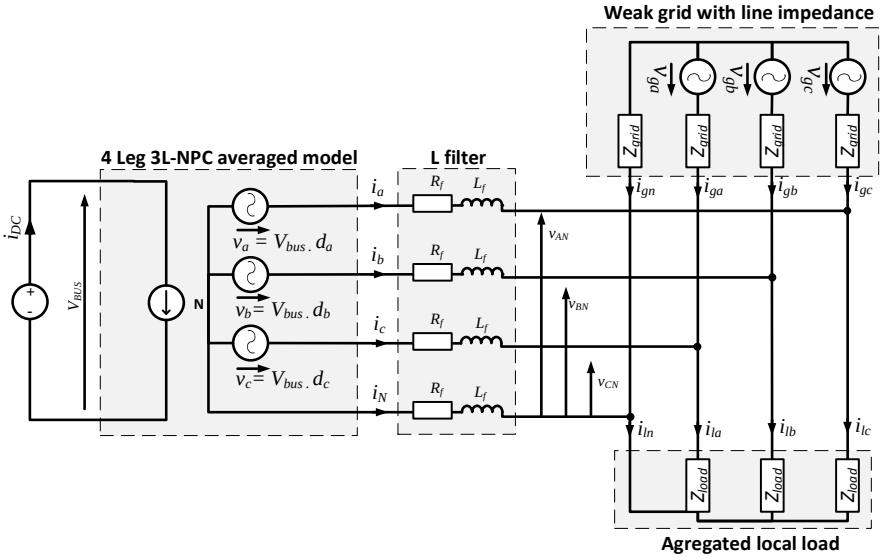

Figure 4.8 3LNPC power converter averaged model in connected mode

Kirchhoff's law applied to the circuit in connected mode leads to similar equations obtained in (4.45) and is given in (4.50) with an additional equation that links the inverter's currents to the load and grid ones (4.51).

$$V_i = V_g + R_f I_i + L_f \frac{dI_i}{dt} + R_f I_{in} + L_f \frac{dI_{in}}{dt} - R_g I_g - L_g \frac{dI_g}{dt} - R_g I_{gn} - L_g \frac{dI_{gn}}{dt} \tag{4.50}$$

$$i_a + i_b + i_c = i_n \tag{4.51}$$

with $V_x = \begin{bmatrix} v_{xa} \\ v_{xb} \\ v_{xc} \end{bmatrix}$; $I_x = \begin{bmatrix} i_{xa} \\ i_{xb} \\ i_{xc} \end{bmatrix}$; $V_{xn} = \begin{bmatrix} v_{xn} \\ v_{xn} \\ v_{xn} \end{bmatrix}$; $I_{xn} = \begin{bmatrix} i_{xn} \\ i_{xn} \\ i_{xn} \end{bmatrix}$ and $x = a, b, c$

Applying the Clark and Park transforms in (4.46), (4.47) and using the matrix derivation property on (4.50), and arranging it using (4.51) gives the model of the inverter connected to the MG in the *dq0* frame in (4.52). The *0* axis projection corresponds to the zero sequence.

$$\begin{bmatrix} v_{id} \\ v_{iq} \\ v_{i0} \end{bmatrix} = \begin{bmatrix} v_{gd} \\ v_{gq} \\ v_{g0} \end{bmatrix} + (R_f + R_g) \begin{bmatrix} i_{id} \\ i_{iq} \\ i_{i0} \end{bmatrix} + (L_f + L_g) \frac{d}{dt} \begin{bmatrix} i_d \\ i_q \\ i_0 \end{bmatrix} + (L_f + L_g)\omega \begin{bmatrix} -i_q \\ i_d \\ 0 \end{bmatrix} - (R_f + R_g) \begin{bmatrix} 0 \\ 0 \\ -3i_0 \end{bmatrix} - (L_f + L_g) \frac{d}{dt} \begin{bmatrix} 0 \\ 0 \\ -3i_0 \end{bmatrix} \tag{4.52}$$

4.4.3.1 Delay-based sequence decomposition

The easiest way to build a complex signal from a discrete measurement input is to apply a pure delay to the signal and multiply it with the complex operator while summing it to the original signal. The delay length is set according to the pulsation of the signal to obtain a 90° shift. This technique has been successfully implemented in [24] with a 5ms delay which corresponds to ¼ of a period at 50Hz. Figure 4.9 shows the block representation of this method and (4.46) its mathematical representation in the Laplace domain where z is considered as the complex value of the input signal x. Although this implementation is a quick and easy way to obtain a complex representation of a sampled input signal, the transient behaviour of this solution gives poor accuracy because of the pure delay induced on the complex part of the output value.

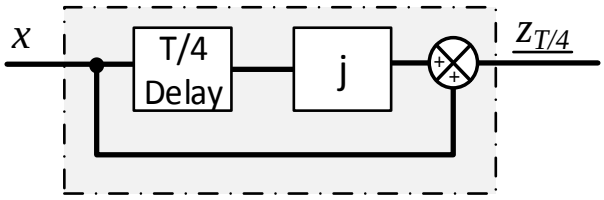

Figure 4.9 ¼ period discrete measurement to complex signal

$$\underline{z_{T/4}} = x\left(1 + e^{-\tau p}\, e^{j\frac{\pi}{2}}\right) \text{; with } \tau = \frac{T}{4} = 5\,ms \tag{4.53}$$

To reduce the effect of this delay on the transfer function, two improvements can be made. The first one could be to take into account this delay in the control loop tuning process, but because the pure delay is added only on the complex part of the newly built complex measurement, classic approaches to deal with a delay in a control loop do not apply. The other identified solution would be to reduce this delay as much as possible and then modify the complex signal calculation to reduce the impact of the delay on the closed loop transfer function.

To reduce this delay, the method retained has been to reduce the delay by half iteratively and use trigonometric relation to obtain the equivalent complex value. The expression of the complex value $\underline{z_{T/8}}$ and $\underline{z_{T/16}}$ of the input signal x is given in (4.54) (4.55), where $e^{-\tau p}$ is a pure delay of time τ expressed in the Laplace domain.

$$\underline{z_{T/8}} = \frac{x}{sin\frac{\pi}{4}}\left(e^{-j\frac{\pi}{4}} + e^{-\tau p}\, e^{j\frac{\pi}{2}}\right) \text{; with } \tau = \frac{T}{8} = 2.5\,ms \tag{4.54}$$

$$\underline{z_{T/16}} = \frac{x}{sin\frac{\pi}{8}}\left(e^{-j\frac{3\pi}{8}} + e^{-\tau p}\, e^{j\frac{\pi}{2}}\right) \text{; with } \tau = \frac{T}{16} = 1.25\,ms \tag{4.55}$$

To assess the rightness of the time delay reduction, the previous equations have been implemented as shown in the block diagram of Figure 4.10. Figure 4.11 shows the result of a simulation where the input signal x_{abc} is a three-phase signal of amplitude equal to 100 and 50 Hz frequency which at t=21ms the line *c* amplitude is reduced by 90%. Although the response time is reduced according to the theory, it can be seen that the lower the delay is, the higher the maximum value reached.

This effect is clearly noticeable at initialisation and can be quantified by the gaps when the convergence occurs. This effect could have a potentially counterproductive effect on the control scheme. Finally, it should be noted that there is use of a lower delay imply to reduce the time step in order to ensure enough precision and avoid ringing phenomenon.

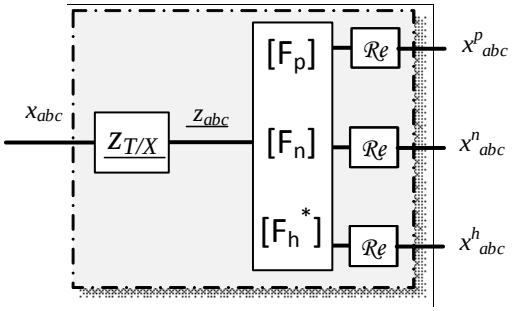

Figure 4.10 Block diagram of the delay based sequence decomposition algorithm

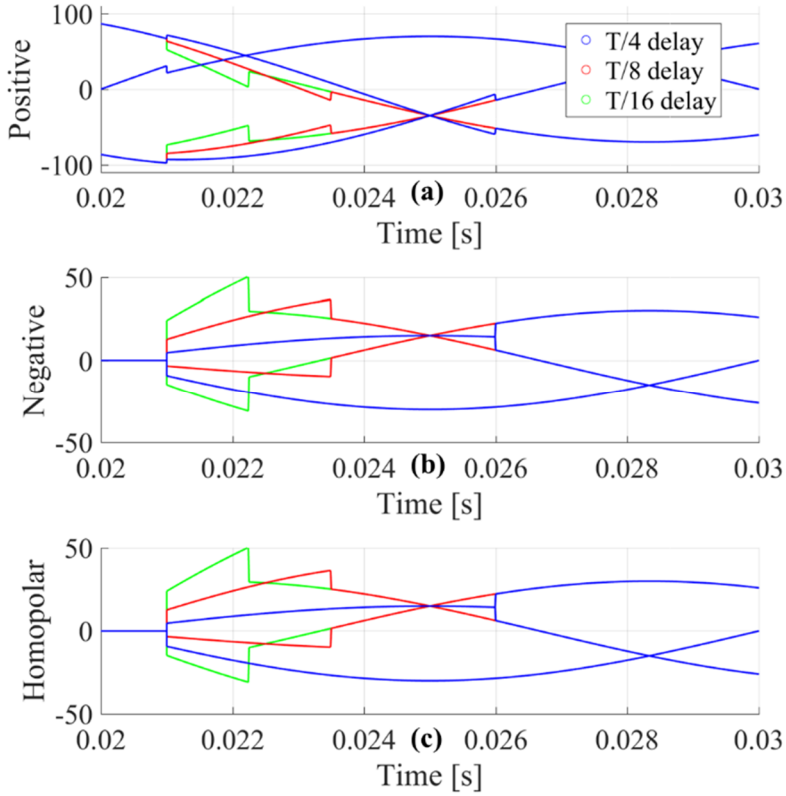

Figure 4.11 Sequence decomposition using several delays (positive (a); negative (d) and zero sequence (b) sequence)

4.4.3.2 Fourier based sequence decomposition

Another method to get the symmetric components is to obtain the polar values of the measurement. The Phase Lock Loop (PLL) algorithm can be used for this and to build the complex value of the input signal with its amplitude and angle. There are several kind of PLL types but the most common implementation uses Fourier transform to output the fundamental frequency polar values. Then the Fortescue transform can be applied to obtain each sequences values.

Unfortunately, classic PLL approaches on their own struggle to deal with strongly unbalanced signals and, more importantly, with DC components in the input signal [26]. Thus a specific design has been developed for this purpose as shown in the block diagram of Figure 4.12.

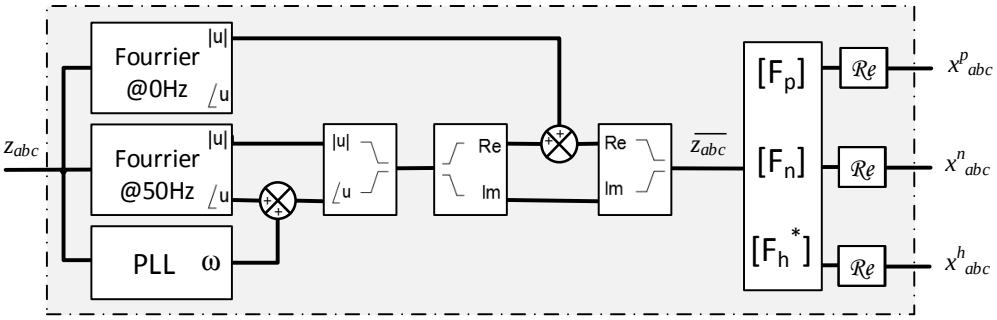

Figure 4.12 Fourier modified sequence decomposition block diagram

To test the ability of effectively realise sequence decomposition, a simulation has been run with the aforementioned algorithm, in the same condition as in the previous section (i.e. 50Hz, 100 amplitude three-phase sinusoidal signal with a 90% unbalance at 41ms). The Fourier method will be compared with the T/8 delay one as a reference. Figure 4.13 shows the result of this simulation. It is clear that the Fourier method presents less brutal variations than the delay based one. But because of the implementation of the Fourier algorithm, the convergence time of such method is a full period (i.e. 20ms) which is a long time. On the other hand, the transfer function of this algorithm can be approximated as a first order low pass filter which is not possible to do with the delay based method. This could

ease the tuning of the controller and enable fine adjustment of the performance in a closed loop.

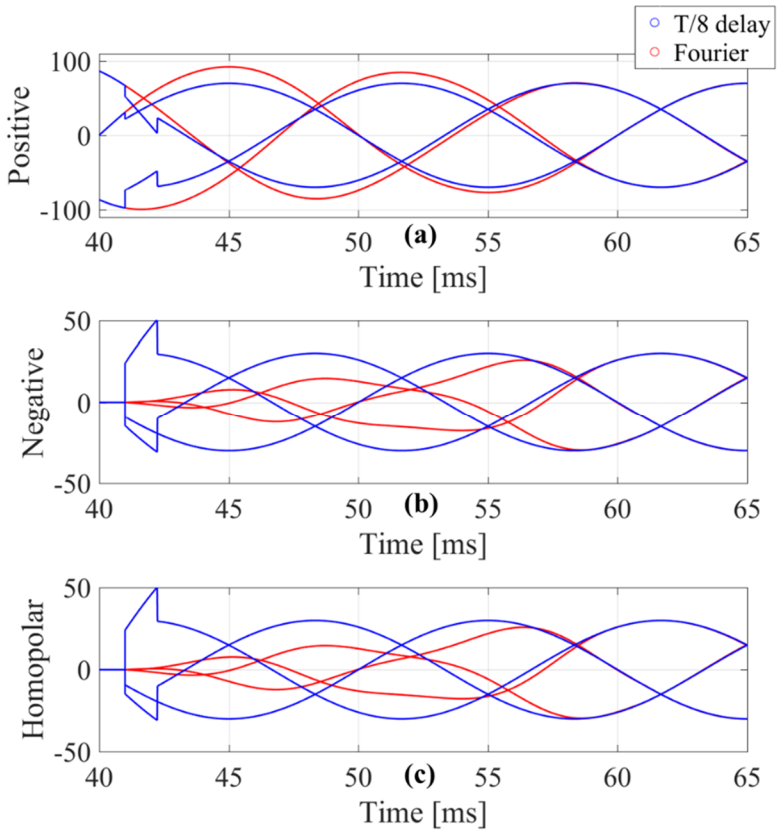

Figure 4.13 Comparison of sequence decomposition using delay and Fourier methods (positive (a), negative (b) and homopolar (c) sequence)

4.4.3.3 Dual Second Order Generalised Integrator Frequency Locked Loop sequence decomposition

As seen in the previous section, a classic PLL approach using Fourier has the advantage of being easily modelled which could ease the tuning process. On the other hand, the response time of this algorithm is quite slow compared with the delay method. To keep in line with the Fourier method which uses PLL, an improvement could be made using Frequency Locked Loop (FLL) algorithm. These have a proven increased ability to deal with unbalanced grids and even with signals with a homopolar component.

FLL algorithms are generally similar to PLLs and are composed of a regulation loop that tracks either the angle or the frequency. But FLLs often do not involve trigonometric calculations and thus are often simpler and more flexible. This enabled the development of an improved class of FLL algorithm of which the Dual Second Order Generalised Integrator (DSOGI) developed in [26] belongs to.

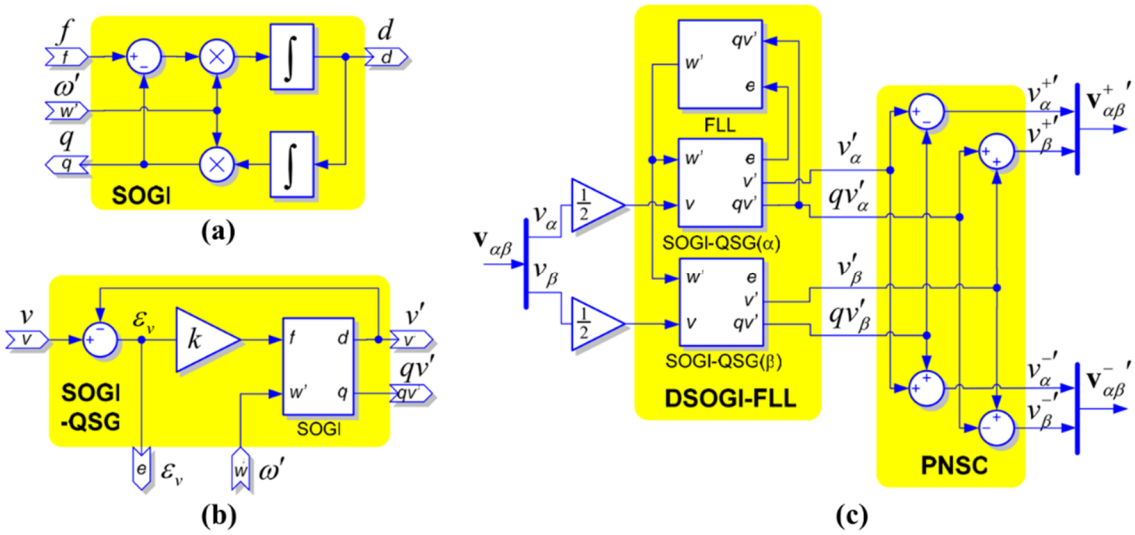

Figure 4.14 DSOGI-FLL block diagram, (a) Second Order Generalized Integrator (SOGI), (b) Quadrature Signal Generator (QSG), (c) DSOGI-FLL) [26]

The DSOGI-FLL has the advantage of being relatively simple to implement as shown in the block diagram of Figure 4.14. It operates in the $\alpha\beta 0$ frame and allows efficient tracing of the positive and negative sequences using only a simple and easy to tune PI controller. The 90° lag operator $q = e^{-\frac{j\pi}{2}}$ is then used to calculate the positive and negative sequence.

Although the positive and negative sequences can be obtained easily and accurately, this method does not offer a straightforward way to get the homopolar sequence as well. The performance of this method can still be assessed and compared to the previous ones for the positive and negative sequence only, the homopolar sequence could be obtained using one of the previous methods.

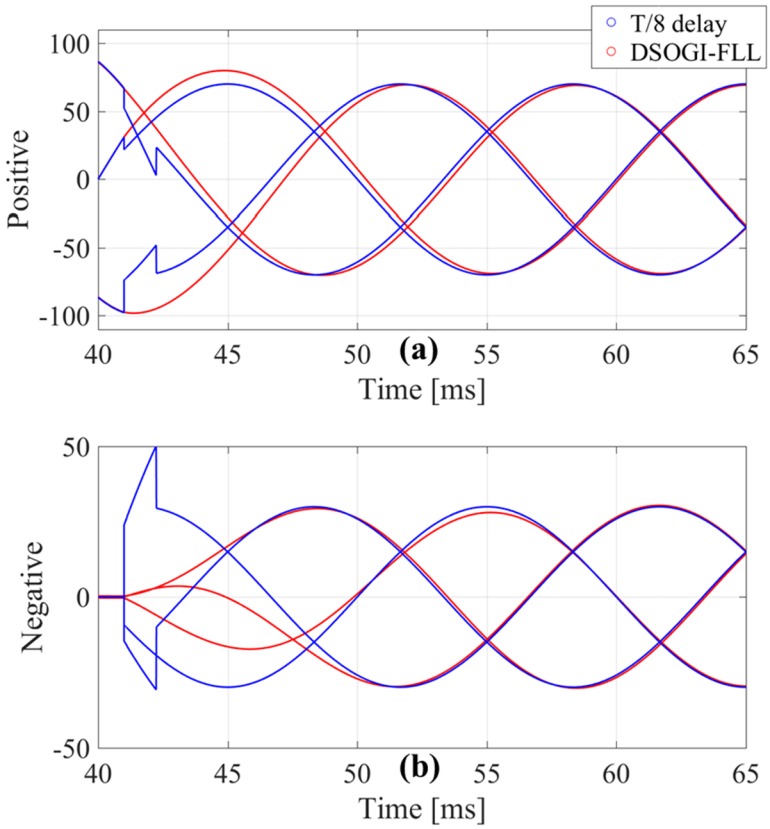

Figure 4.15 Comparison of sequence decomposition using delay and DSOGI-FLL methods (positive (a) and negative (b) sequence)

The DSOGI-FLL has been tested in the same conditions as previously (i.e. 50Hz, 100 amplitude three-phase sinusoidal signal with a 90% unbalance at 41ms). The result of this simulation in Figure 4.15 shows a response time at 5% of approximately 7ms which is an intermediate result compared to the delay based and Fourier methods. Although the response of the DSOGI does not present any overshoot unlike the delay based method, it can be seen that the FLL involves a transitory phase shift. This phase shift is of 5.04° (0.28ms lag) 10ms after the unbalance event. To balance this issue it should be noted that the event applied (a 90% amplitude sudden drop on a line) is an extreme case that is used for testing purpose only, and does not take into account the capacitance and the inductive effect that would moderate such events.

4.4.3.4 Comparison of the sequence decomposition methods in *dq0* frame

In order to compare the three different sequence decomposition methods previously developed, a simulation has been carried out with various events and grid conditions. To be able to compare the results, and also because this extra step will be required by the control architecture, each three-phase sequence signals in *abc* coordinates will be converted to *dq0* reference frame, using successively Clark and Park transforms as aforementioned. Moreover, because the sequence decomposition results in three sequences and each of them are balanced, only the *dq* axis of the *dq0* reference frame will be observed. The standard PLL proposed by Matlab/Simulink with its original settings will be used for angle detection and dq0 transform calculations.

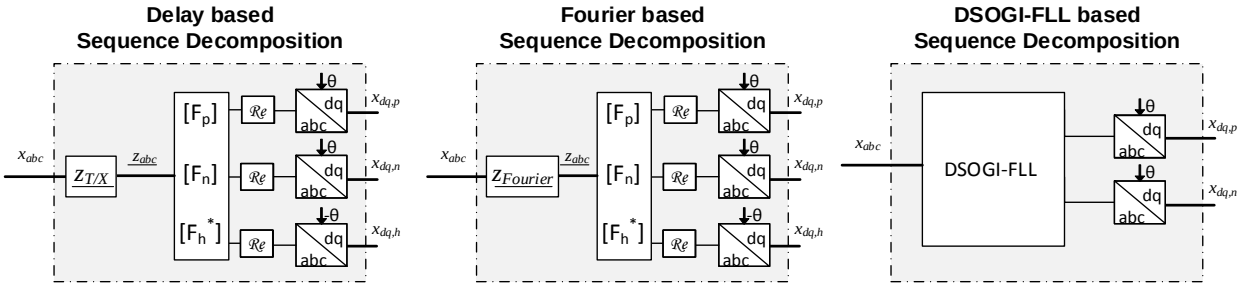

Figure 4.16 Block diagram of sequence decomposition methods in *dq0* frame (1/8 period delay (a) Fourier (b) and DSOGI-FLL (c))

To assess these three different methods, strong events yet realistic from a practical point of view will be applied on the input signal. These events will overcome the classic standards for power quality admitted on continental grid code described in Chapter 2. Indeed, in a weak grid such as a MG or an island grid, reduced stability leads to more volatile power quality indicators. Thus the events applied can be qualified as drastic events but allow the advantages and inconvenience of each sequence decomposition methods to be stressed.

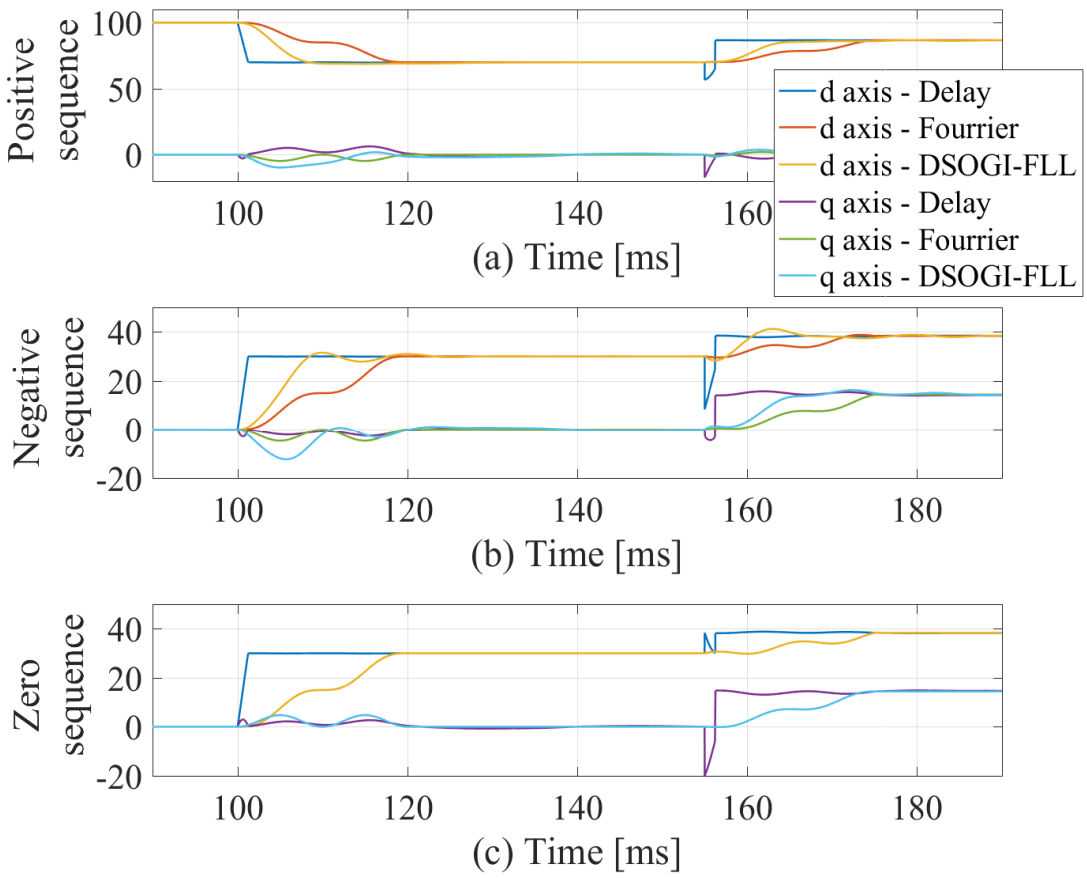

Figure 4.17 Comparison of 1/16 period delay, Fourier and DSOGI-FLL sequence decomposition methods after Clarke and Park transform (a) positive (b) negative (c) zero sequence

Unfortunately, the Fourier based and DSOGI FLL based sequence decomposition did not allow a stable implementation in simulations, and even more in experimentations. Thus the delay based method will be used in this work to realise the sequence decomposition of voltage and current measurements. The selected delay is $1/16^{\text{th}}$ of a period which is equal to 1.25ms for a 50Hz grid frequency. Even though this delay causes higher transitory mismatch, reducing it as much as possible enables classic control strategies without the need for predictors or other means to deal with the delay in the system.

4.4.4 Grid forming and islanded mode control

Following the different mode detailed in Chapter 3 in which the converter can operate, the grid forming mode is made of a controller that sets both the angle and the amplitude of voltages or currents in the case of a VSI CSI respectively. In this thesis the network will be considered as weak, unbalanced and made of nonlinear loads, thus the converter will be considered as a voltage source and the control architecture as a VSI.

In such conditions, the control objectives are to set and maintain the voltage of each line to the desired reference and to maintain balanced voltages on the PCC, whatever the load. The controller has to maintain a low voltage THD even with nonlinear loads. Finally, the voltage and phase angle has to be maintained close to its reference even when a large transitory event occurs (i.e. connection or disconnection of a large load).

To reach these specifications, and as mentioned previously, a sequence decomposition based controller is developed. This controller is inspired by the one developed in [24] in which once the voltage and current signals are decomposed in positive, negative and zero sequences and converted in *dq0* reference frame, each sequence is controlled by a dedicated double loop PI structure on both d and q axis. The block diagram of this control structure is illustrated in detail in Figure 4.18. The particularity of this structure is to control each sequence independently. In grid forming mode, voltage set points $v^*_{qp,}$ $v^*_{dn,}$ $v^*_{qn,}$ v^*_{dh} and v^*_{qh} are set to zero to cancel both voltage unbalances and zero sequence components, and the direct sequence voltage reference v^*_{dp} sets the voltage amplitude to be the same for every line, whatever the inverter's individual line currents which depend on the load conditions.

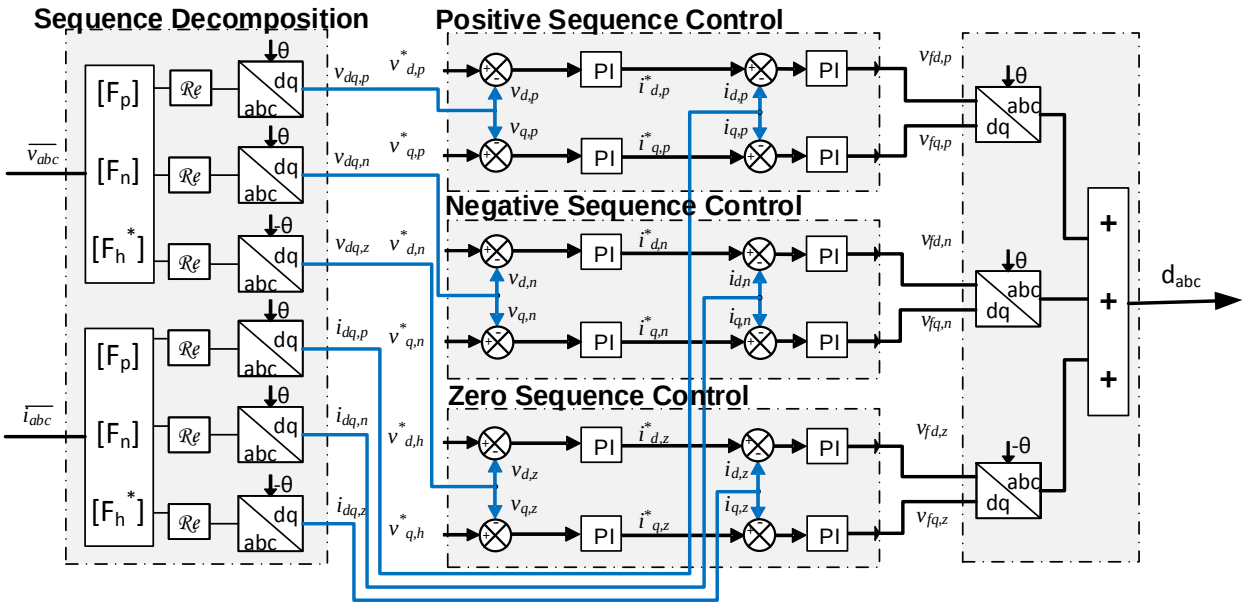

Figure 4.18 Grid forming mode control structure

The tuning of each PI controller requires details of the transfer functions of each sequence. This can be found out using the sequence decomposition matrixes of (4.42), (4.43) and the model of the inverter in (4.45), (4.46).

4.4.5 Grid feeding and P/Q Controller

In grid feeding mode the power converter is now supplying or absorbing energy by the means of a three phase four wire connection to a LV network. This grid will be considered as a weak network with poor power quality. Therefore the concept of active and reactive power while unbalances or harmonics has to be discussed. The expression of the instantaneous active and reactive power p and q supplied/absorbed by the inverter can be expressed as in (4.56) and (4.57) using voltages and currents the *dq0* reference frame. While unbalances or high harmonics components in the three-phase signal, these active and reactive power as computed using (4.56) and (4.57) will be composed of several high amplitude harmonics [27]. These active and reactive power signals do not allow the design of a control using a linear controller. Thus the active and reactive power in unbalanced systems and the solution to express these quantities have to be discussed.

The concept of instantaneous active and reactive power in the unbalanced system with harmonics is rather controversial in the literature and several ways to express these quantities have been proposed [28], [29]. The positive sequence active, reactive and apparent power terminology is however accepted and used in the literature. As a consequence, the computation of these variables can be realized using symmetric components. Thus using the sequence independent control previously developed, the instantaneous positive sequence active and reactive power p^+ and q^+ will be controlled, according to the PQ theory.

The positive sequence currents reference signals will be computed by deriving (4.56) and (4.57) with transforms (4.42) to obtain equations in (4.58) and (4.59). In addition, the negative and zero sequence voltage set points are kept to zero like in the islanded mode in order to cancel voltage unbalances and zero sequence components at the PCC. As a consequence, the injection of active and reactive power on the positive sequence only positively affect the dynamic at the PCC thanks to the absence of parasitic active and reactive power on the negative and zero sequence on the one hand, and participation in the voltage balancing process on the other hand.

$$p = 3/2(v_d i_d + v_q i_q) \tag{4.56}$$

$$q = 3/2(v_d i_q - v_q i_d) \tag{4.57}$$

$$p_p = 3/2(v_{dp} i_{dp} + v_{qp} i_{qp}) \tag{4.58}$$

$$q_p = 3/2(v_{dp} i_{qp} - v_{qp} i_{dp}) \tag{4.59}$$

$$i_{dp}^* = \frac{\frac{2\,p_p^*}{3} - v_{qp} i_{qp}}{v_{dp}} \tag{4.60}$$

$$i_{qp}^* = \frac{\frac{2\,q_p^*}{3} + v_{qp} i_{dp}}{v_{dp}} \tag{4.61}$$

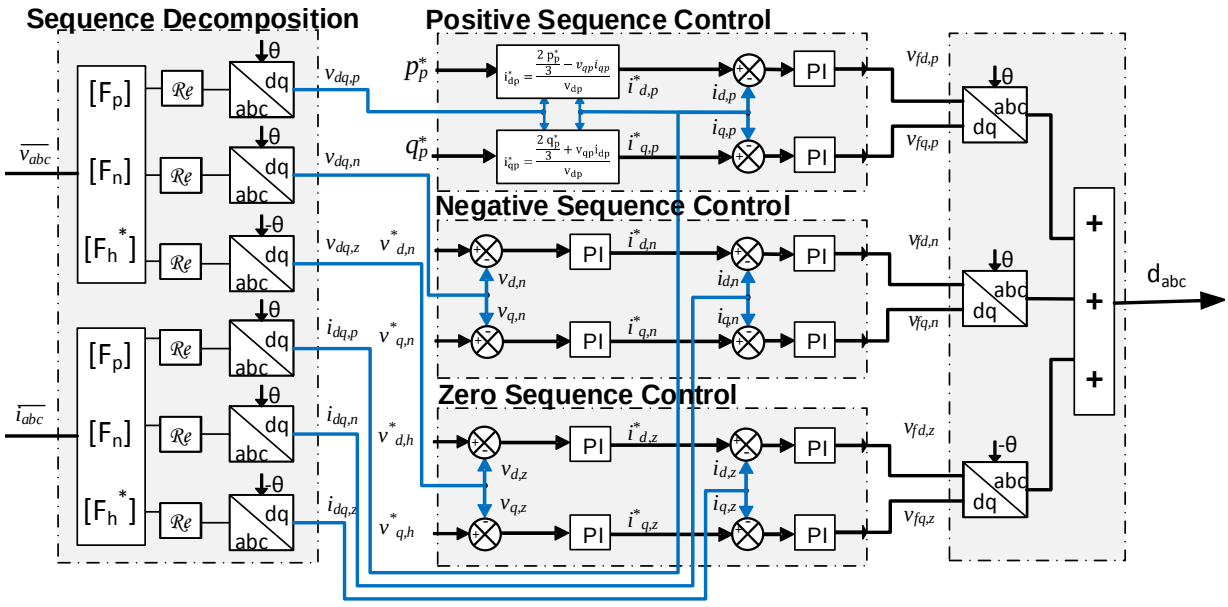

Figure 4.19 Grid feeding mode control structure

4.4.6 Grid supporting and V/f droop control

Conventional P/f and Q/V droop controls have been proven to be an effective solution for grid supporting mode by controlling the voltage amplitude and frequency, especially in MV networks thanks to the predominant inductive behaviour of the line. However, the performance of this kind of control is highly dependent on the R/X ratio of the line and does not provide a satisfactory result in LV networks where the resistive part of the impedance of the line cannot only be neglected but is predominant [30]. For the sake of clarity and because the line impedance will mainly be resistive, the voltage support will be done only through active power control.

In LV networks like distribution networks or MG, the high resistive lines lead to high R/X ratio. In weak networks where R/X>>1 (typically R/X=10) it can be observed that variation of both the active and reactive power will affect the PCC voltage amplitude while the frequency will be affected by the active power balance.

Thus the control of the PCC voltage and the MG frequency cannot be realised simultaneously when the grid is too weak.

A droop control strategy has been chosen for PCC voltage and frequency support, mainly because its implementation is drastically simpler than more advanced technique due to the above-mentioned constraints. The droop controllers will be implemented on top of the grid feeding model using (4.62) for voltage support and (4.63) for frequency support, where the $|V_d^+|$ is the voltage module on the d axis of the positive sequence, and F_{PLL} the frequency measured at the PCC through a Phase Locked Loop (PLL) algorithm. The voltage and frequency support droop gains D_V and D_F units are in [kW/V] and [kW/Hz] and will be selected later on in Chapter 5.

$$P_V^* = D_V\,(V_{PCC}^* - |V_d^+|) \tag{4.62}$$

$$P_F^* = D_F\,(F^* - F_{PLL}) \tag{4.63}$$

4.4.7 Transition between islanded and connected modes

The sequence independent control structure used for both connected and islanded modes are very similar and thus facilitate the transition between the two. Moreover, the use of a well-known control structure on each sequence allows use of the transition methods already proposed in the literature and proven to be effective.

The classic approach for the transition from islanded to connected mode when using a PI double loop control structure consists of bypassing the voltage PI controller of the outer loops, and to reset it to a given value when grid connection occurs. This simple technique used in balanced conditions without independent sequence control has been implemented and proven to be effective both in simulations and experiments [31]. This same method is extended for the sequence independent control structure previously developed to realize smooth transition from islanded to connected mode.

The method consists of bypassing the positive sequence outer voltage loop controller for disconnection from the MG and resetting its output to be equal to

the currents of dq axis when the grid connection occurs. This sequence is depicted in Figure 4.20.

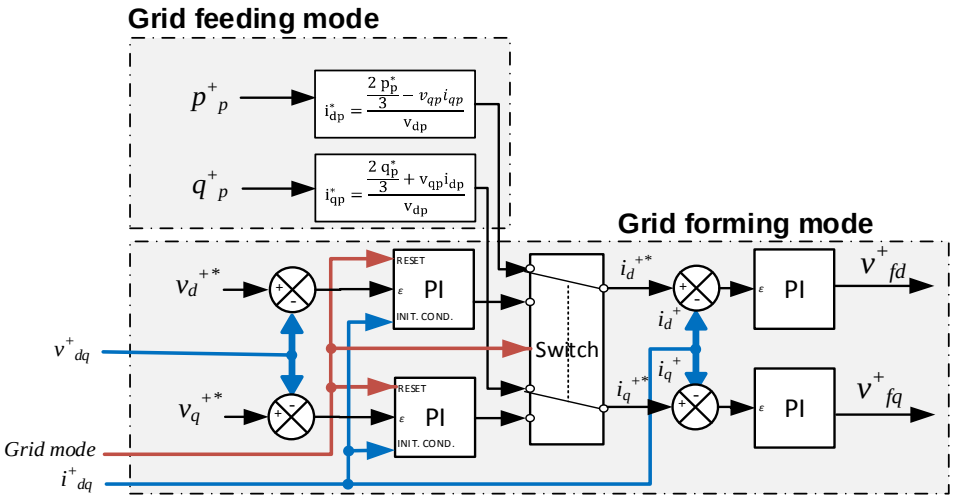

Figure 4.20 Principle for the transition between islanded and MG connected mode

In the same way the transition between the grid feeding to grid supporting mode is done by using the equation (4.62) and (4.63) to set the positive sequence active power reference for voltage and frequency support. It should be noted that the gradients for both active and reactive power set points should be limited thus rate limiter have been implemented to limit the transient magnitude and avoid disturbing the controller operation.

4.4.8 Control tuning

The structure of the sequence decomposition control allows the use of a PI control strategy and existing tuning methods. The double loop control of a VSI uses a two-step tuning method. The first step consists of tuning the inner current loop followed by the outer voltage loop. This process is then reproduced using the model of the plant for each sequence iteratively.

Each sequence control shares the same structure and only the model of the plant changes. If we neglect the decoupling between d and q axis, the gains of the controller on each axis are equals. Thus the elementary control on d and q axis, and for the positive, negative and zero sequences can be reduced to the simplified block representation of Figure 4.21 which is used in this work to tune the 12 PI

controllers of the overall AC side control strategy. This elementary model considers that the sequence decomposition dynamics can be approximated by a first order low-pass filter of settling time corresponding to the selected delay (i.e. 1/16th of a period – 1.25ms).

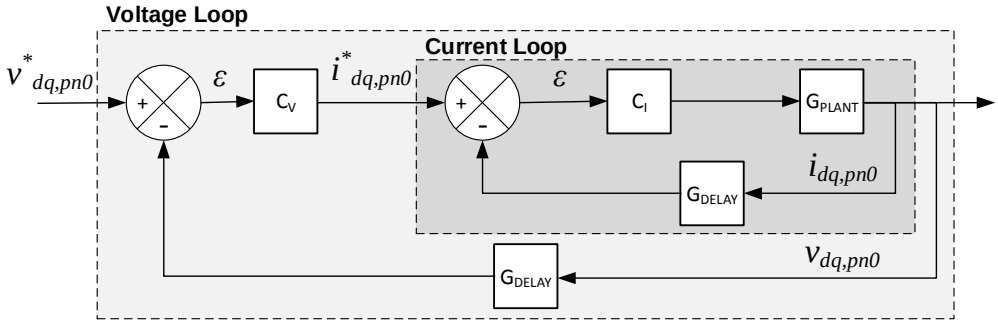

Figure 4.21 Bloc representation of the elementary closed loop structure used to tune the AC side control

The model of the plant is derived from the Laplace transform of the inverter connected mode equation (4.50) and gives the transfer function in (4.64) for the positive and negative sequence, and the transfer function in (4.65) for the zero sequence one, with R_f , L_f , R_g and L_g the filtering inductor resistance and inductance of the inverter and MG respectively.

$$\overline{G^+_{plant}} = \frac{\overline{V_l^+}}{\overline{V_g^+}} = \overline{G^-_{plant}} = \frac{\overline{V_l^-}}{\overline{V_g^-}} = \frac{\dfrac{1}{\overline{R_f + R_g}}}{1 + \dfrac{L_f + L_g}{R_f + L_g}\, s} \tag{4.64}$$

$$\overline{G^0_{plant}} = \frac{\overline{V_l^0}}{\overline{V_g^0}} = \frac{\dfrac{1}{\overline{4(R_f + L_g)}}}{1 + \dfrac{L_f + L_g}{R_f + R_g}\, s} \tag{4.65}$$

In grid-connected mode, the gain of the current loop controller should be different from the grid forming one. For the sake of clarity, and because these gains can be close enough for certain conditions, the same gain will be used both in islanded and connected mode. The hypothesis supporting this choice lies in the grid's weakness. Indeed the grid's parameters will be selected to be representative of a

LV distribution network with high resistive and low inductive profile. Thus the stiffness of the grid enables to neglect the dynamic in islanded mode and to consider only the grid-connected mode for the controller tuning.

In order to tune the controller properly and select an appropriate settling time, the performance and stability have to be assessed. To do so the PI gains are calculated for several settling time targets, and the resulting closed-loop transfer function of the system is analysed. The step response's actual settling time and overshoot are good performance indicator, while the Bode diagram of the open loop transfer function gives the gain and phase margins which are used for stability checks. The inductive filter is set to R_f=10mΩ and L_f=3mH, and the MG impedance to R_g=1.5Ω and L_g=0.5mH which gives a R/X ratio of approximatively 10.

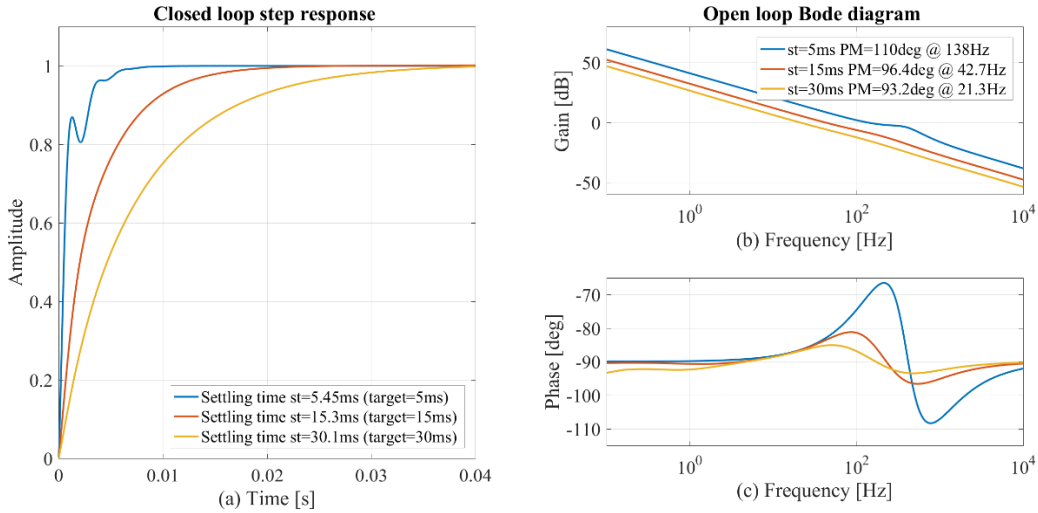

Figure 4.22 Variation of the settling time in the PI tuning process of the positive and negative sequence control, (a) step response of the closed-loop transfer function with the measured settling time, (b) and (c) the Bode diagram of the open loop transfer function with the Phase Margin (PM)

Figure 4.22 shows the step response of the closed loop transfer function (a), the gain (b) and the phase (c) of the open loop transfer function for three different outer loops settling time, the inner loop one being divided by a factor of 2.5. First, it can be seen that the step response of the most rapid case presents some oscillations and the higher the settling time the smoother the step response is.

This is due to the fact that rapid response will result in higher gains and decreased stability. In the same way the higher the settling time target, the closer the measured one is. It can be seen also that the step responses are very close to a first-order one. This results from using a phase margin constraint of 90° in the tuning algorithm which forces the closed loop transfer function to be the first order. Lower values for the phase margin lead to higher order closed loop transfer function, but as a consequence overshoot has to be managed and the performance is decreased. Another consequence of setting a phase margin of 90 degrees target and having a first order closed loop is that the open loop transfer function will be close to an integrator considering the double loop structure. Thus the phase is centred at 90° and the gain margin tends to infinity.

The same process has been applied to the zero sequence control channel. The only difference compared to the previous case is the plant model, but this last is very similar to the positive and negative transfer function as only the static gain changes. As a consequence, the results displayed in Figure 4.23 are very close to the previous ones, and the same comments apply.

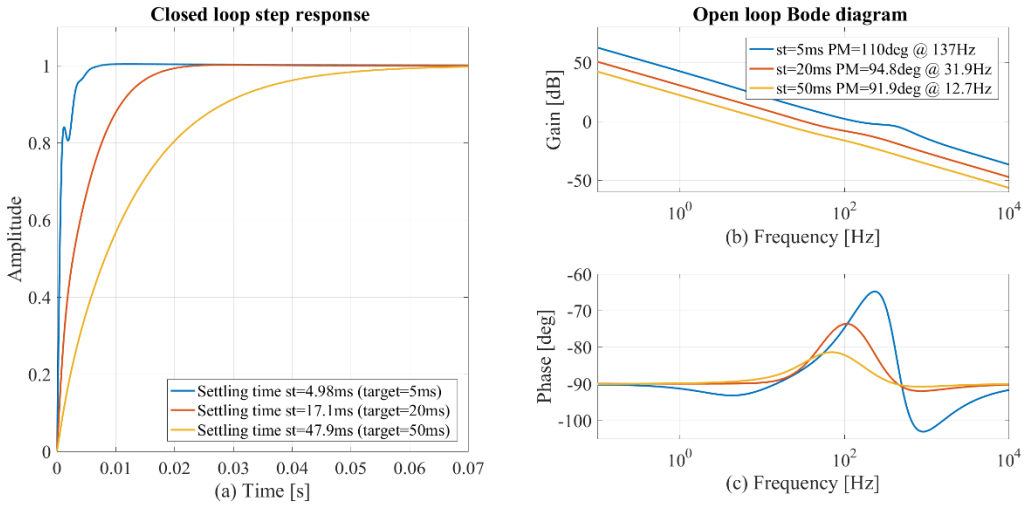

Figure 4.23 Variation of the settling time in the PI tuning process of the zero sequence control, (a) step response of the closed-loop transfer function with the measured settling time, (b) and (c) the Bode diagram of the open loop transfer function with the Phase Margin (PM)

Considering the previous results, the selected settling time is 25ms for the positive and negative sequence voltage loops and 50ms for the zero sequence voltage loops. Using the parameters in Table 4.14, the tuning algorithm gives the PI gains in Table 4.15 and will be used in both simulation and experiment in Chapter 5. These settings are on the conservative side in order to mitigate the uncertainties caused by the design approximations, but mainly the uncertainties caused by grid line impedances mismatch which is an issue that is more likely to happen in a real-world application where the exact parameters are subject to variation over time. This latter issue is discussed in the following section.

Parameter	Value
Sampling time T_s [µs]	100
Settling time sequence +− [ms]	25
Settling time sequence 0 [ms]	50
Filter resistance R_f [Ω]	0.01
Filter inductance L_f [mH]	3
Grid line resistance R_g [Ω]	1.5
Grid line inductance L_g [mH]	0.5
Phase margin target [deg]	90

Table 4.14: Parameters for AC side control calculation

	Voltage loop		Current loop	
	Kp	Ki	Kp	Ki
Positive sequence	0.428	162	1.55	547
Negative sequence	0.428	162	1.55	547
Zero sequence	0.227	65.5	2.49	1776

Table 4.15: AC side PI controllers discrete gains (ts=100µs)

4.4.8.1 Controller parametric robustness

Uncertainties in the grid model are likely to happen in a real case study. To assess the robustness of the controller to withstand grid resistance and inductance uncertainties, the step response of the complete closed-loop transfer function is drawn under grid impedance variations. Figure 4.24 shows the step response under

variations of the line resistor and Figure 4.25 while inductance variation. The R/X ratio is kept equal between each case and displayed so the controller stability can be assessed when the grid weakness varies too. As can be seen, variations of the line resistor results in small changes in the step response and only the settling time is slightly affected. On the contrary, line inductance variations does affect the system response. Indeed for large inductance values, it can be noted that the system oscillates and the stability gets compromised. This is due to the fact that line resistance or inductance variations affect the grid model time constant and if this value is lower than the settling time used to tune the controller the stability cannot be insured. Although the controller settling time has been set to conservative values to increase robustness under grid uncertainties, the values for which the controller starts to oscillate are unrealistic for a real application and increasing slightly the settling time does improve robustness by reducing the PI gains, especially underline resistor variations.

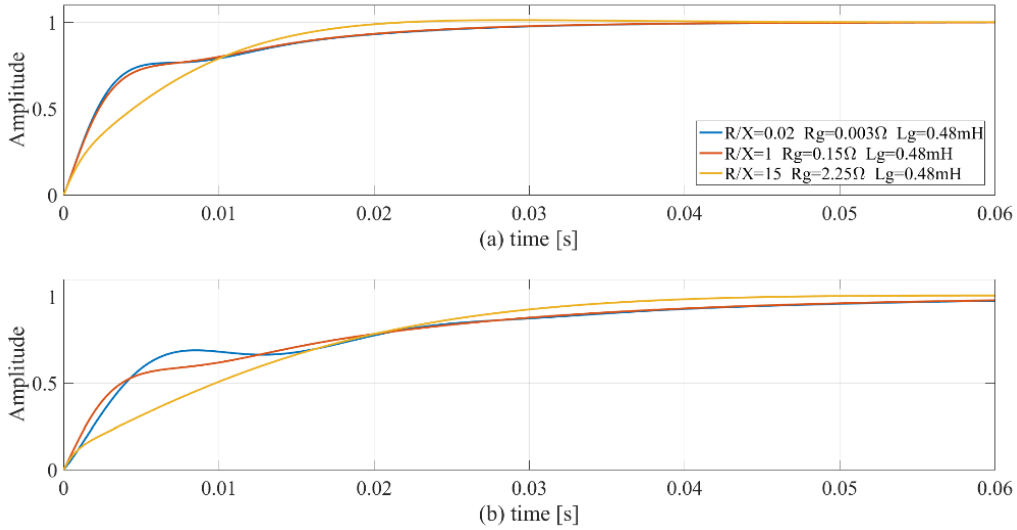

Figure 4.24 Variation of the closed-loop system step response under line resistance uncertainty and constant inductance (a) positive and negative (b) zero sequence

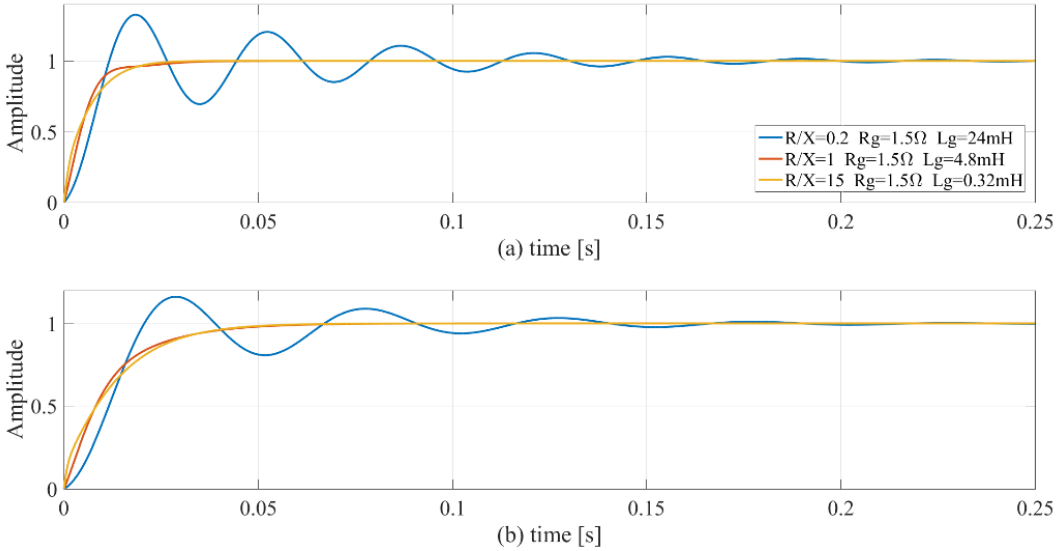

Figure 4.25 Variation of the closed-loop system step response under line inductance uncertainty and constant resistance (a) positive and negative (b) zero sequence

Finally, even though the hypothesis are not conservative, especially concerning the tuning of the control using the connected grid model only and the approximation of the sequence decomposition dynamic using a low pass filter, the good stability while reasonable grid impedance uncertainties show the system is stable, thus it should also mitigate the design uncertainties.

4.5 Chapter conclusions

This chapter has focussed on the low-level control of the multipurpose power converter. The control levels have been defined following the standardized structure given by the ISO 62264 standard. Then two control strategies have been designed, tuned and compared for the DC side HESS control. Results show that the non-linear 2SMC control strategy is more effective and robust than the classical PI one. The AC side control using a sequence-independent control has then been developed in order to comply with the high power quality required. A discussion on the signal decomposition using different means to obtain the complex signals of the current and voltage measurements in a discrete environment has shown that the delay based method gives satisfactory results. The selected control structure has been developed for the grid forming, grid feeding and grid supporting modes. Finally, the tuning of the controller has shown good stability and performance.

4.6 Chapter references

[1] O. Palizban, K. Kauhaniemi, and J. M. Guerrero, "Microgrids in active network management - Part I: Hierarchical control, energy storage, virtual power plants, and market participation," *Renew. Sustain. Energy Rev.*, vol. 36, pp. 428–439, 2014.

[2] S. M. Nosratabadi, R. A. Hooshmand, and E. Gholipour, "A comprehensive review on microgrid and virtual power plant concepts employed for distributed energy resources scheduling in power systems," *Renewable and Sustainable Energy Reviews*, vol. 67. pp. 341–363, Jan-2017.

[3] L. Che, M. Shahidehpour, M. F. Benkhoris, and F. L. Lewis, "Hierarchical Coordination of a Community Microgrid With AC and DC Microgrids," *IEEE Trans. Smart Grid*, vol. 6, no. 6, pp. 3042–3051, Nov. 2015.

[4] C. M. Liaw, J. Xiao, and P. Wang, "Hierarchical Control of Hybrid Energy Storage System in DC Microgrids," *IEEE Trans. Ind. Electron.*, vol. 62, no. 8, pp. 4915–4924, Aug. 2015.

[5] P. Tian, Z. Nie, K. Wang, and R. Ding, "A Hierarchical Energy Management System Based on Hierarchical Optimization for Microgrid Community Economic Operation," *IEEE Trans. Smart Grid*, vol. 7, no. 5, pp. 2230–2241, Sep. 2016.

[6] B. Su, X. Lu, W. Feng, J. Guerrero, and Z. Nie, "Active Power Quality Improvement Strategy for Grid-connected Microgrid Based on Hierarchical Control," *IEEE Trans. Smart Grid*, vol. PP, no. 99, pp. 1–1, 2017.

[7] B. Su, X. Lu, W. Feng, J. Guerrero, and Z. Nie, "Active Power Quality Improvement Strategy for Grid-connected Microgrid Based on Hierarchical Control," *IEEE Trans. Smart Grid*, vol. PP, no. 99, pp. 1–1, 2017.

[8] N. Celanovic and D. Boroyevich, "A comprehensive study of neutral-point voltage balancing problem in three-level neutral-point-clamped voltage source PWM inverters," *IEEE Trans. Power Electron.*, vol. 15, no. 2, pp. 242–249, Mar. 2000.

[9] J. Pou, J. Zaragoza, S. Ceballos, M. Saeedifard, and D. Boroyevich, "A

Carrier-Based PWM Strategy With Zero-Sequence Voltage Injection for a Three-Level Neutral-Point-Clamped Converter," *IEEE Trans. Power Electron.*, vol. 27, no. 2, pp. 642–651, Feb. 2012.

[10] A. Levant, "Sliding order and sliding accuracy in sliding mode control," *Int. J. Control*, vol. 58, no. 6, pp. 1247–1263, 1993.

[11] A. Etxeberria, I. Vechiu, H. Camblong, and J.-M. Vinassa, "Comparison of Sliding Mode and PI Control of a Hybrid Energy Storage System in a Microgrid Application," *Energy Procedia*, vol. 12, pp. 966–974, 2011.

[12] A. Polyakov and A. Poznyak, "Reaching time estimation for 'super-twisting' second order sliding mode controller via Lyapunov function designing," … *Control. IEEE Trans.*, vol. 54, no. 8, pp. 1951–1955, Aug. 2009.

[13] A. Susperregui, M. I. Martinez, I. Zubia, and G. Tapia, "Design and tuning of fixed-switching-frequency second-order sliding-mode controller for doubly fed induction generator power control," *IET Electr. Power Appl.*, vol. 6, no. 9, p. 696, 2012.

[14] A. Etxeberria, I. Vechiu, H. Camblong, and J.-M. Vinassa, "Comparison of three topologies and controls of a hybrid energy storage system for microgrids," *Energy Convers. Manag.*, vol. 54, no. 1, pp. 113–121, Feb. 2012.

[15] W. Jing, C. H. Lai, S. H. W. Wong, and M. L. D. Wong, "Battery-supercapacitor hybrid energy storage system in standalone DC microgrids: areview," *IET Renew. Power Gener.*, vol. 11, no. 4, pp. 461–469, 2016.

[16] T. S. T. Siew, M.-E. Choi, and S.-W. Kim, "Energy Management Optimization in a Battery/Supercapacitor Hybrid Energy Storage System," *IEEE Trans. Smart Grid*, vol. 3, no. 1, pp. 463–472, Mar. 2012.

[17] M.-E. Choi, S.-W. Kim, and S.-W. Seo, "Energy Management Optimization in a Battery/Supercapacitor Hybrid Energy Storage System," *IEEE Trans. Smart Grid*, vol. 3, no. 1, pp. 463–472, Mar. 2012.

[18] J. L. Blackburn and R. Hemmati, "Emergence of hybrid energy storage systems in renewable energy and transport applications – A review," *Renew. Sustain. Energy Rev.*, vol. 65, pp. 11–23, Nov. 2016.

[19] V. Delgado-Gomes and P. Borza, "A biological approach for energy management in smart grids and hybrid energy storage systems," in *Optimization of Electrical and …*, 2014, pp. 1082–1086.

[20] Y. Riffonneau, S. Bacha, F. Barruel, and A. Delaille, "Energy flow management in grid connected PV systems with storage - A deterministic approach," 2009, pp. 1–6.

[21] R. H. Lopez Rodriguez, I. Vechiu, S. Jupin, S. Bacha, Q. Tabart, and E. Pouresmaeil, "A new energy management strategy for a grid connected wind turbine-battery storage power plant," in *IEEE International Conference on Industrial Technology (ICIT)*, 2018, pp. 873–879.

[22] A. Aguilera-Gonzalez, I. Vechiu, R. H. L. Rodriguez, and S. Bacha, "MPC Energy Management System For A Grid-Connected Renewable Energy/Battery Hybrid Power Plant," in *2018 7th International Conference on Renewable Energy Research and Applications (ICRERA)*, 2018, pp. 738–743.

[23] M. J. Hossain, M. A. Mahmud, F. Milano, S. Bacha, and A. Hably, "Design of Robust Distributed Control for Interconnected Microgrids," *IEEE Trans. Smart Grid*, vol. 7, no. 6, pp. 2724–2735, Nov. 2016.

[24] I. Vechiu, O. Curea, and H. Camblong, "Transient Operation of a Four-Leg Inverter for Autonomous Applications With Unbalanced Load," *IEEE Trans. Power Electron.*, vol. 25, no. 2, pp. 399–407, Feb. 2010.

[25] H. Bevrani, B. François, and T. Ise, *Microgrid Dynamics and Control*. John Wiley & Sons, 2017.

[26] P. Rodriguez, A. Luna, M. Ciobotaru, R. Teodorescu, and F. Blaabjerg, "Advanced Grid Synchronization System for Power Converters under Unbalanced and Distorted Operating Conditions," 2006, pp. 5173–5178.

[27] N. Mendalek and R. H. Lasseter, "Formulations for the apparent and unbalanced power vectors in three-phase sinusoidal systems," *Electr. Power Syst. Res.*, vol. 160, pp. 37–43, Jul. 2018.

[28] R. Lopez, "On the definition of power factor and apparent power in

unbalanced polyphase circuits with sinusoidal voltage and currents," *IEEE Trans. Power Deliv.*, vol. 8, no. 3, pp. 841–852, Jul. 1993.

[29] A. Ovalle, S. Member, G. Ramos, S. Bacha, A. Hably, and A. Rumeau, "Decentralized Control of Voltage Source Converters in Microgrids Based on the Application of Instantaneous Power Theory," *IEEE Trans. Ind. Electron.*, vol. 62, no. 2, pp. 1152–1162, 2014.

[30] K. De Brabandere, "Voltage and Frequency Droop Control in Low Voltage Grids by Distributed Generators with Inverter Front-End," *Ph.D. dissertation*, 2006.

[31] A. Etxeberria, "Microgrid Hybrid Energy Storage Integration and Control using a Three-Level NPC Converter," *Ph.D. dissertation*, 2012.

Chapter 5

Simulation and experimental validation

Contents

In this chapter, the designed controllers are tested both in simulation and experimentally. First, the test grid and the experimental test bench is described. Then the grid forming controller will be tested along with the PI and 2SMC HESS controllers. Then both grid feeding and grid supporting control strategies will be tested on the dynamic MG where a low order System Frequency Response (SFR) is implemented. Finally a conclusion on the ability of the 4 Leg 3LNPC power converter to realize an HESS interface to a weak grid and a RES while improving the MG power quality delivery is given.

5.1 Microgrid test bench description

The microgrid test bench used in this thesis for validation purposes lies in ESTIA laboratory. This microgrid is designed to be a flexible test bench centred on two 4 wires AC buses on which various equipment can be connected. The presence of a DC bus along with the AC ones enable another degree of flexibility and is consistent with the hybrid AC/DC microgrid as described in Chapter 2. This microgrid test bench is equipped with several sources, loads and lines for a 20kW peak power. Figure 5.1 shows a picture of the test bench. The main microgrid's equipment used for the validation of the present work are detailed hereafter.

OP5600 HIL box: The microgrid is driven by the OP5600 real-time HIL simulator. It allows measurement of the different MG variables, implementation of the control algorithms and to generate the control signals. It uses Matlab/Simulink to develop the embedded algorithm. The OP5600 is powered by a 4 core processor which allows splitting of the algorithm according to the specific time step (multi-rating). The FPGA driven PWM outputs provide fast and accurate signals to the power converter static switches. The 16 bits analog I/O board allows also precise and fast measurement and signal generation. It supports RS232 and Modbus communication protocol.

PAS1000 S&B: The Spitzenberger PAS1000 are 3 high end 4 quadrant AC and DC voltage amplifiers. Each one can continuously supply 1000 VA in AC and 1500 W in DC. The maximum voltage range is 570V in DC. The control of these three amplifiers is managed through an analog link to the HIL box.

Synergia dual DC source: (Modbus) The Synergia dual source is a 4 quadrant 7KW DC voltage amplifier. Its maximum voltage range is 520V and it is controlled through a MODBUS link to the HIL box.

Programmable AC source: The California 2253iX is a three-phase AC source of 2.25 kVA. It can be used to create a three-phase system of variable frequency, amplitude, and quality through a tuneable crest factor. This source is only one quadrant and can be controlled through a RS232 link.

Programmable AC loads: Three California Instruments 3091LD are used as AC loads for a total of 3kVA. These loads are designed to provide precisely controlled non-linear loads for testing AC power generation equipment in real operating conditions.

4L-3L-NPC Inverter prototype: This NPC inverter is a custom made 4 leg 3LNPC build by ARCEL design office. This converter has rated values of 1200V/50A which is oversized for the current peak power of the microgrid, but such margin does not influence the validity of the experimental results and it allows easy expansion the microgrid with larger power supplies in the future. It is built on the same basis as industrial inverters.

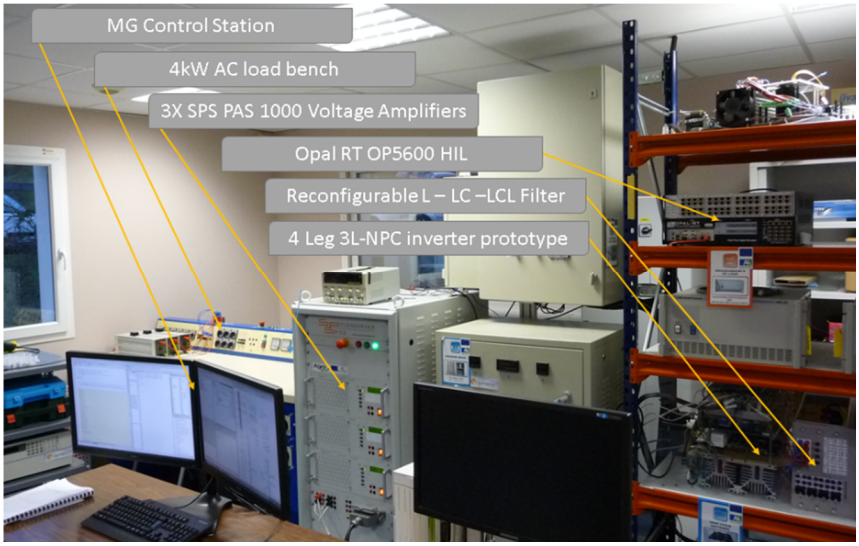

Figure 5.1 Experimental MG

ESSs technologies are emulated in real time using their numerical models and high bandwidth power amplifiers. This gives a high fidelity experimental microgrid hybrid test bench [1], [2].

5.2 Islanded mode and grid forming case study

The grid forming control used while in islanded mode is tested in this section. The islanded mode being simpler case compared to the grid feeding and grid supporting ones, the DC side control will also be tested in this section. Both the 2SMC and PI DC side controllers designed in sections 4.2.1 and 4.2.2 respectively will be tested in simulation, and the 2SMC will be later on tested experimentally along with the grid forming controller, using the same scenario but at lower power.

5.2.1 Overview of the islanded grid and scenario

The islanded grid case study involves the 4 Leg 3LNPC feeding a load and supplied on the DC bus by a RES controlled as a current source in parallel with two ESS connected in series. For the experimental part, the test bench uses two S&B PAS1000 1 kW voltage amplifiers to emulate the ESSs and a third one as a current source injecting on the DC bus to emulate the RES. Due to laboratory limitation compared to the simulation tests, the voltages of the ESSs are divided by a factor of 2.2 and the peak voltage of the AC side is reduced by the same factor. The block representation of the experimental set up given in Figure 5.2 is equivalent to the simulation layout.

The topology limits analysis carried out in section 3.4 has shown that the reactive power does not affect the boundaries of the system. Because in this mode the reactive power is set by the load and does not affect the VRB control, the voltage and the frequency, the load used for both simulation and experiment will be purely resistive. The load should also be able to be unbalanced in order to test the ability of the AC side control to maintain balanced voltages, as well as the DC side control ability to smooth the current ripples on the VRB. Finally, because using an electronic load with the 3LNPC inverter prototype has shown electromagnetic compatibility issues in preliminary experiments, the load will be composed of two

passive loads on which an unbalance can be created thanks to an electromechanical contactor plugged to the HiL box.

The values for the filtering components of the inverter and its switching frequency will be kept equal for both simulation and experiments, and the gains of the controllers calculated with these values too. Even though the experimental validation will be carried out at lower power, having the same filter components sizing and thus the same gains will preserve the dynamic of the system. The passive components have been selected according to that available and their values are 3.3mF for the DC side filter and 3mH for the inductor. The switching frequency has been selected to be several order of magnitude higher than the AC frequency to 10 kHz (i.e. 200 times) in order to comply with the averaged model technique used to design the controllers. This switching frequency is relatively high for an industrial application and will result in higher switching losses but it is consistent with the power quality standard that is needed, especially in islanded mode.

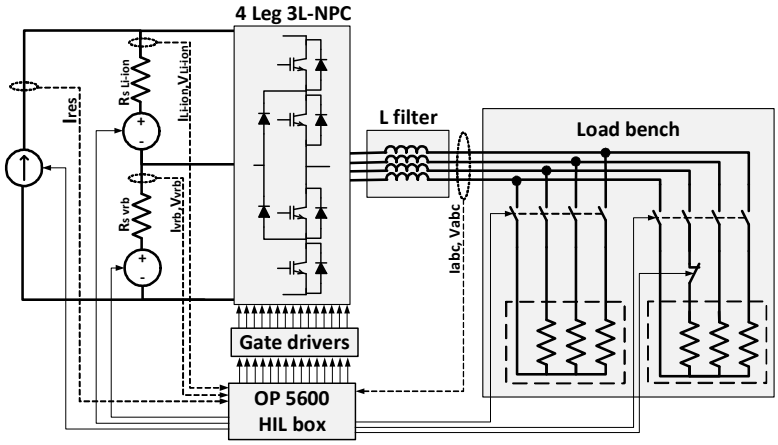

Figure 5.2 Diagram of the experimental tests in the islanded case study

Parameters	**Simulation**	**Experiment**
Switching frequency F_{sw} [kHz]	10	10
AC RMS voltage L-N V_{ac} [V]	230	105
AC filter L_f [mH]	3	3
DC filter C [mF]	3.3	3.3
VRB power settling time [s]	0.25	2.5

Table 5.16: Simulation and experiment parameters

The DC side control will be tested on the whole range available. To do so the results of the structural limits analysis of section 3.4 will be implemented. Although it has been concluded that the power flow division between HESS is not dependant on the load unbalances, section 2.4 stresses that the practical implementation of the VRB power controller should involve a margin to avoid overmodulation. The VRB current controller injects a variable signal in the modulation in order to compensate the DC side current ripples. As a result, the zero sequence injection oscillates and has been seen that the amplitude of these periodic components is hardly expressible and so quantifiable. Thus it has been identified that a 10% margin of the AC active power on the VRB power boundaries as in (3.9) allows avoiding overmodulation and ensures no distortion in the AC waveforms.

$$P_{vrb}^{min/max} = -\frac{P_{res}A_2}{2} + P_{ac}\,K_{bot}^{Zs\,min/Zs\,max} \pm 0.1\,P_{ac} \tag{5.66}$$

Finally, the VRB power boundaries of equation (3.9) are implemented as illustrated in Figure 5.3, using the surfaces K_{top} K_{bot} of section 3.4.3. The reference selector is set as a simple switch to either maximum or minimum in this case study. The selected reference is then smoothened through a second order low pass filter of unity gain and a settling time given in Table 5.16.

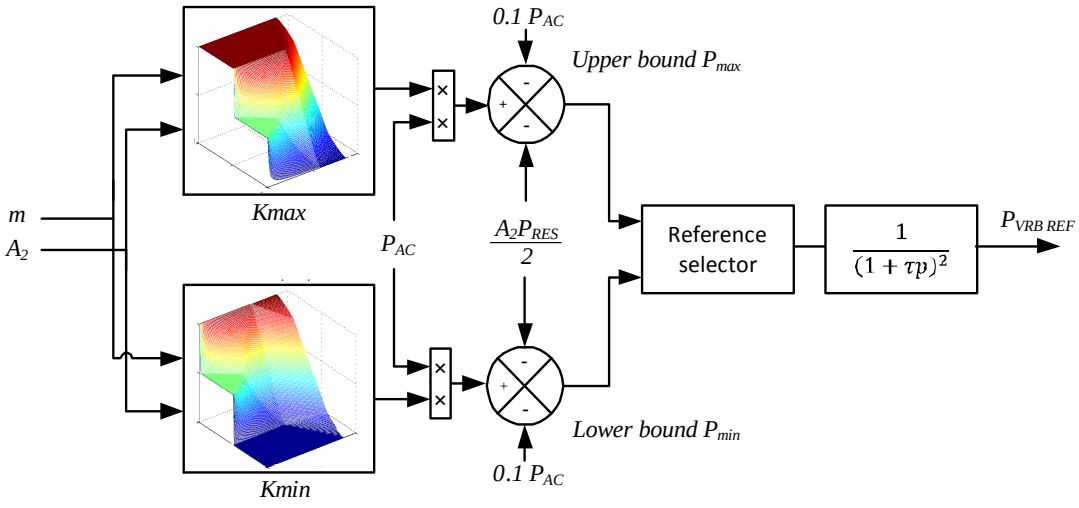

Figure 5.3 VRB power reference definer

5.2.2 Comparison of PI and SMC HESS control

Both the PI and 2SMC controllers along with the limits modelling are assessed simultaneously by simulation means. The 3LNPC used as an interface between a RES, two ESSs and a MG involves a large number of variables, therefore several cases studies have been combined in a unique scenario. The investigated scenario is composed of five sequences separated by events on both AC and DC sides. Taking into account the preformed transitory study in Chapter 4 and for the sake of clarity, the RES injected into the DC bus is kept constant and only the AC side will experience variations. The initial conditions and the events applied are described in Table 5.17.

Case study/Events	**Sequence/Event Desciption**	**Time**
I	P_{ac}=40kW P_{res}=50kW P_{vrb_ref}= P_{vrb_max}	
Event 1	AC load step: from 40kW to 60kW	1s
II	P_{ac}=60kW P_{res}=50kW P_{vrb_ref}= P_{vrb_max}	
Event 2	VRB reference step: from VRB Max to VRB Min	1.5s
III	P_{ac}=60kW P_{res}=50kW P_{vrb_ref}= P_{vrb_min}	
Event 3	AC load step: from 60kW to 40kW	2s
IV	P_{ac}=40kW P_{res}=50kW P_{vrb_ref}= P_{vrb_min}	
Event 4	10 kW monophasic load plugged	2.5s
V	P_{ac}=60kW P_{res}=50kW P_{vrb_ref}= P_{vrb_min}	

Table 5.17: Simulation scenario and event description

Figure 5.4 and Figure 5.5 show the evolution of the AC side active power delivered to the load and the DC mean power of the RES injected, the VRB and Li-Ion ESSs with the PI and 2SMC based DC side HESS controllers respectively.

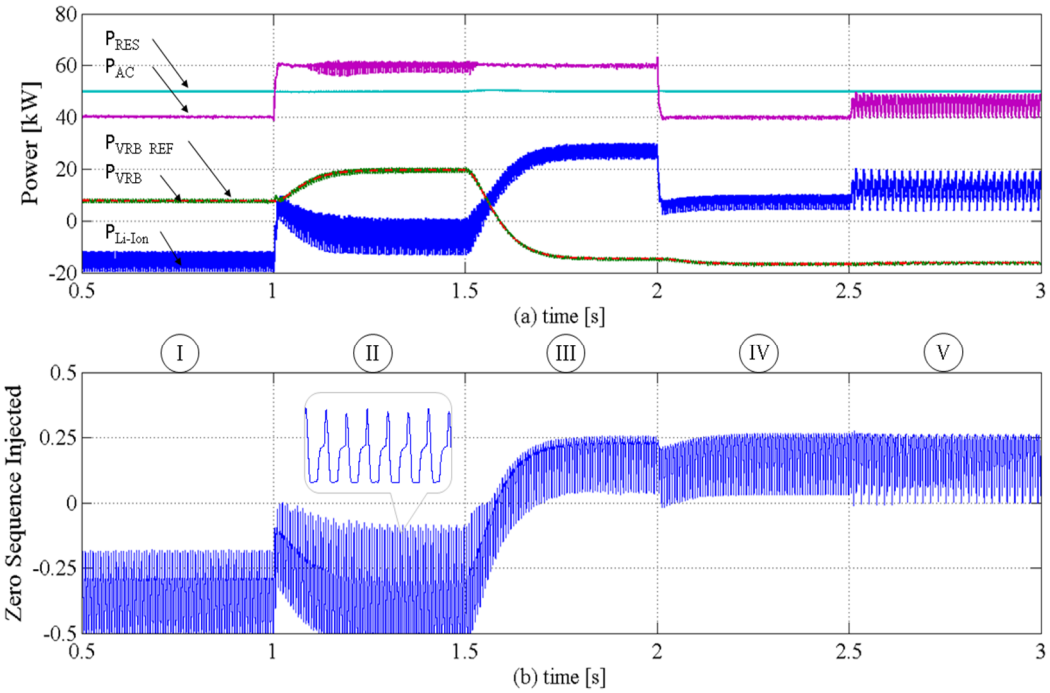

Figure 5.4 Islanded mode PI DC side control under constant RES injection and unbalanced load (a) AC and DC power (b) Zero sequence injection

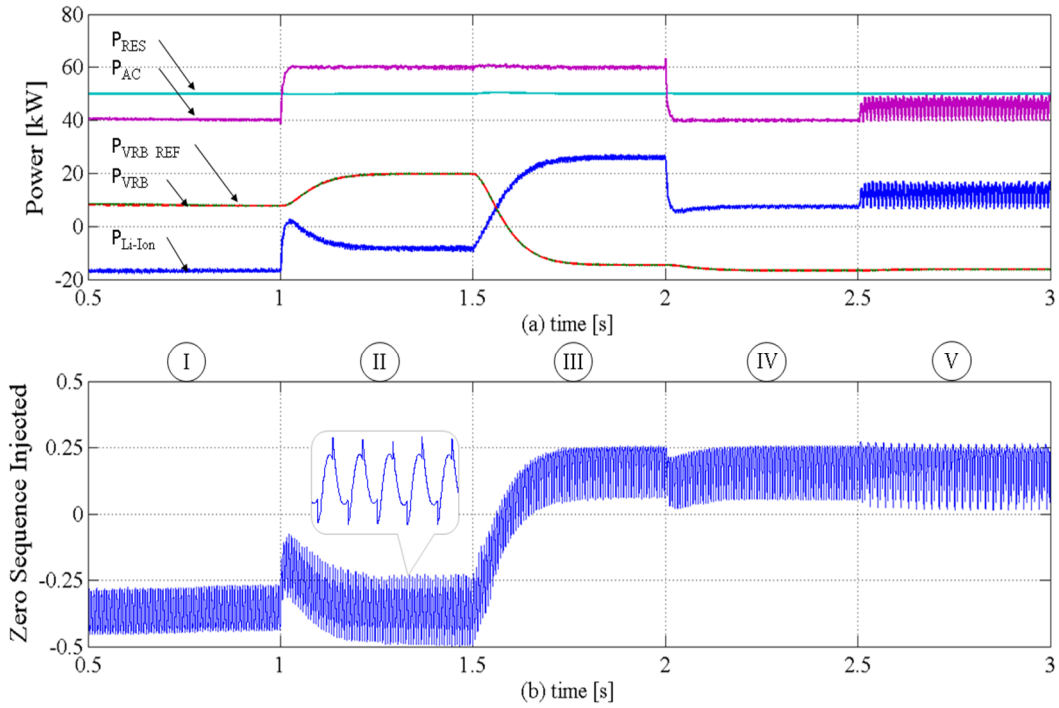

Figure 5.5 Islanded mode 2SMC DC side control under constant RES injection and unbalanced load (a) AC and DC power (b) Zero sequence injection

It can be seen that both 2-SMC and PI control schemes allow the VRB power to be maintained close to its reference, even while the AC load is suddenly increased/decreased (Events 1 and 3) or unbalanced (Case Study V). Concerning the HESS harmonics compensation, the PI control scheme shows only a reduction whereas the 2-SMC suppresses most of the 150Hz component. Despite the peak to peak ripples on the VRB power being moderate (close to 2kW for Case Study II), the Li-Ion reaches a 13kW peak to peak power ripple in the same case for the PI control. It can also be seen that the zero sequence injection in the modulating signals has a much cleaner waveform with the 2-SMC. On the contrary, the PI controlled zero sequence injection has a higher amplitude and reaches the saturation zone at -0.5 for the Cases Studies I and II where the VRB reference is set to the maximum. Finally, the DC harmonics produced by AC load unbalances are better displaced from the VRB to the Li-Ion ESS for the 2SMC scheme. It should be noted that the 10kW single phase load plugged (Case Study V) would involve more than 20A current ripples on the VRB for a constant zero sequence injection, which would increase losses and may reduce its lifetime due to thermal increase.

Moreover, it can be seen in Figure 5.5 (Case study II) that the power taken from the VRB is 20kW and the Li-Ion battery is charging at -9kW. As stated in Section 3.4.5 the topology allows the power of the DC side to be split in a way that can be seen as a power exchange of 9kW between the ESSs from a macro point of view and therefore increases the interest of the topology.

5.2.3 Experimental validation

The previous case study is reproduced experimentally. Although the total duration of the experiment has been extended and the voltages are reduced because of laboratory limitations, the same events are applied experimentally. The detailed description of the scenario is given in Table 5.18.

Case study/Events	Sequence/Event Desciption	Time
I	P_{ac}=1kW P_{res}=1.5kW P_{vrb_ref}= P_{vrb_max}	
Event 1	AC load step: from 1kW to 1.75kW	50s
II	P_{ac}=1.75kW P_{res}=1.5kW P_{vrb_ref}= P_{vrb_max}	
Event 2	VRB reference step: from VRB Max to VRB Min	60s
III	P_{ac}=1.75kW P_{res}=1.5kW P_{vrb_ref}= P_{vrb_min}	
Event 3	AC load step: from 1.75kW to 1kW	70s
IV	P_{ac}=1kW P_{res}=1.5kW P_{vrb_ref}= P_{vrb_min}	
Event 4	500W biphasic load plugged	80s
V	P_{ac}=1.5kW P_{res}=1.5kW P_{vrb_ref}= P_{vrb_min}	

Table 5.18: Experiment scenario and event description

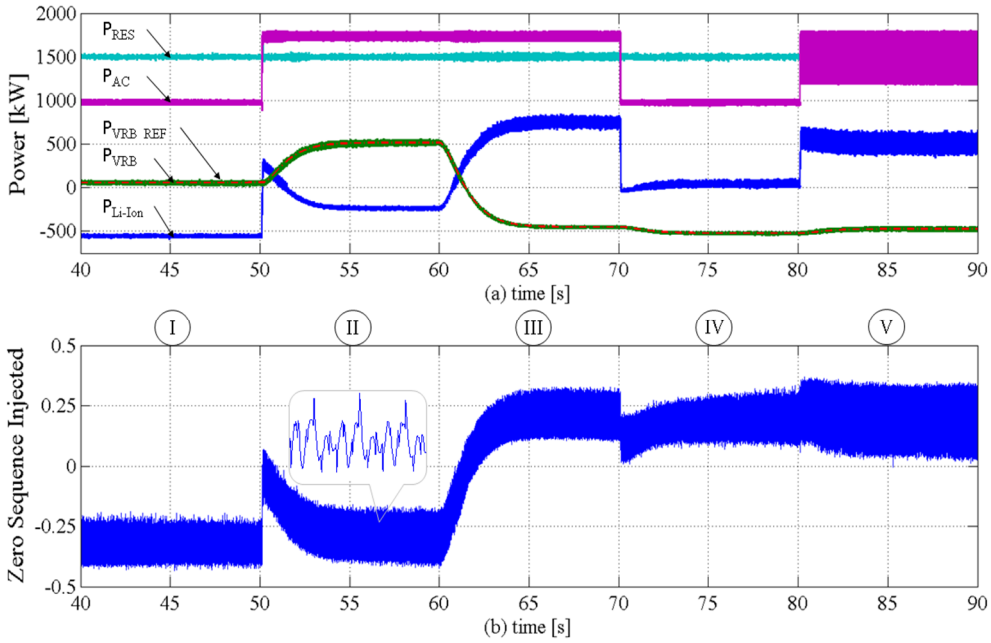

Figure 5.6 Islanded mode 2SMC DC side control under constant RES injection and unbalanced load (a) AC active power and DC mean power (b) Zero sequence injection

As it can be seen in Figure 5.6, the experimental results are very close to the simulation ones. The sudden load increase is effectively provided by the Li-Ion ESS and progressively replaced the VRB one, and in the same way, the load decrease does not affect the VRB power. When the unbalanced load is plugged, the current

oscillation on the DC side is well reported on the Li-Ion ESS as it can be seen on the mean power signals. Although it can be noted that the zero sequence signal presents some chatter which is due to measurement noise, the profile of the zero sequence is very close to the simulation one.

Figure 5.7 and Figure 5.8 show the AC side voltage and current signals in *abc* frame and *dq0* frame after decomposition in positive negative and zero sequences respectively. It can be seen in Figure 5.7 that both the voltage and current waveform are clean and present a very low harmonic content. When the unbalanced load is plugged in Figure 5.7 e) f) the voltage clearly remain balanced. The transient response of the controller which can be observed in Figure 5.8 is approximately equal to 10ms. This value matches the settling time which has been used to tune the controller in grid forming mode.

Overall both DC and AC side controllers show a proper operation even though the measurement noise and parametric uncertainty are quite high in an experimental setup. This confirms the choice of the 2SMC control technique thanks to its robustness with regard to parametric uncertainties as observed in the preliminary study, but also the AC side controller whose robustness has not been previously analysed in detail.

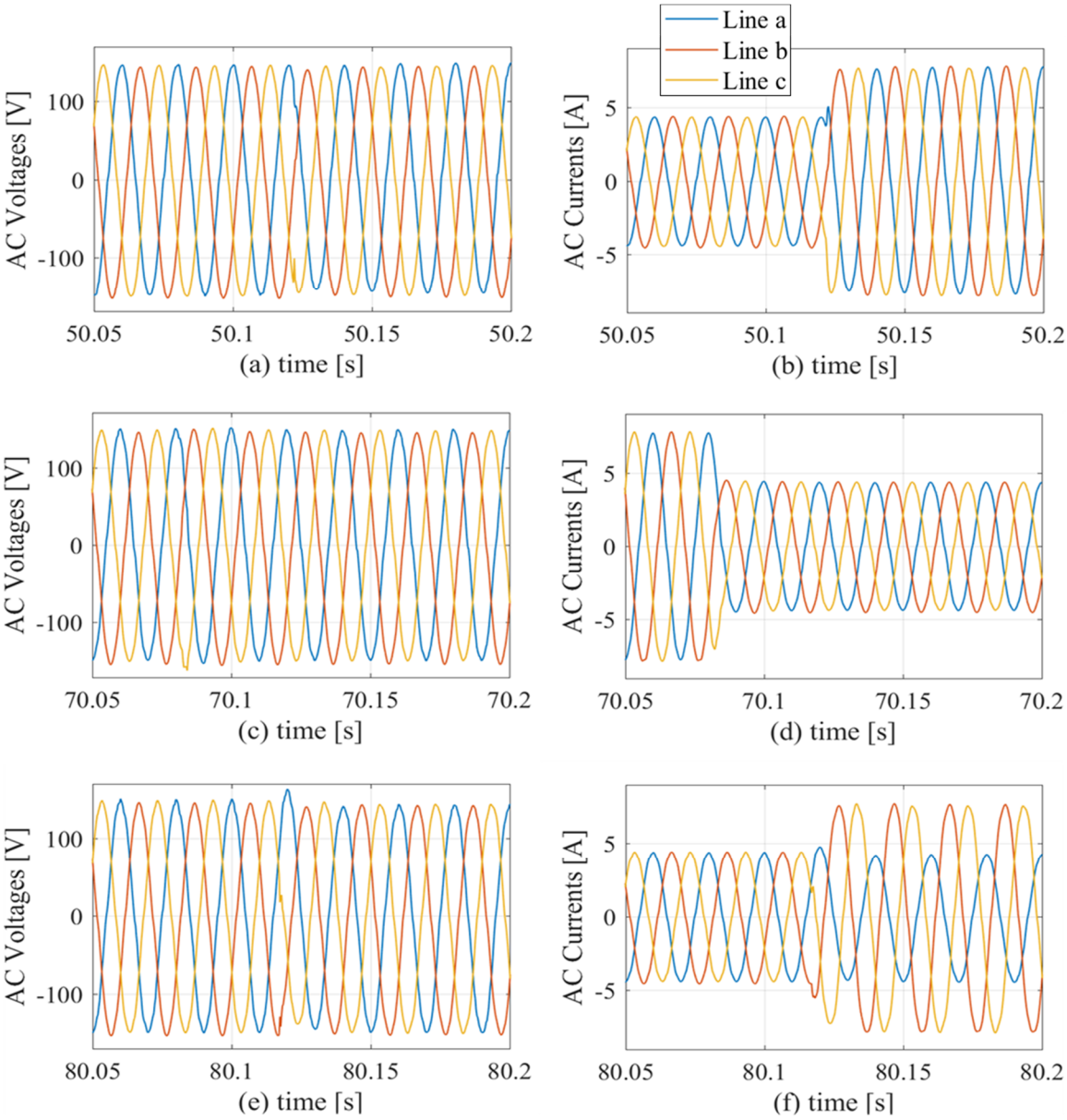

Figure 5.7 Evolution of the experimental AC voltages/currents in *abc* frame for (a), (b) Event 1 (c), (d) Event 3 (e), (f) Event 4

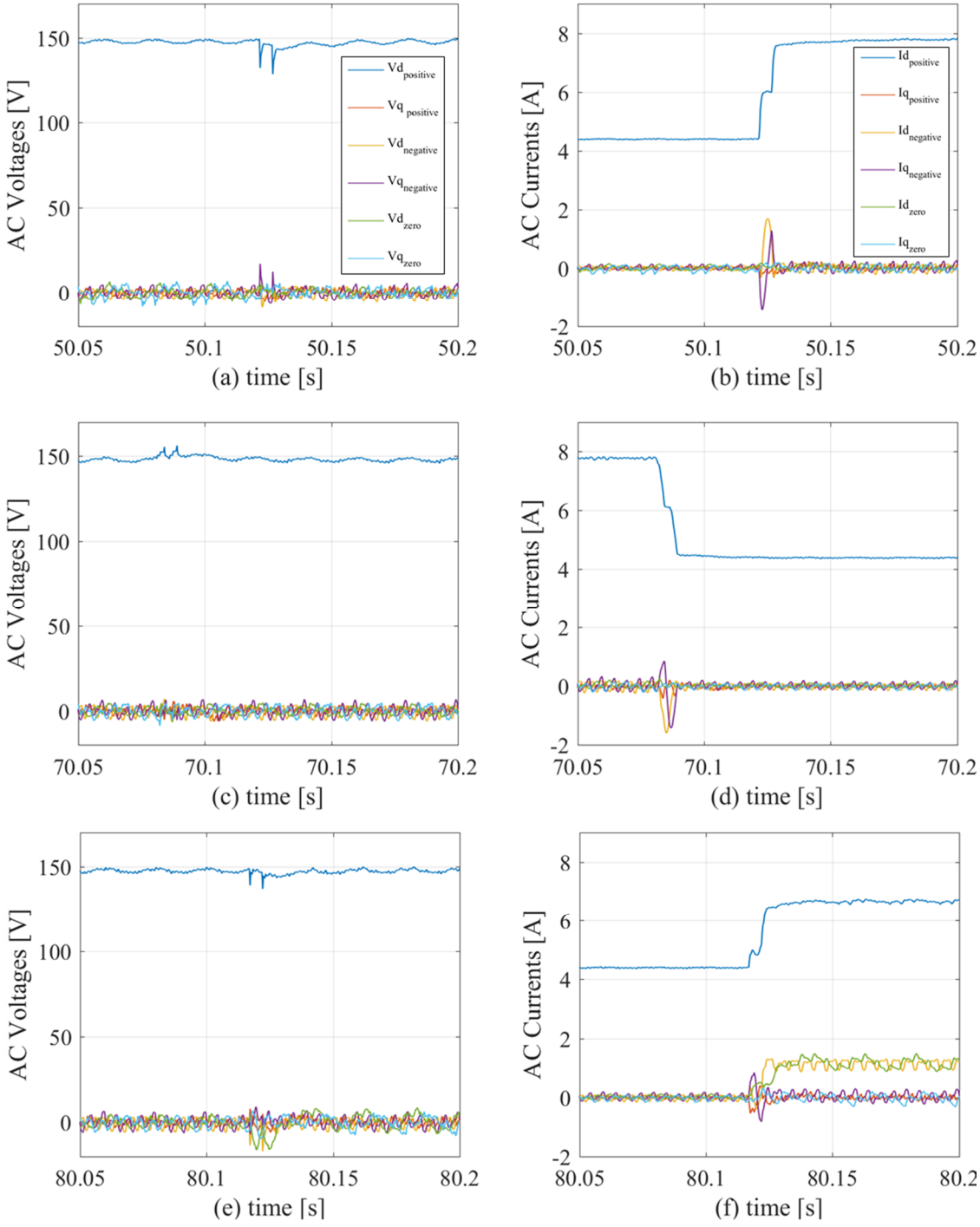

Figure 5.8 Evolution of the experimental AC voltages/currents in dq0 frame for (a), (b) Event 1 (c), (d) Event 3 (e), (f) Event 4

5.3 Grid-connected mode in a weak grid context

5.3.1 Overview of the microgrid model

The objective of this section is to test the ability of the 3L-NPC to interface a RES coupled with a HESS to a MG. Selecting a MG topology is not easy because there are many configurations available depending on the target of the study and the desired level of modelling of the dynamic [3], [4]. Depending on the structure of the network, the loads and generators types, the characteristics of the lines or even the set points, the dynamic response and the stability would change completely from one case to another. Even though lots of attention is given to the topic, there is no available standard such as IEEE test networks for microgrids yet.

The main characteristic of MG dynamic model is its weakness embodied by voltage variation across the network caused by lines impedances, and global active power balance issues that lead to frequency deviation if the network is dominated by synchronous generation [5]. In normal operation mode (i.e. excluding fault cases) and considering that no voltage regulation strategy is already employed, the R/X ratio will define the voltage dynamics at the PCC. On the other hand, the frequency dynamics of a weak grid can be modelled as a function of the global inertia and the damping provided by the rotating machines.

A low order dynamic model using an aggregated representation of a grid has been first presented in [6] and is still widely used to observe the frequency dynamic of power systems [4], [7]–[9]. Even though it excludes the participation of other generation units based on power electronics, this modelling is sufficient for the purpose of the study.

The dynamic model of MG designed for this case study will use a reduced model based on a Thévenin equivalent circuit made of an ideal voltage source and an impedance Z_g. The ideal voltage source will be controlled in frequency by the MG frequency response transfer function of Figure 5.10.

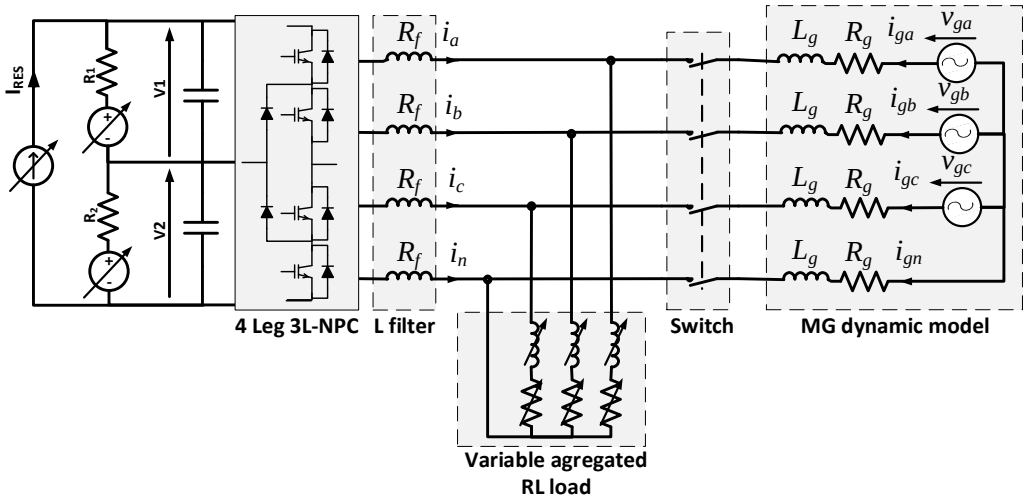

Figure 5.9 Schematic of the MG dynamic model with line impedance and low order SFR

The parameters of the MG dynamics are selected to be representative of a weak grid and given in Table 5.19 [7]. The impedance of the grid is selected in the same way using a ratio R/X=10. The schematic of the MG dynamic model with line impedance and low order system frequency response is shown in Figure 5.10. Finally the MG dynamic frequency response to several active power steps are shown in Figure 5.11.

Parameters	**Value**
L-n RMS MG voltage V_g [V]	250
Line resistance R_g [Ω]	1.5
Line inductance L_g [mH]	0.5
Inertia constant H [s]	0.25
Damping factor D	1
Reheat time constant T_R [s]	0.5
Mechanical Power Gain Factor K_M	0.95
Fraction of total power F_H	0.3
Governor regulation R	0.05
MG frequency bias B [kW/Hz]	100

Table 5.19: MG dynamic model parameters

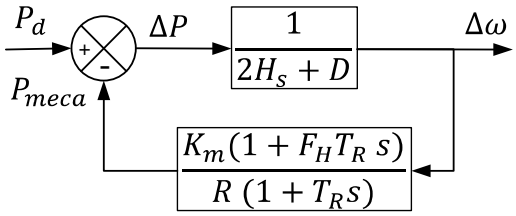

Figure 5.10 Bloc diagram of the MG dynamic frequency low order model [6]

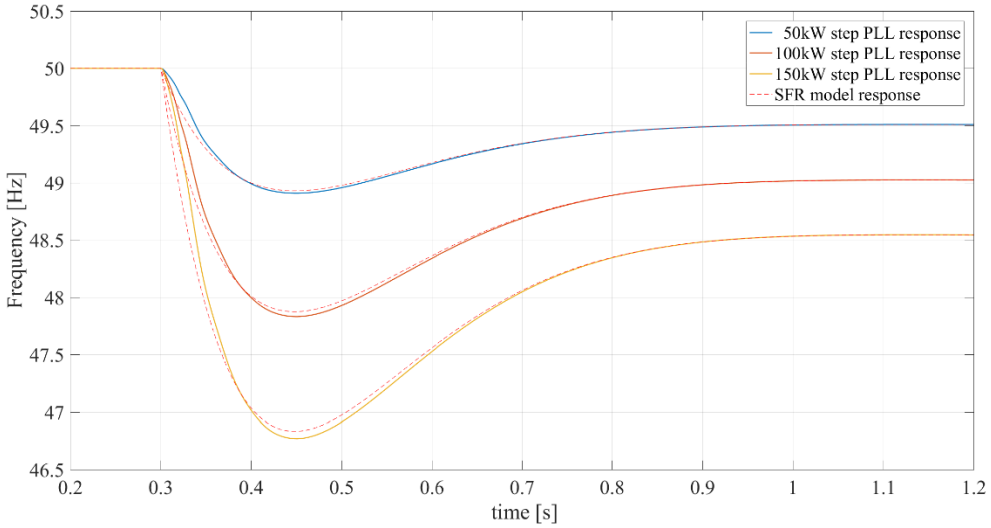

Figure 5.11 Low order SFR model and PLL measured MG response to a load step

5.3.2 Grid feeding mode case study

In this case study, the grid feeding mode control is tested. As the DC side control has been tested in the previous section and both the 2SMC controller and the HESS power division limits have been validated, the focus will be put on the AC side. The same parameters for the inverter in Table 5.16 are also kept. In practice, every event on the active and reactive power set points will be progressive. Thus, the variation of P_{ref} and Q_{ref} will follow a ramp profile of 500 kW/s.

The initial conditions are the following. The RES injection is constant and set at 50 kW while the VRB power reference is set to its maximum. The initial setpoints for active and reactive power injection are set to zero. The load is represented by an aggregated unbalanced load connected to the PCC. The load value is set to 100 kW so the MG is strongly loaded and the voltage profile is poor due to the high

impedance of the MG at the PCC. The load unbalances are chosen to put both the AC side control and the synchronisation algorithm under test with a targeted CUF of approximately 50%. To do so the line *a* is loaded with a different value than line *b* and *c*. Finally, the events and the detail of each sequence are summed up in Table 5.20.

Events	**Description**	**Time**
Event 1	Single phase load of 50kW plugged on line a	0.2s
Event 2	Ramp from P_{ref}=25 kW to P_{ref}=50 kW	0.4s
Event 3	Ramp from Q_{ref}=0 kVA to Q_{ref}=25 kVA	0.5s
Event 4	Step on the load from 50kW to 100kW	0.9s

Table 5.20: Grid feeding mode simulation scenario events description

The results of the simulation for the previously detailed scenario are shown in the following figures. First, it can be noted that the voltage profile at the PCC shown in Figure 5.12 is very low because of the heavy load going through the emulated line of the MG, but it is maintained balanced even though the load unbalances is suddenly increased to reach a CUF of approximatively 45% at t=0.2s. Also, as a consequence, it can be seen that the CUF of the grid is restored to values lower than 5% after the unbalanced load is plugged. It means that the inverter absorbs most of the unbalances of the load which is a functionality provided by STATCOM devices. The transient response of approximately 20ms is satisfactory and matches the settling time used to tune the zero sequence voltage loop controller which is the slowest controller of the overall control strategy. The most important result lies in the very good VUF of less than 2% in steady state while the load is highly unbalanced, which fulfills continental grid standards. This shows that the control strategy is able to tackle an unbalanced load in MG both in term of voltage balance and frequency synchronisation.

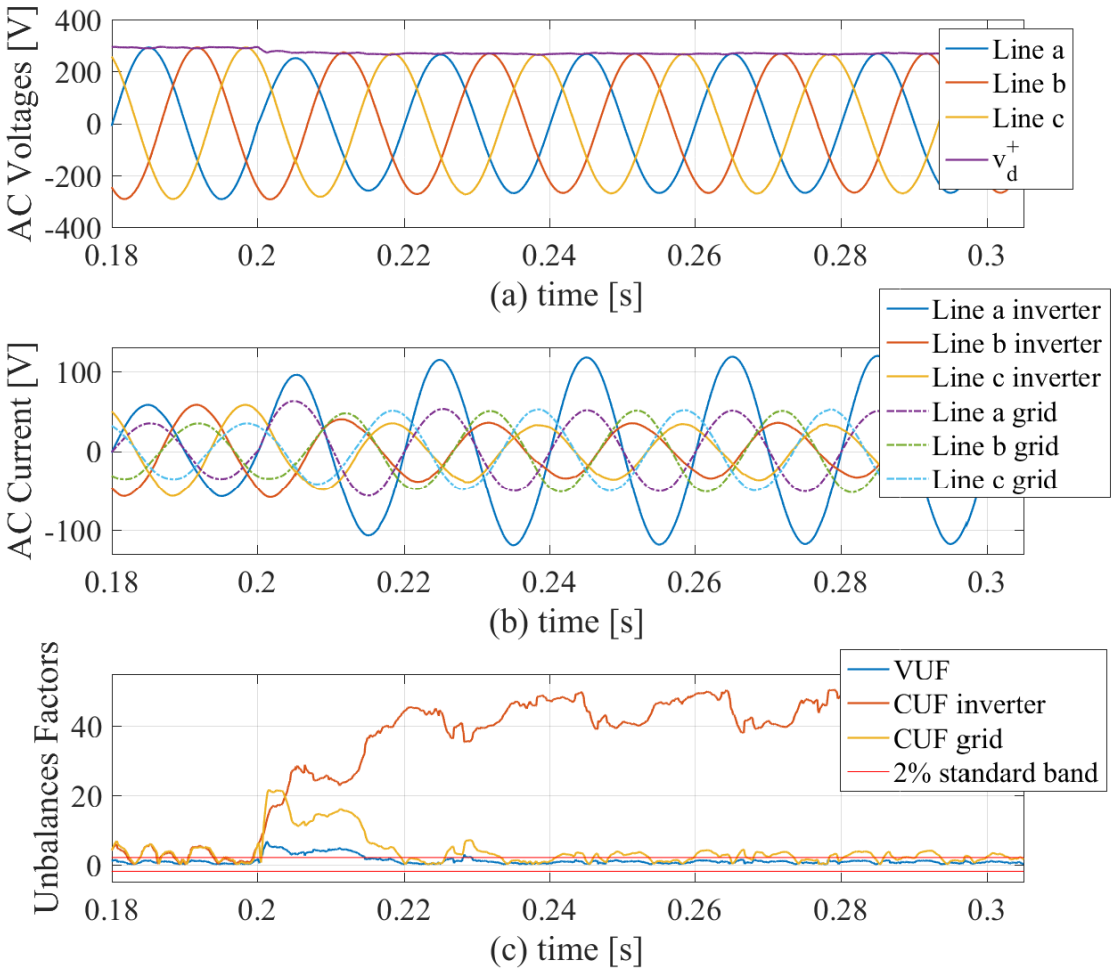

Figure 5.12 Evolution of (a) AC voltages (b) AC currents (c) VUF and CUF while an unbalanced load is plugged

In Figure 5.13 the positive and negative sequence components of both the active and reactive power during the events 2 and 3 are displayed (a), along with the voltage at the PCC (b) and the currents of both the inverter and the grid (c). It can be seen that even though the ramp is steep (500kW/s), the tracking ability of the active power control is effective. The same applies to the tracking abilities on the positive sequence reactive power, but in this case, an overshoot can be noticed at the end of the ramp. This could be explained by the fact that the AC side control tuning has been done considering the MG in islanded mode because of its resistive predominance, and therefore the MG dynamics could be responsible. It should also be noted that the chattering in the active and reactive power is not

consistent with the clean waveforms of both the AC voltages and currents (the TDH of all these signals before the low pass filter stage is always lower than 5% in steady state) and is probably induced by the delay based symmetrical decomposition. Still, the effectiveness of the controller design in grid feeding mode is proven.

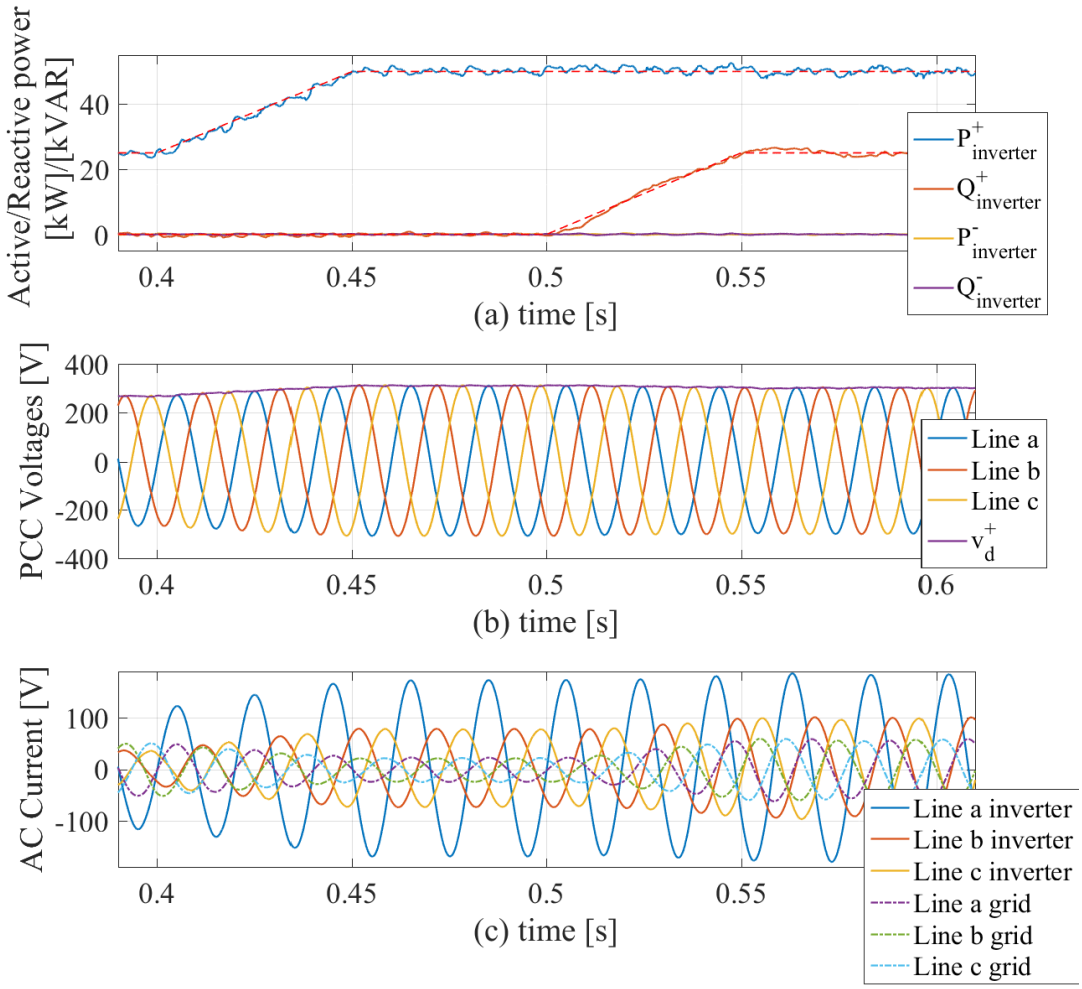

Figure 5.13 Evolution of (a) the active and reactive power of the inverter, (b) PCC voltage and (c) inverter and grid currents while Event 2 and 3 (a)

The result of a sudden increase in the load active power of event 4 is shown in Figure 5.14. It can be seen that the transient on the active and reactive power is quite high and as previously mentioned does not match the AC voltage and current waveforms which is due to the delay based decomposition. Here the transient of roughly 1.5ms is clear and matched the $1/16^{th}$ of a period delay (i.e. 1.25ms) used

for symmetric components decomposition in this case. Nevertheless and as it can be seen in the voltages and currents waveforms the controller ensures clean AC waveform, a quick settling time of 20ms and also keeping the voltage balanced below a 2% VUF.

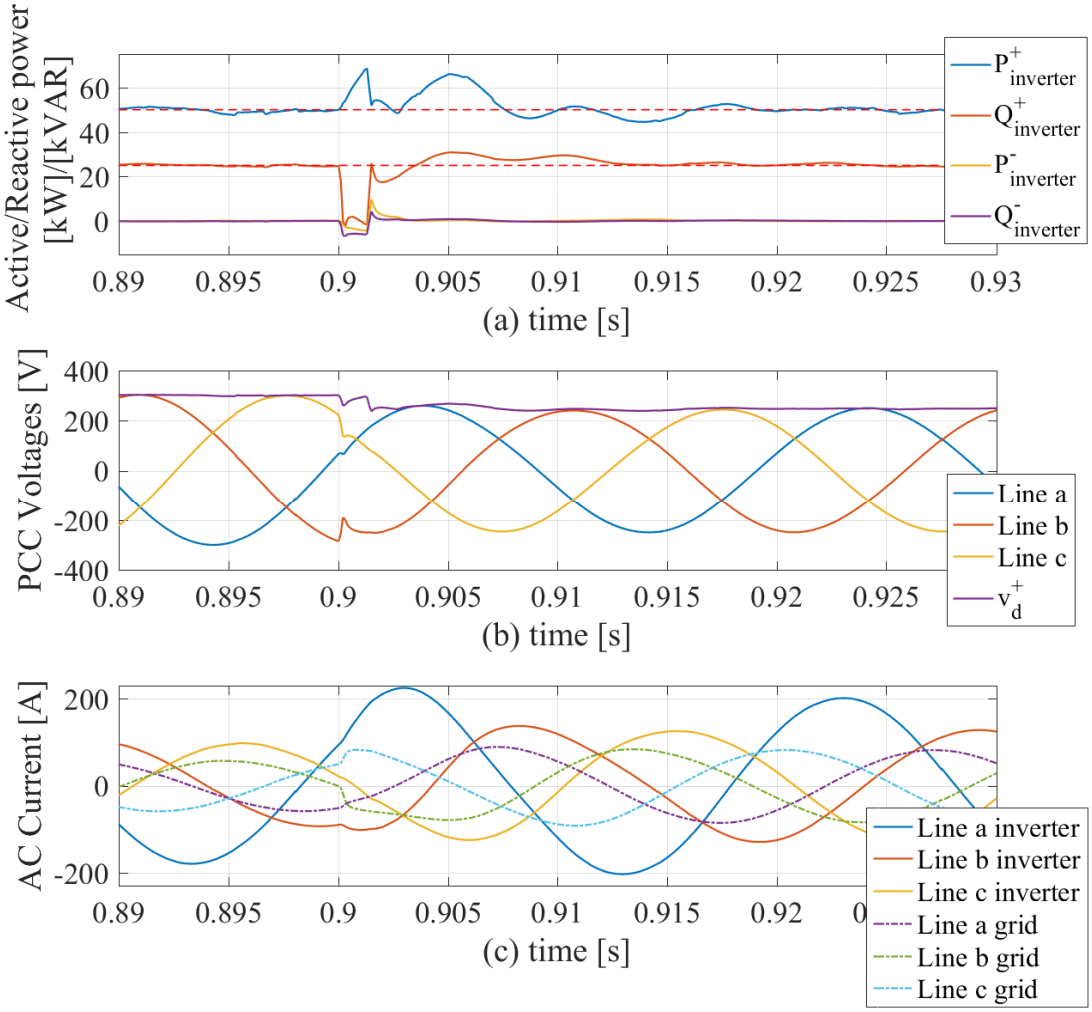

Figure 5.14 Evolution of (a) the active and reactive power of the inverter, (b) PCC voltage and (c) inverter and grid currents while sudden load increase

Additionally, it should be mentioned that the sequence decomposition of both the AC voltages and currents has not been shown in the previous figures. Indeed, the AC side controller is designed to maintain the negative and zero sequence components of the AC voltage to zero. As a result, the peak value of the voltage

at the PCC is always equal in steady state to the positive sequence as it can be seen in Figure 5.12, Figure 5.13 and Figure 5.14.

Finally, the AC side control using the sequence decomposition allows fine tunning each specific component of the signal. As a result, it is possible to provide several services to the MG, like voltage balancing and control over the RES injection in the MG using a HESS, to reach good power quality standards and enable an increased penetration of RES in distribution networks.

5.3.3 Grid supporting mode / Voltage regulation

In this section, the grid supporting capabilities of the 4Leg-3LNPC inverter are tested on the dynamic MG model described previously. The droop voltage functionality developed in section 2.3.3 aims to improve the voltage level of the PCC which is greatly dependant on the load because of the high R/X ratio. As developed in the design process, the high resistivity of the lines makes the voltage at the PCC sensitive to both the active and the reactive power. Since the reactance of the MG is low, and for the sake of simplicity, only the droop control on the positive sequence active power is implemented. The selected droop gain is equal to 250W/V.

The result on the voltage when the droop control is enabled is shown in Figure 5.15. It can be seen that even though the droop gain is low and the reactive power droop is disabled, the voltage is restored very close to its nominal value. The transient response is similar to the previous cases with a settling time of 20ms which conforms to the tuning of the controller.

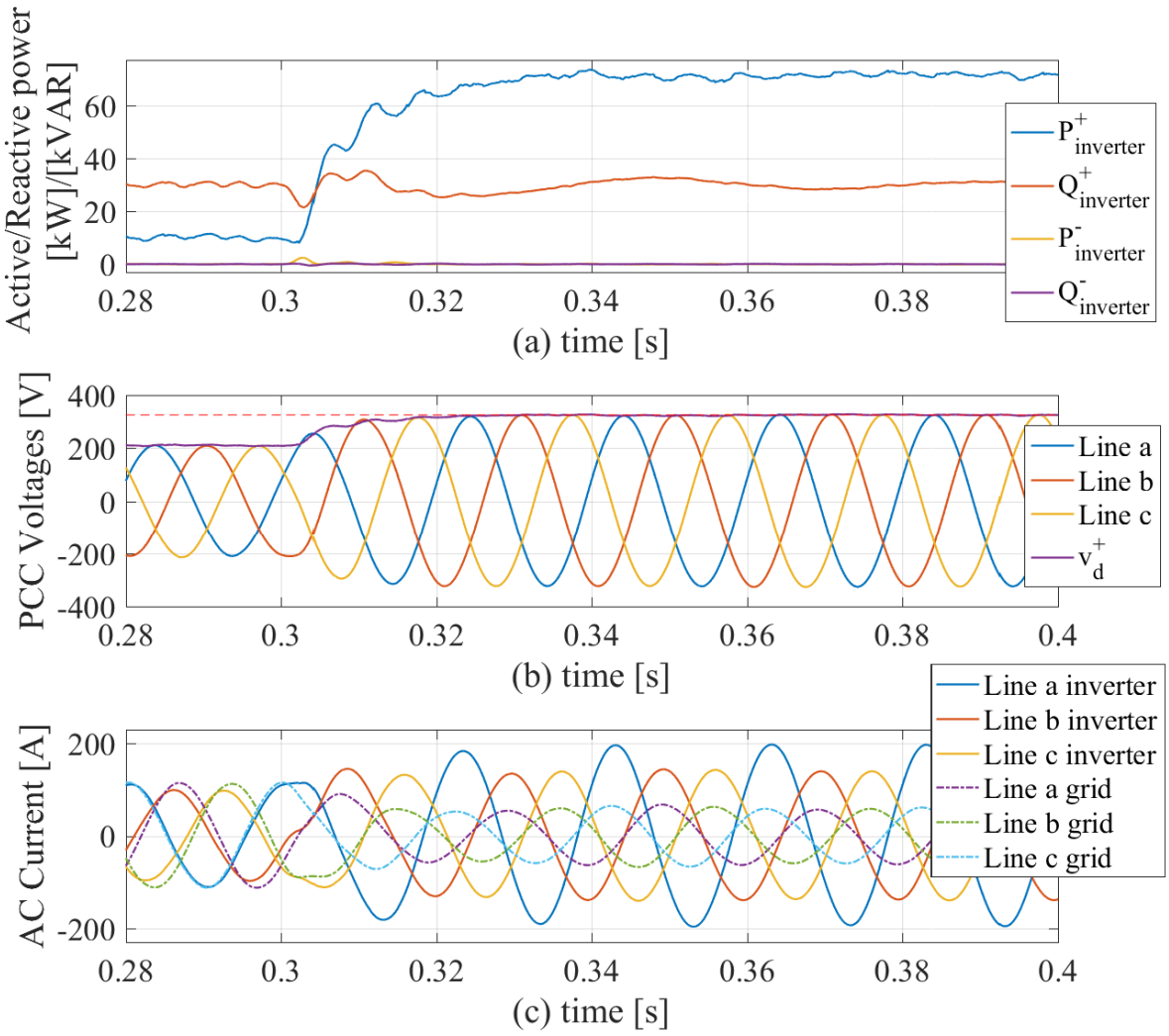

Figure 5.15 Evolution of (a) the active and reactive power of the inverter, (b) PCC voltage and (c) inverter and grid currents while voltage droop is switched on

In Figure 5.16 the result of the voltage droop control while the load is suddenly increased is shown. In this case, the reaching time of the voltage to its 325V target takes slightly more time.

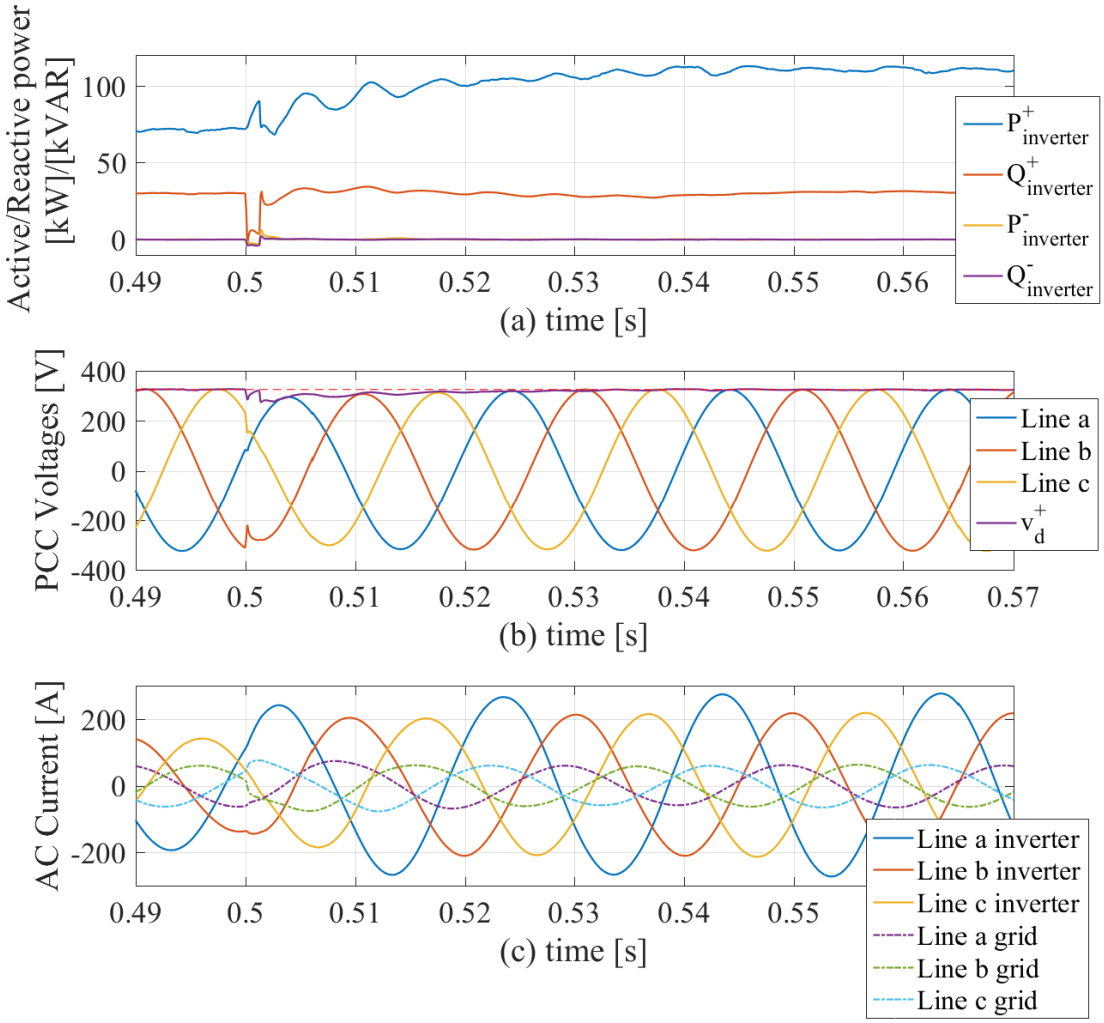

Figure 5.16 Evolution of (a) the active and reactive power of the inverter, (b) PCC voltage and (c) inverter and grid currents while voltage droop enabled and sudden load increase

5.3.4 Grid supporting mode / Frequency regulation

The frequency droop control strategy developed in section 2.3.2 is now tested on the dynamic MG model. The selected droop gain is equal to 10% of MG frequency bias to 10 kW/Hz. In this case study, the initial frequency is set to 49.5 Hz and the inverter is in grid feeding mode with both active and reactive power set point to zero. At 0.3 s the load is suddenly increased from 50kW to 80kW. Then at 1s, the frequency regulation is switched on. As can be seen in Figure 5.17, the load step of approximately 10kW provides an additional frequency deviation of 0.1 Hz.

When the frequency regulation is enabled the frequency deviation is 0.6 Hz from the nominal frequency at 50 Hz. Once the droop control is enabled, the inverter's active power set point increases to reduce the frequency deviation to reach 87kW and 49.75Hz in steady state. It can be also seen that because of the high droop gain associated with the high sensitivity of the MG frequency to active power variation, the primary frequency control is effective and limits the frequency deviation significantly.

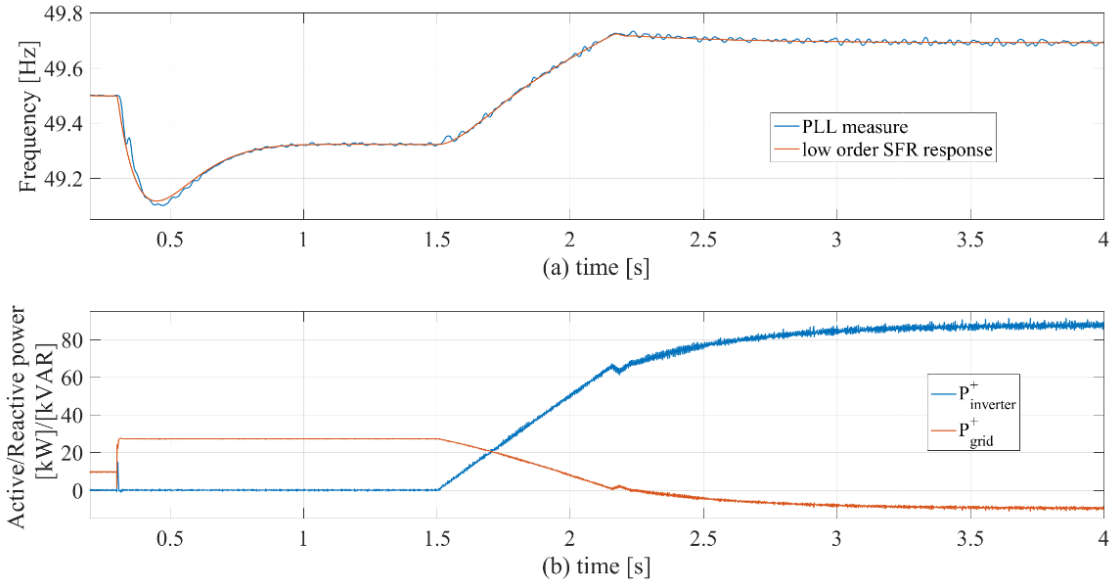

Figure 5.17 Evolution of (a) PLL measured frequency and low order SRF model frequency (b) the active and reactive power of the inverter while frequency droop enabled at t=1.5s

Although the frequency regulation works as expected, it can be seen that the very weak nature of the MG does not give a comfortable operation margin to be able to regulate the frequency properly. Indeed, the resistive nature of the MG line implies that variation of the active power will affect the voltage at the PCC, and thus the frequency regulation ability is constrained by this same voltage limits. For the same reason, the frequency support in a MG context result in changes in the active power set points of the inverter. However, the same variable is used for voltage support, which result in a conflict when both voltage and frequency support are activated.

It should be noted that the low order SFR model assumes that the MG is governed by synchronous machines, which is not always true. Regardless, the results of this section show that if the MG is weak and the line mainly resistive, the frequency should be governed by power electronic devices so it does not depend on the active power balance like in the SFR model used in this work.

5.3.5 Harmonic suppression / non-linear load

So far the controller has shown good grid forming, grid feeding, and grid supporting abilities. It has also been shown that even strong unbalanced loads do not affect the voltage at the PCC thanks to the control of each symmetric component independently. In this section, the ability of the controller to both manage and improve distorted waveforms at the PCC is assessed. The injection of harmonics is done using a non-linear load plugged at the PCC on the grid side. The non-linear load is realized using a passive three-phase rectifier and a 2Ω resistive load on the DC side. The AC side current harmonic content of such load is mainly composed of 5^{th} and 7^{th} harmonics.

As stated in section 4.4.1 the delay based decomposition is not ideal to be able to tackle harmonics issues. Also, section 4.4.8 stated that for the aforementioned reason the tuning of the controller has been restricted to avoid transitory instability. Thus it is expected that the harmonic reduction will not be very effective. Still, the interest of this test is to prove that the controller is able to work properly even with distorted waveforms, and to some extent measure the improvement on low order harmonics.

The inverter is initially in grid forming mode and feeds a 25kW resistive load, while the non-linear load is connected to the MG and consumes approximately 30kW. At 0.2s the inverter is connected to the MG and the control is switched to grid feeding mode. The positive sequence active power reference is set to 25kW and the reactive power one set to zero. Figure 5.18 shows the AC voltage and current waveforms with their associated line by line THDs. It can be seen that before the inverter switches in grid-tie mode, the THDs of both the inverter's voltages and currents are about 20% while the grid side voltages and currents THD are 16.5% and 11.2% respectively. After the connection, the voltage THD at the PCC is

reduced to 10% and the grid side current THD is reduced to 7.5%, while the inverter's current THD rise to 6% approximately. This shows that the control technique is able to switch from islanded mode to grid-tie even though the grid side waveforms present a high harmonic content, and in this case, the PCC voltage THD is reduced by 40% after the connection.

It can also be observed that when the connection occurs there is nearly no transitory. This is due to the fact that the active power reference of the grid feeding mode is set to match the power of the load before the connection occurs. This has been purposely set up for the sake of clarity, in order to avoid transitory and get a cleaner transition in the THD charts. But a 20ms transitory can be noticed on the THDs. This is due to the Matlab implementation of the THD calculation block, which uses Fourier transform and thus needs a full period to converge.

It should be noted that the efficiency of the harmonic cancellation using this technique is not sufficient. A way to improve it would be to extract the harmonic component from the fundamental one and then inject a controlled variable after the signal symmetric components re-composition.

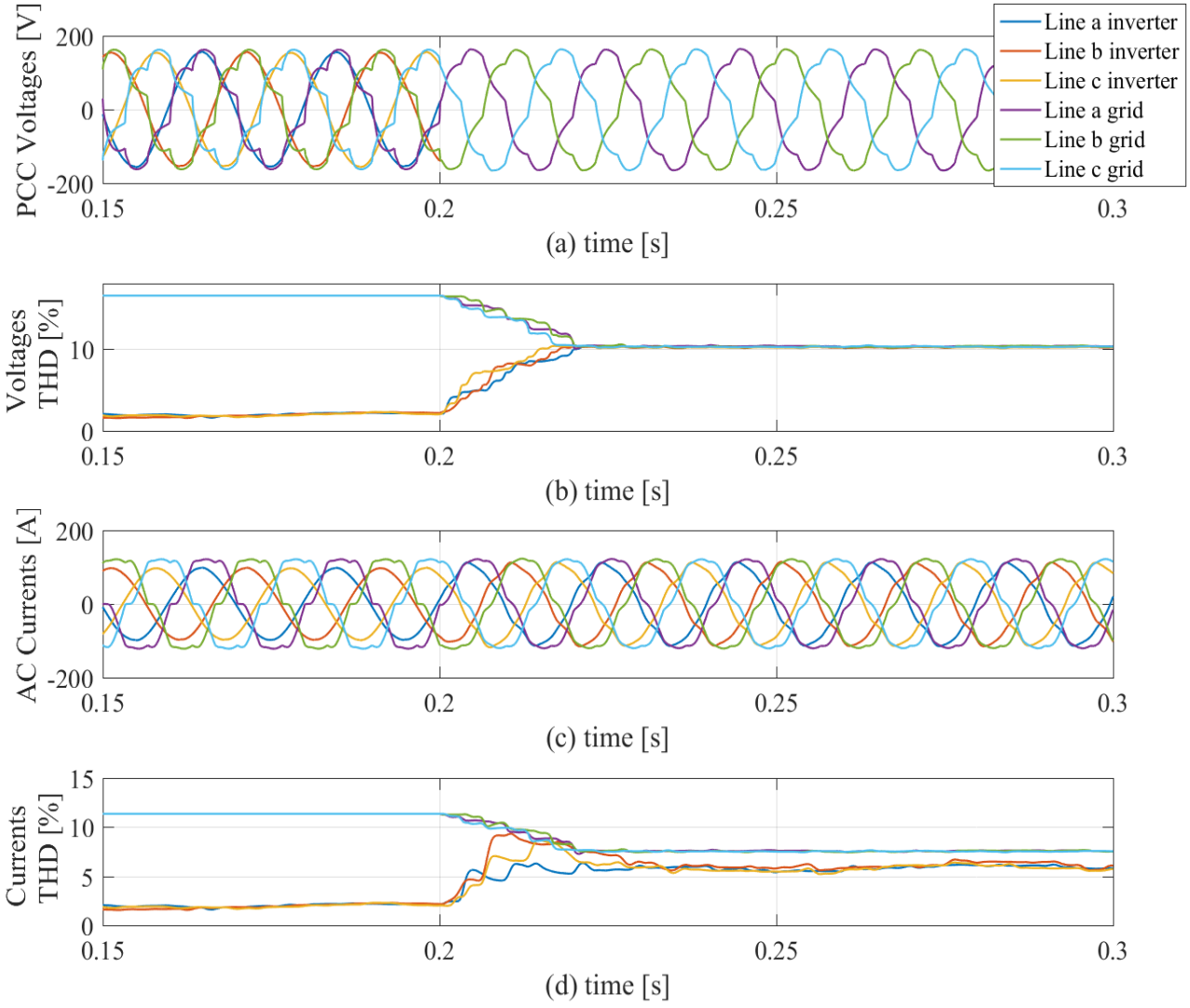

Figure 5.18 Evolution of (a) the AC voltage waveforms at the PCC and (b) the associated THD; (c) the inverter and grid current waveforms and (d) the associated THD while connected to the MG with a non-linear load

5.4 Transition between modes

In this section, the inverter will be alternatively connected and disconnected from the MG to assess the behaviour while in transition between modes [2]. To have a complete insight of the transition between every mode, including the grid supporting one, the scenario of this case study will switch between grid forming,

grid feeding, and grid supporting mode, along with other events. These events are detailed in Table 5.21.

For this case study, the same conditions and parameters as the grid feeding mode in section 5.3.2 are used. Some changes have been made in the PCC load and active and reactive power set points of the grid feeding mode in order to exacerbate the controller solicitations. The total aggregated load at the PCC is initially set to 15kW and suddenly increased to 90kW with an unbalance on line a so the targeted CUF is approximatively 15%.

Events	**Description**	**Time**
Event 1	Switch to connected / grid feeding mode	0.2s
Event 2	Active power reference ramp from -25kW to 50kW	0.25s
Event 3	Switch to islanded / grid forming mode	0.4s
Event 4	Unbalanced load step from 15kW to 115kW	0.5s
Event 5	Switch to connected / grid feeding mode	0.6s
Event 6	Switch to grid supporting mode with V droop on	0.7s
Event 7	Switch to grid forming	0.8s

Table 5.21: Events description of the transition between modes scenario

The result of this scenario is given in Figure 5.19. First, it can be observed that even though the active power setpoint is not equal to the power in islanded mode, the transition between grid forming and grid feeding is conformed to the theory. Just the duration of the transient of Event 1 from 15kW to -25kW at 0.2s is only half the one from 90kW to 50kW at 0.6s which last 20ms. This difference is surprising considering these steps are in the same direction and of same magnitude, but could be explained by the fact that the first one crosses the zero line and thus reduces the control effort compared to the second one. The MG impedance is also highly resistive, and when the first grid connection occurs the voltage at the PCC drops which could also ease the effort. The grid disconnection at 0.4s and 0.8s are also seamless and do not involve disturbances in the reactive power, unlike the grid connection events (Event 1 and Event 5).

Overall the transition between modes is working as expected and shows that the transition mechanism is effective

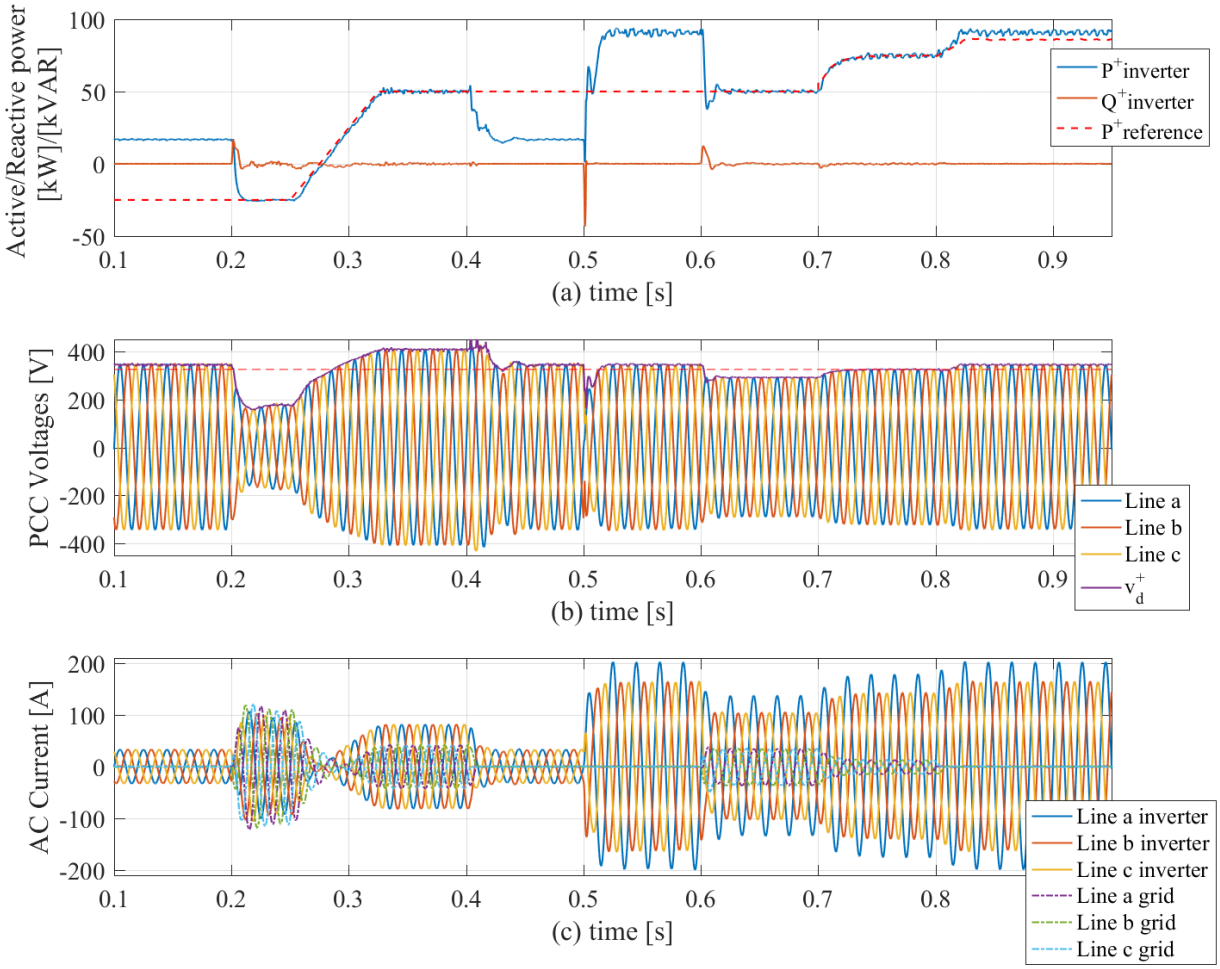

Figure 5.19 Evolution of (a) the active and reactive power of the inverter, (b) PCC voltage and (c) inverter and grid currents while switching between grid forming, grid feeding and grid supporting modes

5.5 Chapter conclusions

This chapter thoroughly tested the hybrid control strategy of a multipurpose 4 Leg 3LNPC developed in Chapter 4. This unique power electronic topology behaves as an interface between two ESSs, a RES injecting on the DC bus, and a weak grid like a MG. The DC side 2SMC controller has shown excellent abilities to control the VRB power flow compared to a classic linear technique like PI regulators. The control strategy developed in Chapter 4 and the structural limits of the topology detailed in Chapter 3 are also tested experimentally. The experimental results are very encouraging considering the good agreement between

simulation and experiments while islanded in grid forming mode. The energy exchange between ESSs has also been highlighted for some operating points. In grid feeding mode simulations have shown the ability to control the positive sequence active and reactive power with precision and minimal overshoot. The grid supporting mode has also shown that the voltage at the PCC and the MG frequency can be improved significantly using droop methods. The control technique has also shown voltages and current harmonic reduction from the grid side while non-linear loads are plugged at the PCC. These tests have been carried out under various conditions like strong unbalanced load, and the transition between each mode has shown a stable behaviour whatever the conditions.

5.6 Chapter references

[1] D. Ocnasu, C. Gombert, S. Bacha, D. Roye, F. Blache, and S. Mekhtoub, "Real-time hybrid facility for the study of distributed power generation systems," *Rev. des Energies Renouvelables*, vol. 11, pp. 343–356, 2008.

[2] H. Gaztañaga, I. Etxeberria-Otadui, S. Bacha, and D. Roye, "Real-time analysis of the control structure and management functions of a hybrid microgrid system," in *IECON Proceedings (Industrial Electronics Conference)*, 2006, no. 1, pp. 5137–5142.

[3] F. D. O. Resende, "Contributions for MicroGrids Dynamic Modelling and Operation," [s. n.], 2007.

[4] P. C. Jayamaha, "Energy Storage For Frequency Support In Weak Electrical Grids," 2015.

[5] P. Kundur, "Power System Stability And Control," *New York McGraw-hill*, Apr. 1994.

[6] A. Ulbig and G. Adamidis, "A low-order system frequency response model," *IEEE Trans. Power Syst.*, vol. 5, no. 3, pp. 720–729, Aug. 1990.

[7] T. H. Bradley, D. Cook, P. N. Borza, and H. Gaztañaga, "An Analysis of Energy Storage Systems for Primary Frequency Control of Power Systems in South Korea," *Energy Procedia*, vol. 107, pp. 116–121, Feb. 2017.

[8] A. Etxegarai, P. Eguia, E. Torres, A. Iturregi, and V. Valverde, "Review of grid connection requirements for generation assets in weak power grids," *Renew. Sustain. Energy Rev.*, vol. 41, pp. 1501–1514, Jan. 2015.

[9] H. Bevrani, A. Ghosh, and G. Ledwich, "Renewable energy sources and frequency regulation: survey and new perspectives," *IET Renew. Power Gener.*, vol. 4, no. 5, pp. 438–457, Sep. 2010.

Chapter 6

Conclusions and Future Lines

Contents

6.1 Conclusions

The main objective of this work has been to realise a multipurpose power electronic interface between a HESS, a RES and a MG based on a multilevel NPC inverter. The targeted functionalities include HESS control, energy efficiency and power quality improvement, along with voltage and frequency regulation in a weak grid context.

The increasing penetration of RES in distribution grid forces DSO to take action against the production variability that leads to energy efficiency and power quality issues. The MG concept is seen as a promising solution to this problem, as described in Chapter 1. It is shown in Chapter 2 that the use of ESS enables the MG with improved grid stability, power quality and energy delivery efficiency while high RES injection to the grid. It also highlight that ESS hybridization allows increased performance while improving the overall lifetime of energy focused ESSs. The proposed HESS uses a VRB for its energy capability and the flexibility of redox flow ESSs, and the Li-Ion technology for its versatility, high efficiency, fast response time and also for its industrial maturity. Given that the HESS sizing depends strongly on the application specification, a simple hybridization factor is applied for energy and power split among the HESS.

Chapter 3 has shown that multilevel NPC power converters can be used to connect several ESS to a grid using only one power electronic interface. Even though the 3LNPC inverter has shown certain limits, its capability to improve the efficiency and the power quality has been proved. The addition of a 4^{th} leg to the 3LNPC inverter enables neutral current control and thus allows the management of unbalanced load under islanded mode or in weak grid conditions. The structural limits of the topology have also been described using a new power based indicator that allows clearer appreciation of the power splitting limits compared to previous works. These limits were validated in simulation, and it has been shown that this configuration allows energy exchange between ESSs.

The main contributions of this work lie in the control strategy of the multipurpose 4 Leg 3LNPC interface. First, a 2SMC controller has been designed and tuned to control the power division among the HESS. This controller has shown increased

performances compared with classical PI controllers and at the same time allow for a reduction of DC link current ripples inherent to multilevel NPC topologies. Then the AC side control was developed based on classical PI double loop control scheme but using symmetric components independent control. This strategy allows control of the system in a way that cancels the negative and zero sequences and thus ensures balanced voltages at the PCC whatever the load unbalances. In addition, grid supporting functionalities have been implemented using droop control technique for both voltage and frequency regulation to provide services to the MG and thus realize a multipurpose power electronic interface. These controllers have been successfully tested experimentally while islanded in grid forming mode, and in simulation while grid tied in grid feeding and grid supporting mode. Unfortunately, the grid feeding and grid supporting test could not be reproduced experimentally because the test bench was not suited to carry out these experiments at the time.

6.2 Future Lines

Further routes for development of the present work have been identified and are given below:

- Asses the behaviour of the proposed control in faulty conditions like fault ride through, voltage sags and voltage flickering.
- Develop an energy management strategy based on optimal control theory which implements the structural limits and the power exchange abilities among the HESS.
- Upgrade the AC side filter to a LCL one and implement active damping suited to the sequence independent control scheme.
- Analyse the effect of different structures and values for the neutral line filter. This could allow another degree of freedom and could be a leverage for increased performance in grid-connected mode.
- Introduce impedances on the inverter DC side to turn it into a Z source inverter. This could allow high AC voltages to be reached using the same DC voltages and to obtain transformerless connection to MV networks, as well as increased power division among the HESS.

6.3 Publications

- I. Vechiu, A. Etxeberria, H. Camblong, and Q. Tabart, "Control of a microgrid-connected hybrid energy storage system," in *3rd International Conference on Renewable Energy Research and Applications, ICRERA 2014*, 2014, pp. 412–417.

- Vechiu, Q. Tabart, and A. Etxeberria, "Power quality improvement using an advanced control of a four-leg multilevel converter," in *2015 IEEE 16th Workshop on Control and Modeling for Power Electronics (COMPEL)*, 2015, pp. 1–6.

- Q. Tabart, I. Vechiu, A. Etxeberria, and S. Bacha, "Limits of 4 Wires 3 Levels NPC topology for Hybrid Energy Storage System and power quality improvement in weak grids," in *Simposium de Génie Electrique*, 2016.

- Vechiu, Q. Tabart, A. Etxeberria, and R. Lopez, "Operational limits of four wires three levels NPC topology for power quality improvement in weak grids," in *EEEIC 2016 - International Conference on Environment and Electrical Engineering*, 2016, pp. 1–5.

- M. Real, Q. Tabart, A. A. Akle, and F.- Bidart, "Building Pathways for Empowering User Toward Prosumer Behaviour The Design for Experience with the Prosumer Empowerment Concentric Model," in *SMART INTERFACES 2017, The Symposium for Empowering and Smart Interfaces in Engineering*, 2017, no. i, pp. 66–69.

- Q. Tabart, I. Vechiu, A. Etxeberria, and S. Bacha, "Hybrid Energy Storage System Microgrids Integration for Power Quality Improvement Using Four-Leg Three-Level NPC Inverter and Second-Order Sliding Mode Control," *IEEE Trans. Ind. Electron.*, vol. 65, no. 1, pp. 424–435, 2018.

- R. H. Lopez Rodriguez, I. Vechiu, S. Jupin, S. Bacha, Q. Tabart, and E. Pouresmaeil, "A new energy management strategy for a grid connected wind turbine-battery storage power plant," in *IEEE International Conference on Industrial Technology (ICIT)*, 2018, pp. 873–879.